**Universidade do Minho**
Escola de Ciências

Cristiano Miguel Pereira Viães

# Development of multifunctional dental implants

october 2022

Development of multifunctional dental implants
Cristiano Miguel Pereira Viães
Uminho | 2022

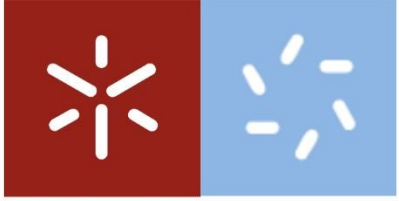

**Universidade do Minho**
Escola de Ciências

Cristiano Miguel Pereira Viães

# Development of multifunctional dental implants

Master Thesis
Master in Biophysics and Bionanosystems

Work developed under the supervision of
**Luis Silvino Marques**
with co-supervisior
**Sandra Mariana Silva Marques**

october 2022

## Copyright and terms of use of the work by third parties

## Acknowledgements:

This Thesis represents the ending of an important stage of my life. Throughout my path I was positively influenced by a number of friends, family and mentors to whom I would like to thank.

To my advisor Luís Silvino Marques and my co-adviser Sandra Mariana Silva Marques for the guidance.

To the group from Minho's University to Sandra Carvalho, Nuno Bexiga, Edgar and José David and the group NOVA-FCT, to Tânia, Francisco, and Professor Isabel Sá-Nogueira for all the help and patience to transmit to me the knowledge I needed during this journey.

To my grandmother, for being great role model who inspire me every day.

To my parents, for the help, strength, and motivation which they guide me with every day.

And finally, to my friends, for all the love, patience, and motivation to always be a better version of me.

To all, thank you.

## STATEMENT OF INTEGRITY

I hereby declare having conducted this academic work with integrity. I confirm that I have not used plagiarism or any form of undue use of information or falsification of results along the process leading to its elaboration.

I further declare that I have fully acknowledged the Code of Ethical Conduct of the University of Minho.

**Desenvolvimento de implantes dentários multifuncionais.**

## Resumo:

Os implantes dentários são geralmente fabricados com materiais à base de titânio (Ti) devido à sua biocompatibilidade e resistência à corrosão. No entanto, a baixa capacidade de formar uma forte ligação química com o tecido vivo, conhecida como bioatividade, é uma das desvantagens deste tipo de materiais. Consequentemente, o uso de implantes dentários é às vezes acompanhado por falhas devido à fraca osseointegração e posteriores infeções causadas por microrganismos. Nesse sentido, são necessárias novas abordagens para o desenvolvimento de superfícies bioativas capazes de potencializar o crescimento ósseo e que, ao mesmo tempo, apresentem propriedades antibacterianas.

O desenvolvimento de superfícies altamente bioativas e antimicrobianas, com melhor osseointegração e resistência à corrosão, pode ser alcançado por meio da deposição de revestimentos à base de TiN-M (M=Ag, Zn) por pulverização catódica reativa em magnetrão. A escolha deste tipo de material deve-se às propriedades dos seus constituintes: o nitreto de titânio por ser um biocompatível e aumentar a resistência à corrosão; e as nanopartículas de prata (Ag) e zinco (Zn) pelas suas propriedades antimicrobianas.

Pela variação das condições de deposição poderemos obter revestimentos com diferentes composições de nitreto de titânio e de nanopartículas, explorando desta forma um vasto espectro de propriedades mecânicas e biológicas, sem que haja nenhum tipo de efeito citotóxico.

**Palavras-chave**: Implante dentário; Nitreto de titânio; Osseontegração; Periimplantite; Pulverização catódica reativa em magnetrão

**Development of multifunctional dental implants**

## Abstract:

Dental implants are generally manufactured by titanium (Ti) based materials due to their biocompatibility and corrosion resistance. However, a low ability to form a strong chemical bond with living tissue, known as bioactivity, is one of the disadvantages of this type of material. Consequently, the use of dental implants is sometimes accompanied by failures due to poor osseointegration and subsequent infections caused by microorganisms. In this sense, new approaches are needed for the development of bioactive surfaces that can enhance bone growth and, at the same time, have antibacterial properties.

The development of highly bioactive and antimicrobial surfaces, with better osseointegration and corrosion resistance, can be achieved through the deposition of coatings based on TiN-M (M = Ag, Zn) by reactive sputtering in magnetron. The choice of this type of material is due to the properties of its constituents: titanium nitride as it is biocompatible and increases corrosion resistance; and silver (Ag) and zinc (Zn) nanoparticles, for their antimicrobial properties.

By varying the deposition conditions, coatings with different compositions of titanium nitride and nanoparticles can be obtained with different compositions of titanium nitride and nanoparticles, thus exploiting a wide spectrum of mechanical and biological properties, without any type of cytotoxic effect.

**Keywords:** Dental implant; Osseointegration; Peri-implantitis; Reactive magnetron cathodic sputtering; Titanium nitride.

## Table of Contents:

**Acknowledgements:** ..... III

**Resumo:** ..... V

**Abstract:** ..... VI

**List of Figures:** ..... X

**List of tables:** ..... XIII

**List of Abbreviations:** ..... XIV

**Chapter 1 - Introduction:** ..... 16

1. **Introduction:** ..... 17
2. **Work objectives, methodology and thesis organization:** ..... 18
3. **References:** ..... 21

**Chapter 2 - State of the art:** ..... 22

1. **Introduction:** ..... 23
2. **Dental implants:** ..... 23
3. **Titanium-based dental implants:** ..... 25
   - 3.1. **Biocompatibility of titanium for dental implants:** ..... **26**
4. **Failure of dental implants:** ..... 26
   - 4.1. **Osseointegration Failure:** ..... **27**
   - 4.2. **Peri-implantis infection:** ..... **27**
5. **Surface modification:** ..... 29
6. **Bioactive materials:** ..... 30
   - 6.1. **Antibacterial activity Ag nanoparticles:** ..... **31**
   - 6.2. **Antibacterial activity Zn nanoparticles:** ..... **32**
7. **References:** ..... 34

**Chapter 3 – Coatings deposition TiN-Ag and TiN-Zn:** ..... 40

1. **Introduction:** ..... 41

**2. Physical Vapor Deposition (PVD) Technology:** ..... 41

**3. Cathodic sputtering:** ..... 41

**3.1. Magnetron System:** ..... **43**

**3.2. Unbalanced magnetron sputtering:** ..... **44**

**3.3. Closed-field unbalanced magnetron sputtering:** ..... **46**

**4. Coatings deposition: TiN-Ag and TiN-Zn:** ..... 46

**4.1. Equipment used in the production of the coatings:** ..... **47**

**4.2. Preparation of the substrates:** ..... **47**

**4.3. Deposition Parameters of TiN, TiN-Ag, and TiN-Zn coatings:** ..... **48**

**5. References:** ..... 51

**Chapter 4 - Characterization techniques** ..... 54

**1. Introduction:** ..... 55

**2. Physical and chemical characterization techniques:** ..... 55

**2.1. Scanning electron microscopy and energy dispersive spectroscopy (SEM-EDS):** ..... **55**

**2.2 Atomic force microscopy (AFM):** ..... **58**

**2.2. X-Ray Diffraction (XRD):** ..... **60**

**2.3. Wettability and Surface energy:** ..... **61**

**2.4. Inductively Coupled Plasma Optical Emission Spectrometry (ICP-OES): 62**

**3. Biological analyses:** ..... 65

**3.1. Cell viability:** ..... **65**

**3.2. Antibacterial Activity Assay:** ..... **66**

**3.3. Cell's Adhesion test:** ..... **68**

**3.4. Cell's Proliferation assay:** ..... **69**

**3.5. Cell's Differentiation assay:** ..... **69**

**3.6. Statistical analysis:** ..... 70

**4. References:** ..... 71

**Chapter 5 – Results and Discussion:** ..... 73

**1. Introduction:** ..... 74

**2. Physical and chemical characterization:** ..... 74

**2.1. Morphology: ..... 76**

**2.2 Structural analysis: ..... 81**

**2.3 Silver and zinc ion release: ..... 86**

**3. Biological analysis:** ..... 88

**3.1. Cell viability: ..... 88**

**3.2. Antibacterial activity: ..... 89**

**4.1. Cell's Adhesion, cell's proliferation, and Cell's differentiation assay: 92**

**4. References:** ..... 96

**Chapter 6 – Final remarks and future research:** ..... 101

**1. Final remarks:** ..... 102

**2. Future work:** ..... 103

**Annex 1:** ..... 104

## List of Figures:

FIGURE 1 - SCHEME OF THE WORK METHODOLOGY USED FOR THE DEVELOPMENT OF THE MULTIFUNCTIONAL IMPLANTS. ..... 19

FIGURE 2 - COMPONENTS OF RESTORED IMPLANT. A, IMPLANT CROWN. B, ABUTMENT. C, IMPLANT FIXTURE. ADAPTED [2] ..... 23

FIGURE 3 - STEPS OF BIOFILM FORMATION ON TITANIUM BIOMATERIAL. (1) ADSORPTION OF PROTEINS (2) INITIAL COLONIZERS ADHERE TO THE PROTEIN LAYER. (3) BIOFILM ACCUMULATION. (4) THIS SYNERGISTIC INTERACTION BETWEEN ORGANISMS CONTINUES TO CONTRIBUTE TO THE BIOFILM STRUCTURE. ADAPTED [27]..... 28

FIGURE 4 - INCREASED BIOFILM ACCUMULATION ON IMPLANT SURFACES RESULTS IN AN INFLAMMATORY PROCESS THAT ALTERS THE ENVIRONMENT, CAUSING A MICROBIOLOGICAL CHANGE AND DISEASE PROGRESSION (RED BOXES). THE MICROBIOLOGICAL CHANGE IN BIOFILMS. AS A RESULT, PERI-IMPLANT MUCOSITIS CLINICALLY TRANSFORMS INTO PERI-IMPLANTITIS. ADAPTED [23]. ..... 29

FIGURE 5 SCHEME OF SURFACE FUNCTIONALISATION OF DENTAL IMPLANTS WITH THE AIM OF IMPROVING OSSEOINTEGRATION AND INFECTION CONTROL. ADAPTED [30]..... 30

FIGURE 6 - THE ANTIBACTERIAL ACTIONS OF SILVER NANOPARTICLES (AGNPS) [48]..... 32

FIGURE 7 - MORE MATERIAL IS LOCALLY ELIMINATED AS MORE IONS ARE PRODUCED IN THE PERMANENT MAGNETS' MAGNETIC FIELD.. (A) CROSS-SECTION DIAGRAM OF THE TARGET [18]; (B) SILVER TARGET AT THE END OF THE DEPOSITIONS..... 44

FIGURE 8 - SCHEMATIC REPRESENTATION OF THE PLASMA CONFINEMENT OBSERVED IN CONVENTIONAL AND UNBALANCED MAGNETRONS [17]..... 45

FIGURE 9 - DUAL UNBALANCED MAGNETRON CONFIGURATIONS [17] ..... 46

FIGURE 10 - REACTIVE MAGNETRON SPUTTER EQUIPMENT FROM THE UNIVERSITY OF MINHO..... 47

FIGURE 11 - PREPARATION OF THE SUBSTRATES..... 48

FIGURE 12 - SCHEMATIC REPRESENTATION AND PARAMETERS OF DEPOSITED INTERLAYERS..... 49

FIGURE 13 - SCHEMATIC DIAGRAM ILLUSTRATING THE PRIMARY ELECTRON EMISSION PROCESS. (A) HIGH-ENERGY INDUCES TARGET ATOM WITH AN INNER-SHELL EMISSION. (B) AN ELECTRON DROPS FROM A HIGHER ENERGY LEVEL TO THE VACANT HOLE BY EMITTING X-RAYS [8]. ..... 57

FIGURE 14 - EXAMPLE OF AN EDS SPECTRUM FOR A TIN-AG 0.21A SAMPLE. ..... 58

FIGURE 15 - SKETCH ILLUSTRATING THE PRINCIPAL OF ATOMIC FORCE MICROSCOPY [9]. ..... 59
FIGURE 16 - GEOMETRICAL CONDITION FOR DIFFRACTION FROM LATTICE PLANES [12]. . 60
FIGURE 17 - SCHEMATIC OF A TYPICAL INDUCTIVELY COUPLED PLASMA-OPTICAL EMISSION SPECTROMETRY (ICP-OES) SYSTEM [16]. ..... 63
FIGURE 18 - ICP-OES SILVER CALIBRATION: (A) SILVER CALIBRATION CURVE WITH NITRIC ACID; (B) ZINC CALIBRATION CURVE WITH NITRIC ACID..... 64
FIGURE 19 - STRUCTURES AND REACTION MECHANISM OF RESAZURIN (RZ), RESORUFIN (RS) [18]. ..... 65
FIGURE 20 - 96-WELL PLATE, "SEEDED" WITH SAOS-2 CELLS AT A CONCENTRATION OF 30000 CELLS/CM$^2$. ..... 66
FIGURE 21 - 20-WELL PLATE, WITH THE COATINGS PRODUCED. EACH COATING CONTAINS A DROP OF 40 μL OF THE PRE-INOCULUM AT A CONCENTRATION OF 5 X 105 CELLS/ML. ..... 67
FIGURE 22 - PETRI DISHES WERE REMOVED FROM THE INCUBATOR AND THE NUMBER OF COLONY FORMING UNITS (CFU), FOR EACH DILUTION: (A) TIN-ZN 0.25 COATING; (B) TIN COATING..... 68
FIGURE 23 - CHEMICAL COMPOSITIONS OF THE VARIOUS COATINGS: (A) TIN-AG; (B) TIN-ZN. ..... 75
FIGURE 24 - SEM MICROGRAPHS IN SE MODE OF THE DIFFERENT FILMS, DEPOSITED IN PVD. THE INSERTS ARE CROSS-SECTION MICROGRAPHS..... 77
FIGURE 25 - AFM IMAGES OF THE TIN, TIN-AG AND TIN- ZN COATINGS DEPOSITED ON SILICON SUBSTRATES. ..... 79
FIGURE 26 - THE WATER CONTACT ANGLE OF THE SEVERAL SAMPLES. DATA WAS REPRESENTED AS MEAN± STANDARD DEVIATION. ..... 81
FIGURE 27 - XRD DIFFRACTOGRAM OF SEVERAL COATINGS: (A) TIN-AG; (B) TIN-ZN ... 82
FIGURE 28 - AG+ RELEASE ALONG TIME (2H, 6H, 12H, 24H, 48H, 120H AND 168H) DETERMINED BY ICP-OES ANALYSIS. DATA WAS REPRESENTED AS MEAN± STANDARD DEVIATION..... 86
FIGURE 29 - ZN+ RELEASE ALONG TIME (2H, 6H, 12H, 24H, 48H, 120H AND 168H) DETERMINED BY ICP-OES ANALYSIS. DATA WAS REPRESENTED AS MEAN± STANDARD DEVIATION..... 87

FIGURE 30 - CELL VIABILITY ASSESSED USING THE RESAZURIN ASSAY. C- WAS THE NEGATIVE CONTROL. C+ WAS THE POSITIVE CONTROL. DATA WAS REPRESENTED AS MEAN± STANDARD DEVIATION. SIGNIFICANT VALUES AS *P > 0.05. ..... 88
FIGURE 31 - SURVIVAL RATE (%) OF: E. COLI: (A) BOXPLOT, (B) BAR GRAPH; S. AUREUS: (C) BOXPLOT, (D) BAR GRAPH; S. MUTANS: (E) BOXPLOT, (F) BAR GRAPH. DATA WAS REPRESENTED AS MEAN± STANDARD DEVIATION. SIGNIFICANT VALUES AS ****P < 0.0001***P <0.001, **P < 0.01. THE GREEN TRIANGLE SYMBOLISES THE MEAN, THE BLACK LINE THE MEDIAN AND THE DOTS THE VALUES OBTAINED IN EACH REPETITION. ..... 90
FIGURE 32 - ADHESION OF SAOS-2 CELLS ON DIFFERENT COATINGS. DATA WAS REPRESENTED AS MEAN± STANDARD DEVIATION. SIGNIFICANT VALUES AS ****P < 0.0001, **P < 0.01. ..... 92
FIGURE 33 - CELL PROLIFERATION OF SAOS-2 CELLS "SEEDED" ON THE COATINGS PRODUCED. THE CONTROL IS SAOS-2 CELLS GROWN ON THE PLATES. ..... 94
FIGURE 34 - ALP ACTIVITY OF SAOS-2 CELLS "SEEDED" ON THE COATINGS PRODUCED. 95

## List of tables:

Table 1 - Various materials choices to fabricate dental abutments [1]. ..... 24
Table 2 - Composition and properties of titanium alloys used as implants [4]. ..... 25
Table 3 - Chemical composts used to make 400 mL of artificial saliva. ..... 63
Table 4 - Summarized deposition parameters of TiN, TiN-Ag, and TiN-Zn coatings... 50
Table 5 - Results obtained for chemical composition, thickness, deposition rate and roughness, as well as some experimental details. ..... 74
Table 6 - Area of the nanoparticles present in each sample. ..... 79
Table 7 - Water, glycerol and 1-bromonaphthalene contact angles and surface energy components of the different coatings. ..... 80
Table 8 - Grain size was calculated on TiN-Ag coatings for the most intense TiN and Ag peaks. ..... 83
Table 9 - Grain size was calculated on TiN-Zn coatings for the most intense TiN and Zn peaks. ..... 84
Table 10 - XRD network parameters was calculated on TiN-Ag coatings for the most intense TiN and Ag peaks. ..... 85
Table 11 - XRD network parameters was calculated on TiN-Zn coatings for the most intense TiN and Zn peaks. ..... 85
Table 12 – Proliferation two-way ANOVA statistical test results comparing TiN coating with doped coatings. ..... 93
Table 13 - ALP activity two-way ANOVA statistical test results comparing TiN coating with doped coatings ..... 94

## List of Abbreviations:

| | |
|---|---|
| **PVD** | Physical vapor phase deposition |
| **TiN** | Titanium nitride |
| **Ti** | Titanium |
| **Ag** | Silver |
| **Zn** | Zinc |
| **Al** | Aluminium |
| **V** | Vanadium |
| **Si** | Silicon |
| **Ar** | Argon |
| **$N_2$** | Nitrogen |
| **ZnO** | Zinc oxide |
| **AgO** | Silver oxide |
| **WHO** | World Health Organization |
| **ROS** | Reactive oxygen species |
| **ATP** | Adenosine triphosphate |
| **DNA** | Deoxyribonucleic acid |
| **ALP** | Alkaline phosphatase activity |
| **cpTi** | Commercially pure titanium |
| **SEM** | Scanning electron microscope |
| **XRD** | X-ray powder diffraction |
| **AFM** | Atomic force microscopy |
| **EDS** | Energy-dispersive X-ray spectroscopy |
| **at.%** | Atomic percentage |
| **WCA** | Water contact angle |
| **DC** | Direct current |
| **PULS** | Pulse |
| **ICP-OES** | Inductively Coupled Plasma - Optical Emission Spectrometry |
| **NaCl** | Sodium chloride |
| **$CaCl_2$** | Calcium chloride |
| **KCl** | Potassium chloride |
| **NADPH** | Nicotinamide adenine dinucleotide phosphate |
| **Abs** | Absorbance |

| | |
|---|---|
| **ISO** | International Organization for Standardization |
| **TSA** | Trypticase Soy Agar |
| **CFU** | Colony-forming unit |
| **p-NPP** | p-Nitrophenyl Phosphate |
| **HCl** | Hydrochloric acid |
| **SD** | Standard deviation |
| **ICDD** | International Centre for Diffraction Data |
| **FCC** | Face centered cubic |

# Chapter 1 - Introduction:

# 1. Introduction:

The impact of edentulism on the health and well-being of the population is a problem requiring intervention. Human beings have always faced problems associated with tooth loss. In the past, the inability to bite and chew minimally processed food was a threat to survival. However, with the advancement in food processing, survival is no longer a concern. Instead, the ability to enjoy a wide variety and textures of food has become the primary motivation for attempting to retain teeth or seeking methods for replacing lost teeth. Nowadays, facial aesthetic factors have gained increasing importance in the maintenance of dentition and with the increase in contemporary dental techniques, replacement of lost teeth has become possible and desirable [1]. According to "Markets and Markets" [2], the global dental implants market is expected to grow at a rate of 6.5% by 2023, reaching approximately USD 13.01 billion by then. The growth of this market is driven by the increasing elderly population and corresponding age-related dental diseases, the increasing prevalence of dental caries and periodontal diseases worldwide and the increasing desire for cosmetic dental surgery and the growing number of dentists capable of doing so [2]. Dental implants can be manufactured from various materials, each of which has different advantages and disadvantages. Due to exceptional corrosion resistance, biocompatibility, and mechanical stability, commercially pure titanium, and its alloy Ti-6Al-4V are the most commonly used materials in their manufacture [3]. However, there is still debate about its capacity to integrate with bone, since the Ti surface does not present the capacity to stimulate the formation of new tissue, delaying the biological integration of the dental implant [4] [5]. Subsequently, the slow osseointegration of the dental implant leads to a long postoperative period and increases the likelihood of microorganisms interacting with the surgical site. Microbial adhesion and colonization may induce infections with consequent surgical complications [3]. Statistically, 47% of implant failures are due to inefficient osseointegration and 45% occur during the first year of use [6]. Thus, the development of bioactive surfaces capable of enhancing and promoting bone growth and bone matrix mineralization, thus reducing the frequency of infectious complications, is a major challenge for manufacturers and the scientific community worldwide.

In this work, a way to increase the probability of success of dental implants by adding a coating to the implant, having in mind that the perfect coating should possess antibacterial and osseointegrative properties [7]. Thus, considering this goal, titanium nitride (TiN) was chosen as the base coating, as it has excellent corrosion and wear

resistance properties and has been used as a hard coating in dental implants [8]. Moreover, in order to make it biologically active, zinc and silver nanoparticles were added, which can confer antibacterial properties to the implant surface [7].

## 2. Work objectives, methodology and thesis organization:

This work is inserted in the project ORAiDEA - POCI-01-0247-FEDER-039985 "Development of Multifunctional Dental Implants", by the European Regional Development Fund (ERDF) through the Operational Program Competitiveness and Internationalization (POCI) which proposes to develop multifunctional dental implants, starting with their design and subsequent production through machining of titanium blocks. The project aims to build an important step toward solving real problems and needs that affect more specifically the sector of dental implants, namely peri-implant infections, which are increasingly common and can lead to implant loss and the need for additional surgeries. In this sense, this work aims to deposited by a physical vapor phase deposition (PVD) technology, namely magnetron sputtering, multifunctional titanium nitride (TiN) coating doped with metallic nanoparticles, such as silver (Ag) and zinc (Zn) in dental implants allowing the improvement of osseointegration capacity and antibacterial activity through.

In more detail, the objectives of this work are:

- Deposit by PVD TiN-M [M=Ag; Zn] coatings with different amounts of metal nanoparticles on Ti-6Al-4V substrates;
- Characterization of physical and chemical properties, like: roughness, surface energy, bioactivity studies, among others;
- Obtain coatings with good mechanical properties and with antibacterial activity over time without cytotoxicity;
- To evaluate the osseointegrative capacity, through the assessment of adhesion, proliferation and differentiation of SaOS-2 cells (osteoblasts);
- Correlate the kinetics of ion release with bacterial inhibition.

The following scheme, figure 1, summarizes the working methodology used in the thesis, which will be described throughout the different chapters.

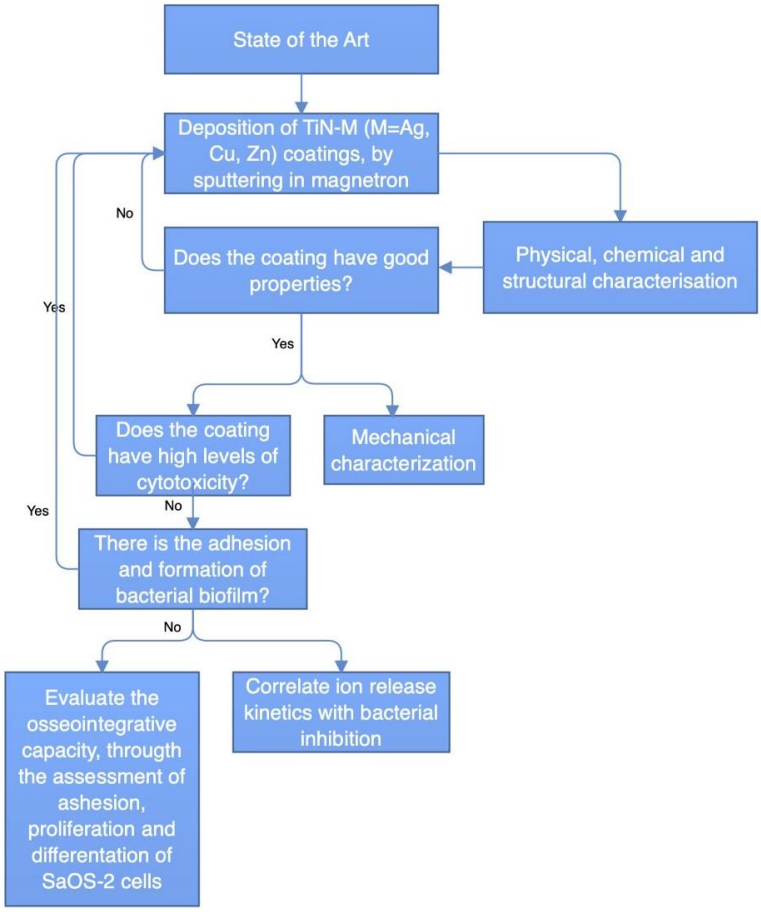


*Figure 1 - Scheme of the work methodology used for the development of the multifunctional implants.*

This paper is organized into 6 chapters to provide a logical sequence for understanding the production of TiN-M coatings by magnetron sputtering and its subsequent characterization.

**Chapter 1** introduces the topic of the thesis and the methodology followed is presented.

**Chapter 2** presents the state of the art. Throughout the chapter, a review of the literature on dental implants and their current problems is provided.

**Chapter 3** describes the production of TiN-Ag and TiN-Zn coatings by magnetron sputtering. A theoretical explanation of the technique is provided, and the methodology and conditions used to obtain the coatings are presented.

**Chapter 4** includes a brief description of characterisation techniques. An explanation of the theoretical concept of the physical and chemical characterisation

techniques used is provided and the protocols followed in the biological analysis are described.

**Chapter 5** presents and discusses the results. The influence of the deposition conditions on the chemical composition, morphology and ion release is discussed. Results of biological tests are also discussed.

Lastly, the **Chapter 6**, final remarks and future research presents an overall conclusion of the thesis and discusses possible future research perspectives.

## 3. References:


[1] M. S. Block, “Dental Implants: The Last 100 Years,” J. Oral Maxillofac. Surg., vol. 76, no. 1, 2018, doi: 10.1016/j.joms.2017.08.045.

[2] “Dental Implants and Prosthesis Market Size, Share and Trends forecast to 2023 by Type, Material, Type of Facility | COVID-19 Impact Analysis | MarketsandMarkets™” https://www.marketsandmarkets.com/Market-Reports/dental-implants-prosthetics-market-695.html (accessed Jan. 25, 2022).

[3] T. Guo, K. Gulati, H. Arora, P. Han, B. Fournier, and S. Ivanovski, “Race to invade: Understanding soft tissue integration at the transmucosal region of titanium dental implants,” Dent. Mater., vol. 37, no. 5, 2021, doi: 10.1016/j.dental.2021.02.005.

[4] A. Al-Noaman, S. C. F. Rawlinson, and R. G. Hill, “MgF2- containing glasses as a coating for titanium dental implant. I- Glass powder,” J. Mech. Behav. Biomed. Mater., vol. 125, 2022, doi: 10.1016/j.jmbbm.2021.104948.

[5] D. P. Utami, D. J. Indrani, and Y. K. Eriwati, “The role of implant surface modification method on the success of osseointegration,” J. Kedokt. Gigi Univ. Padjadjaran, vol. 31, no. 2, 2019, doi: 10.24198/jkg.v31i2.17967.

[6] M. Esposito, J. M. Hirsch, U. Lekholm, and P. Thomsen, “Biological factors contributing to failures of osseointegrated oral implants. (I). Success criteria and epidemiology,” European Journal of Oral Sciences, vol. 106, no. 1. 1998, doi: 10.1046/j.0909-8836..t01-2-.x.

[7] S. E. A. Camargo et al., “Novel coatings to minimize bacterial adhesion and promote osteoblast activity for titanium implants,” J. Funct. Biomater., vol. 11, no. 2, 2020, doi: 10.3390/jfb11020042.

[8] G. Zorn, V. Migonney, and D. G. Castner, “Grafting titanium nitride surfaces with sodium styrene sulfonate thin films,” Biointerphases, vol. 9, no. 3, 2014, doi: 10.1116/1.4878215.

# Chapter 2 - State of the art:

## 1. Introduction:

This chapter provides an overview of dental implants and the current problems they present. The most relevant works in the field are summarized with regard to the most important issues of the present thesis: Development of multifunctional dental implants.

## 2. Dental implants:

Teeth are bony structures with numerous functions. They are used for chewing, participating in speech, and contributing to the owner's aesthetics. Over the years, teeth are exposed to various chemical and physical effects, which lead to the erosion of dental hard tissues, gum regression and other complications, and it is therefore often necessary to resort to their removal. As a result, the demand for dental implants has been increasing [1].

Dental implants are devices inserted preferably in direct contact with the maxillary and/or mandibular bone. They are composed of three main components: a cylindrical screw known as an implant; the abutment that connects the implant to the dental prosthesis; and the crown/prosthesis that is usually customized according to the patient [2], figure 2.

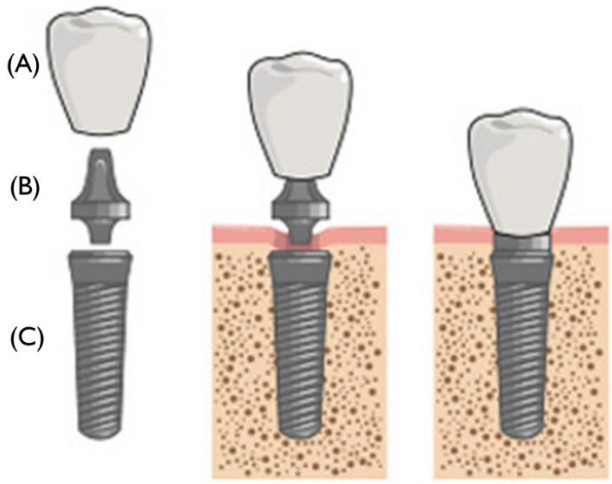


*Figure 2 - Components of restored implant. A, Implant crown. B, Abutment. C, Implant fixture. Adapted [2]*

Currently, they can be manufactured from several materials, each one presenting different advantages and disadvantages, summarized in table 1.

*Table 1 - Various materials choices to fabricate dental abutments [1].*

| **Abutment material** | **Advantages** | **Limitations** |
|---|---|---|
| Gold and alloys | • Mechanically ductile. | • Expensive;<br>• Insufficient chemical stability;<br>• Downgrowth of epithelium. |
| Zirconia | • High chemical stability;<br>• Natural tooth appearance;<br>• Reduced ion leaching. | • Mechanical complications such as fracture and delamination. |
| Aluminum | • Acceptable for mucosal healing; | • Toxicity concerns; |
| Titanium | • Mechanically stable;<br>• Exceptional biocompatibility;<br>• Chemically stable and corrosion resistant. | • Biological inert. |
| Titanium Alloys (Ti-6Al-4V and Ti-6Al-7Nb) | • Good biocompatibility;<br>• Chemically stable. | • Potentially cytotoxic;<br>• Biological inert. |

Due to exceptional corrosion resistance, biocompatibility and mechanical stability, pure titanium and its alloy Ti-6Al-4V are the most commonly used materials in its manufacture [3].

## 3. Titanium-based dental implants:

The main alloy used is called “commercially pure titanium” (cpTi). There are four grades of this metal, numbered from 1 to 4, according to its purity and oxygen content [4]. These differ in properties such as corrosion resistance, ductility, and strength, with grade 4 having the highest oxygen content and the best overall mechanical strength. There is also the Ti-6Al-4V alloy, which can be applied in dentistry due to its high strength and low Young's modulus [5]. Table 2 presents the composition of the different cpTi grades and Ti-6Al-4V alloys.

*Table 2 - Composition and properties of titanium alloys used as implants [4].*

| | **CpTi Grade 1** | **CpTi Grade 2** | **CpTi Grade 3** | **CpTi Grade 4** | **Ti-6Al-4V** |
|---|---|---|---|---|---|
| Titanium at.% | ca 99% | ca 99% | ca 99% | ca 99% | 90% |
| Oxygen at.% | 0.18% | 0.25% | 0.35% | 0.4% | 0.2% max |
| Iron at.% | 0.2% | 0.2% | 0.2% | 0.3% | 0.25% |
| Nitrogen at.% | 0.03% | 0.03% | 0.05% | 0.05% | - |
| Hydrogen at.% | 0.15% | 0.15% | 0.15% | 0.15% | - |
| Carbon at.% | 0.1% | 0.1% | 0.1% | 0.1% | - |
| UTS/MPa | 240 | 340 | 450 | 550 | 900 |
| Yield | | | | | |
| Strength/MPa | 170 | 275 | 380 | 480 | 850 |
| Elongation at Failure/% | 25 | 20 | 18 | 15 | 10 |

One of the problems in using Ti-6Al-4V is the release of aluminum and vanadium, which can cause biological problems, since vanadium is cytotoxic and can cause allergic reactions of grade 4 and aluminum interferes with bone mineralization, causing structural deficiencies [6]. In order to occur these complications, both need to be present in the tissues at significant concentrations. However, the amounts of ion released from this alloy are much lower than those needed to produce cytotoxic effects, being below the average for nutritional uptake, so, studies confirm that this alloy undergoes satisfactory

osseointegration [4] [7] [8], especially when treated to improve the oxide layer on the surface [9].

### 3.1. Biocompatibility of titanium for dental implants:

Corrosive behavior is one of the factors which most influences the biocompatibility of metallic implants. When titanium dental implants are used, the titanium levels in the blood and serum increase, indicating that there is leaching in these devices. Once it enters the bloodstream, titanium can be transported throughout the body and cause allergic reactions [10].

Although titanium alloys have good corrosion resistance, this property can be changed by the presence of proteins such as albumin, increasing the amount of titanium released [11]. However, assessing how much titanium may be released and how harmful it may be is difficult, as several different animal models were used in the published studies, and different approaches were also used. The metal ions that are released by corrosion can both cause adverse effects on the tissue surrounding the implant, depending on the corrosion rate; and systemically, where grade 4 allergic reactions may arise that do not depend on the corrosion rate, but occur simply because there is a release of metal ions. However, these reactions are rare and affect only a small number of patients [12].

The two most used titanium alloys, cpTi and Ti-6Al-4V are bioactive and capable of promoting bone formation in direct contact with the metal. Thus, the interfacial zone between the implant and the bone is critical for the development of osseointegration because it is in this region that bone cells release growth factors, initiating the first steps of bone formation [13]. Liu et al., discuss about which alloy is best for use in dental implants. In general, cpTi is slightly favored, however, in vitro results have found Ti-6Al-4V alloy to be superior. What can be said is that both alloys show minimal corrosion, cause few systemic effects, and biomechanically they are fit for purpose with high clinical survival rates over time. [4].

## 4. Failure of dental implants:

The basic principle of dental implants is osseointegration, in which osteoblastic cells grow and integrate directly into the surface of the implant inserted surgically in the mandible, since the stability of the implant depends on its connection with the bone [14]. Brånemark et al., defined osseointegration as bone cells fully adhered to the implant surface and that the structure and function are directly linked [15]. Broadly, this can be

defined as "the process that results in the direct structural and functional connection between the bone and the implant surface", providing the desired basis for the correct functioning of the dental implant [16].

When exposed to the oral environment, commercially available dental implants still have some limitations [17]. With a survival record of around 98%, implants are often successfully placed; nevertheless, long-term problems are frequent. Mechanical stress caused by osseointegration failure and bacterial infection is the two main causes of dental implants failing over time [18].

### 4.1. Osseointegration Failure:

Osseointegration is the direct functional and structural connection between the living bone tissue and the implant surface. Thus, osseointegration is an extremely important parameter to evaluate the success of an implant in terms of healing and longevity [19]. Although the root of a normal tooth attaches to the bone through the periodontal ligament, which allows a slight movement of the tooth, successful implants are completely fused to the bone and have no mobility. So, one way to see if the implant is correctly integrated with the bone is to apply a force or torque to the implant. If it does not move, it is considered successful; if it does move, the implant is considered a failure and therefore a complication [20].

Slow osseointegration increases the waiting time for loading of the implant into the artificial crown, thus requiring a long post-operative period as the expected healing time is three to six months, which is far from the patients' current expectations [16]. Furthermore, this post-surgical time increases the likelihood of micro-motions and the entry and adhesion of microorganisms in the environment close to the surgical site, specifically on the surface of the dental implant, which may ultimately culminate in an unsuccessful implant [21].

### 4.2.Peri-implantis infection:

Polymicrobial biofilm infections are the main reason for dental implant failure, when polymicrobial biofilm forms on the titanium surface, host immune-mediated responses and inflammatory processes are activated, changing the environmental conditions around the implant. If a deleterious change occurs in the balance of the endogenous microbiome, excessive growth of pathogenic species within the biofilm may

occur leading to progressive destruction of the peri-implant tissue [22]. Thus, infections related to bacterial biofilm can lead to implant and associated prosthetic device failure, requiring implant removal and generating serious problems for the oral health and quality of patient's life [23].

Just as periodontal tissue is essential for the stability of the dentition, healthy peri-implant tissue is essential for the long-term stability of the dental implant [24]. Currently, dental implants present a high prevalence of infections, where more than 40% of them are affected by peri-implant mucositis and more than 22% by peri-implantitis, being the microbial biofilms formed on the surface of the device the main etiological factor for these inflammatory processes [25]. Consequently, it is important to define what a biofilm is an inflammation that results from its formation. A biofilm is a structured community of microbial cells deeply organized and embedded in a self-produced extracellular polymeric matrix firmly adhered to the surface. It represents a survival mechanism that not only provides structural stability and a functional environment but also increases tolerance to antibiotics and immune cells, thus providing a favorable environment for the growth of micro-organisms [26]. Its formation includes several stages: protein adsorption, microbial adhesion, biofilm formation, maturation, and dispersion [27], figure 3.

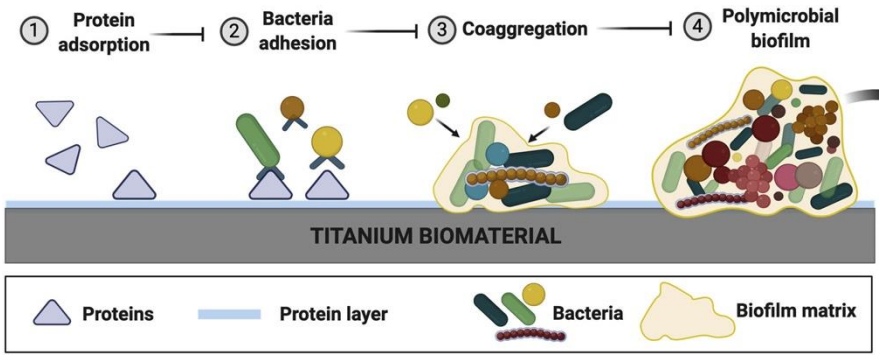


*Figure 3 - Steps of biofilm formation on titanium biomaterial. (1) Adsorption of proteins (2) Initial colonizers adhere to the protein layer. (3) Biofilm accumulation. (4) This synergistic interaction between organisms continues to contribute to the biofilm structure. Adapted [27].*

On the other hand, peri-implant mucositis is characterized by inflammation of the mucosa around the osseointegrated implant, occurring local bleeding, and/or suppuration. This inflammatory reaction is reversible; however, if it is not properly treated, its progression may evolve to peri-implantitis, a more serious inflammatory disease characterized by the progressive loss of the supporting alveolar bone around the implant

[28]. These events are similar to the progression from gingivitis, a reversible disease, to periodontitis that develops on natural teeth in susceptible individuals [29], figure 4.

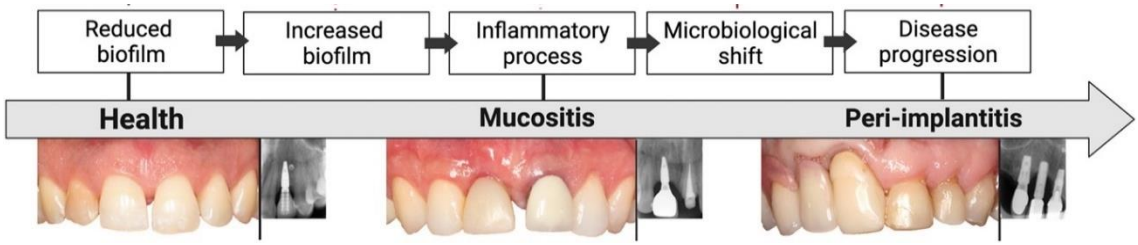


*Figure 4 - Increased biofilm accumulation on implant surfaces results in an inflammatory process that alters the environment, causing a microbiological change and disease progression (red boxes). The microbiological change in biofilms. As a result, peri-implant mucositis clinically transforms into peri-implantitis. Adapted [23].*

## 5. Surface modification:

Implant surface modifications designed to promote osseointegration, combat bacterial infections and increase implant survival rates have been a major focus of biomedical research in the last 30 years. In this sense, many surface modification techniques have been proposed, producing numerous variations on titanium surfaces changing or improving properties such as bioactivity, functionalization and antibacterial activity [23]. Furthermore, changes in the morphology, roughness and surface crystallinity of the implant have been shown to produce excellent results in the speed of healing and the osseointegration process, both in vivo and in vitro [30].

In this context, surface treatments such as acid etching, blasting, anodizing and magnetron sputtering have opened up a range of scientifically proven functionalization and surface modification opportunities, which allow achieving nanostructuring, a property that stimulates cell adhesion, dissemination, and proliferation [31]. Consequently, the characteristics of implant nanomorphology such as hydrophilicity, the drug-loaded surface and the addition of bioactive coatings are the most promising aspects of increasing the success of implants [32].

In the last 10 years, there were several studies with techniques and methodologies to incorporate drugs, proteins, and nanoparticles at the cell/surface interface. On Ti implants, anodization methodologies with the creation of nanotubes and bioactive coatings methodologies have revealed a positive potential to accelerate osseointegration and the behavior of osteoprogenitor cells [30]. figure 5 explains how the process occurs.

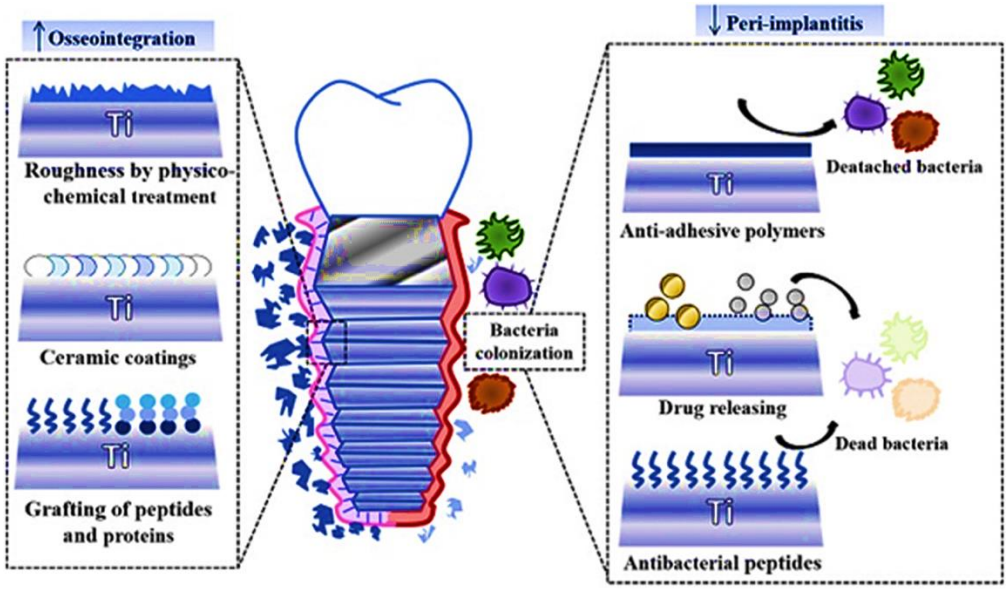


*Figure 5 Scheme of surface functionalisation of dental implants with the aim of improving osseointegration and infection control. Adapted [30].*

Dental implants made of pure titanium are prone to suffering scratches and abrasions during routine oral hygiene procedures. This low resistance to wear induces irrevocable damage to the implant surface, increasing its roughness, which facilitates the adhesion of bacteria and the early formation of biofilms [33]. In addition, these are also known to be intrinsically susceptible to corrosion and ion leaching in physiological environments, generating products that cause many adverse and toxic reactions in host tissues [34]. To overcome these problems, titanium nitride (TiN) coatings have been used since they present promising characteristics such as high hardness; wear resistance; corrosion and erosion resistance; low friction coefficient; no toxicity, and excellent biocompatibility [35]. In addition, TiN-modified surfaces enable various application opportunities, mainly as antimicrobial coatings in food technology and biomedicine through the addition of transition metal nanoparticles, such as zinc (Zn) and silver (Ag) [36].

## 6. Bioactive materials:

As has been discussed, to prevent failures it is necessary to use implants produced with materials that enhance osseointegration processes and at the same time, prevent or suppress bacterial colonization. These materials can present different mechanisms of action. In one hand, they may promote bone tissue formation by favoring the activity of osteoblastic cell or the differentiation of stem cells into osteogenic phenotypes, and in

other hand, their surface properties and composition may interfere with bacterial adhesion and viability, modifying the surface energy or releasing antibacterial agents, such as ions or antibiotics [37]. Ag and Zn nanoparticles, as well as their oxides, AgO and ZnO, prevent initial bacterial attachment, preventing biofilm formation [38]. However, it is important to note that although nanoparticles can kill bacteria and have no cytotoxic effect on osteoblastic and epithelial cells at low concentrations, this cannot be guaranteed at high concentrations. Therefore, it is necessary to develop a suitable coating, i.e., with concentrations that are below the citotoxicity limit [39].

### 6.1. Antibacterial activity Ag nanoparticles:

A nanoparticle can be defined as "an object of very small dimensions that behaves as a whole in terms of its properties". Nanoparticles have among them several important characteristics that can be used to classify them, such as composition, morphology, uniformity, and agglomeration [40]. Furthermore, nanoparticles are classified according to their diameter which can vary from 1 nanometer to 100 nanometers and can correspond to individual molecules or macromolecules that include higher order assemblies in nanoparticles [41]. The size of nanoparticles allows different biological interactions when compared to non-nanostructured materials, due to the surface-to-volume ratio. This property can be exploited to create nanostructures capable of diagnosing and treating numerous pathologies [42].

Silver is a transition metal that is distinguished by having high reflectivity and electrical and thermal conductivity, as well as low emissivity. This material is characterized by having only one crystalline form, presenting a face-centered cubic shape with a lattice constant of a=0.4086 nm [43].

Silver nanoparticles have a high surface/volume ratio and present different morphological characteristics. They can easily penetrate the bacterial cell membrane and act as a catalyst for bacteria destruction. Their antimicrobial properties have been widely studied revealing that there is an inverse relationship between nanoparticle size and antimicrobial activity. Particles in the 1-10 nanometer range have proven to be most effective in fighting bacteria, but smaller particles are also reported to be more toxic and this effect is most noticeable when they are in the oxide form (AgO) [44]. Therefore, reckless or excessive use of silver nanoparticles can result in potential risks to humans and the environment and it is crucial to keep the concentration of free silver nanoparticles below World Health Organization (WHO) permissible limits. [45].

Although the exact mechanisms of the antibacterial effects of nanoparticles have not yet been fully elucidated, several pathways have been proposed. For example, silver nanoparticles can continuously release silver ions that contribute to the death of microbes, due to their affinity for sulfur proteins present in the cell wall and cytoplasmic membrane. The adhering ions increase the permeability of the cytoplasmic membrane and lead to the disruption of the bacterial envelope [46]. Additionally, silver ions trapped free in cells can deactivate respiratory enzymes by generating reactive oxygen species (ROS) and disrupting ATP production. As sulfur and phosphorus are important components of DNA, their interaction with silver ions can cause problems in DNA replication and consequently, cell reproduction. In addition, silver ions can also inhibit protein synthesis by denaturing ribosomes present in the cell cytoplasm [47], figure 6.

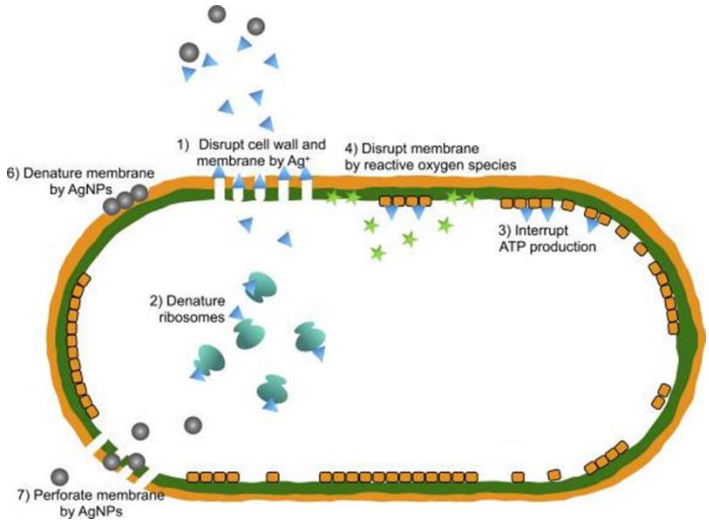


*Figure 6 - The antibacterial actions of silver nanoparticles (AgNPs) [48].*

## 6.2. Antibacterial activity Zn nanoparticles:

To date, zinc has been used in oral hygiene products as an antimicrobial agent to control dental plaque, inhibit the formation of colonies and reduce halitosis. Lately, it has been incorporated into many dental materials due to the zinc ion's ability to inhibit the growth of bacteria however, it is considered a bacteriostatic agent and not bactericidal, as its effect is reversed when the cells are washed out [49].

Zinc ions have multiple inhibitory effects on bacterial cell activity, such as on glycolysis, glycosyltransferase production and polysaccharide synthesis, transmembrane proton translocation, and tolerance to acidic environments. They can increase bacterial cell membrane permeability to protons, reduce adenosine triphosphate (ATP) synthesis

in glucose-forming cells, and decrease F-type adenosine triphosphate (F-ATPase) activity due to their ability to inhibit the glycolytic enzymes glyceraldehyde-3-phosphate dehydrogenase and pyruvate kinase, as well as phosphoenolpyruvate [50].

Its oxidized form (ZnO), on the other hand, has also been studied, and is a biosafety material, non-toxic to human cells [51]. ZnO nanoparticles can disrupt bacterial growth by interacting with the bacterial surface or by entering the interior of the bacteria. This leads to the disruption of bacterial enzyme systems by displacing magnesium ions essential for the enzymatic activity of bacteria and subsequently showing a significant bactericidal effect [52].

## 7. References:


[1] M. S. Zafar, S. Najeeb, and Z. Khurshid, “Introduction to dental implants materials, coatings, and surface modifications,” in Dental Implants: Materials, Coatings, Surface Modifications and Interfaces with Oral Tissues, 2020. doi: 10.1016/B978-0-12-819586-4.00001-9

[2] “Section I Introduction,” J. Oral Maxillofac. Surg., vol. 75, no. 2, p. 2, Feb. 2017, doi: 10.1016/j.joms.2016.09.029.

[3] T. Guo, K. Gulati, H. Arora, P. Han, B. Fournier, and S. Ivanovski, “Race to invade: Understanding soft tissue integration at the transmucosal region of titanium dental implants,” Dent. Mater., vol. 37, no. 5, 2021, doi: 10.1016/j.dental.2021.02.005.

[4] X. Liu, S. Chen, J. K. H. Tsoi, and J. P. Matinlinna, “Binary titanium alloys as dental implant materials-a review,” Regenerative Biomaterials, vol. 4, no. 5. 2017, doi: 10.1093/rb/rbx027.

[5] C. N. Elias, D. J. Fernandes, F. M. De Souza, E. D. S. Monteiro, and R. S. De Biasi, “Mechanical and clinical properties of titanium and titanium-based alloys (Ti G2, Ti G4 cold worked nanostructured and Ti G5) for biomedical applications,” J. Mater. Res. Technol., vol. 8, no. 1, 2019, doi: 10.1016/j.jmrt.2018.07.016.

[6] J. P. Thyssen, S. S. Jakobsen, K. Engkilde, J. D. Johansen, K. Søballe, and T. Menné, “The association between metal allergy, total hip arthroplasty, and revision,” Acta Orthop., vol. 80, no. 6, 2009, doi: 10.3109/17453670903487008.

[7] M. McCracken, “Dental implant materials: Commercially pure titanium and titanium alloys,” J. Prosthodont., vol. 8, no. 1, 1999, doi: 10.1111/j.1532-849X.1999.tb00006.x.

[8] L. C. Zhang and L. Y. Chen, “A Review on Biomedical Titanium Alloys: Recent Progress and Prospect,” Advanced Engineering Materials, vol. 21, no. 4. 2019, doi: 10.1002/adem.201801215.

[9] O. G. Bodelón, C. Clemente, M. A. Alobera, S. Aguado-Henche, M. L. Escudero, and M. C. G. Alonso, “Osseointegration of TI6Al4V dental implants modified by thermal oxidation in osteoporotic rabbits,” Int. J. Implant Dent., vol. 2, no. 1, 2016, doi: 10.1186/s40729-016-0051-5.

[10] M. Temiz, E. Dayi, and N. Saruhan, “Evaluation of blood titanium levels and total bone contact area of dental implants,” Biomed Res. Int., vol. 2018, 2018, doi: 10.1155/2018/4121639.

[11] F. Yu, O. Addison, and A. J. Davenport, “A synergistic effect of albumin and H2O2 accelerates corrosion of Ti6Al4V,” Acta Biomater., vol. 26, 2015, doi: 10.1016/j.actbio.2015.07.046.

[12] M. S. Patton, T. D. B. Lyon, and G. P. Ashcroft, “Levels of systemic metal ions in patients with intramedullary nails,” Acta Orthop., vol. 79, no. 6, 2008, doi: 10.1080/17453670810016911.

[13] D. Apostu et al., “Systemic drugs that influence titanium implant osseointegration,” Drug Metabolism Reviews, vol. 49, no. 1. 2017, doi: 10.1080/03602532.2016.1277737.

[14] M. C. Pan, H. P. Lin, and C. S. Chen, “Design/exploration and verification of an electromagnetic probe for assessing dental implant osseointegration,” Meas. J. Int. Meas. Confed., vol. 174, 2021, doi: 10.1016/j.measurement.2021.109054.

[15] P. I. Brånemark, U. Breine, R. Adell, B. O. Hansson, J. Lindström, and A. Ohlsson, “Intra-osseous anchorage of dental prostheses: I. Experimental studies,” Scand. J. Plast. Reconstr. Surg. Hand Surg., vol. 3, no. 2, 1969, doi: 10.3109/02844316909036699.

[16] J. Li, J. A. Jansen, X. F. Walboomers, and J. J. van den Beucken, “Mechanical aspects of dental implants and osseointegration: A narrative review,” Journal of the Mechanical Behavior of Biomedical Materials, vol. 103. 2020, doi: 10.1016/j.jmbbm.2019.103574.

[17] R. C. Costa et al., “Microbial Corrosion in Titanium-Based Dental Implants: How Tiny Bacteria Can Create a Big Problem?,” J. Bio- Tribo-Corrosion, vol. 7, no. 4, 2021, doi: 10.1007/s40735-021-00575-8.

[18] A. D. Pye, D. E. A. Lockhart, M. P. Dawson, C. A. Murray, and A. J. Smith, “A review of dental implants and infection,” Journal of Hospital Infection, vol. 72, no. 2. 2009, doi: 10.1016/j.jhin.2009.02.010.

[19] J. Wirth, M. Tahriri, K. Khoshroo, M. Rasoulianboroujeni, A. R. Dentino, and L. Tayebi, “Surface modification of dental implants,” in Biomaterials for Oral and Dental Tissue Engineering, 2017.

[20] K. Liaw, R. H. Delfini, and J. J. Abrahams, “Dental Implant Complications,” Semin. Ultrasound, CT MRI, vol. 36, no. 5, 2015, doi: 10.1053/j.sult.2015.09.007.

[21] C. F. Almeida Alves, A. Cavaleiro, and S. Carvalho, “Bioactivity response of Ta1-xOx coatings deposited by reactive DC magnetron sputtering,” Mater. Sci. Eng. C, vol. 58, 2016, doi: 10.1016/j.msec.2015.08.017.

[22] G. N. Belibasakis and D. Manoil, “Microbial Community-Driven Etiopathogenesis of Peri-Implantitis,” Journal of Dental Research, vol. 100, no. 1. 2021, doi: 10.1177/0022034520949851.

[23] R. C. Costa et al., “Fitting pieces into the puzzle: The impact of titanium-based dental implant surface modifications on bacterial accumulation and polymicrobial infections,” Advances in Colloid and Interface Science, vol. 298. 2021, doi: 10.1016/j.cis.2021.102551.

[24] C. T. Lee, Y. W. Huang, L. Zhu, and R. Weltman, “Prevalences of peri-implantitis and peri-implant mucositis: systematic review and meta-analysis,” Journal of Dentistry, vol. 62. 2017, doi: 10.1016/j.jdent.2017.04.011.

[25] G. E. Salvi, R. Cosgarea, and A. Sculean, “Prevalence and Mechanisms of Peri-implant Diseases,” J. Dent. Res., vol. 96, no. 1, 2017, doi: 10.1177/0022034516667484.

[26] L. Karygianni, Z. Ren, H. Koo, and T. Thurnheer, “Biofilm Matrixome: Extracellular Components in Structured Microbial Communities,” Trends in Microbiology, vol. 28, no. 8. 2020, doi: 10.1016/j.tim.2020.03.016.

[27] J. G. S. Souza, M. M. Bertolini, R. C. Costa, B. E. Nagay, A. Dongari-Bagtzoglou, and V. A. R. Barão, “Targeting implant-associated infections: titanium surface loaded with antimicrobial,” iScience, vol. 24, no. 1. 2021, doi: 10.1016/j.isci.2020.102008.

[28] G. A. Kotsakis and D. G. Olmedo, “Peri-implantitis is not periodontitis: Scientific discoveries shed light on microbiome-biomaterial interactions that may determine disease phenotype,” Periodontology 2000, vol. 86, no. 1. 2021, doi: 10.1111/prd.12372.

[29] G. Körtvélyessy, T. Tarjányi, Z. L. Baráth, J. Minarovits, and Z. Tóth, “Bioactive coatings for dental implants: A review of alternative strategies to prevent peri-implantitis induced by anaerobic bacteria,” Anaerobe, vol. 70. 2021, doi: 10.1016/j.anaerobe.2021.102404.

[30] M. F. Kunrath, “Customized dental implants: Manufacturing processes, topography, osseointegration and future perspectives of 3D fabricated implants,” Bioprinting, vol. 20. 2020, doi: 10.1016/j.bprint.2020.e00107.

[31] S. H. Choi et al., “Effect of wet storage on the bioactivity of ultraviolet light- and non-thermal atmospheric pressure plasma-treated titanium and zirconia implant surfaces,” Mater. Sci. Eng. C, vol. 105, 2019, doi: 10.1016/j.msec.2019.110049.

[32] R. Rasouli, A. Barhoum, and H. Uludag, “A review of nanostructured surfaces and materials for dental implants: Surface coating, patterning and functionalization for improved performance,” Biomaterials Science, vol. 6, no. 6. 2018, doi: 10.1039/c8bm00021b.

[33] X. Shi, L. Xu, M. L. Munar, and K. Ishikawa, “Hydrothermal treatment for TiN as abrasion resistant dental implant coating and its fibroblast response,” Mater. Sci. Eng. C, vol. 49, 2015, doi: 10.1016/j.msec.2014.12.059.

[34] A. Jemat, M. J. Ghazali, M. Razali, and Y. Otsuka, “Surface modifications and their effects on titanium dental implants,” BioMed Research International, vol. 2015. 2015, doi: 10.1155/2015/791725.

[35] S. Datta, M. Das, V. K. Balla, S. Bodhak, and V. K. Murugesan, “Mechanical, wear, corrosion and biological properties of arc deposited titanium nitride coatings,” Surf. Coatings Technol., vol. 344, 2018, doi: 10.1016/j.surfcoat.2018.03.019.

[36] V. Jokanović et al., “Detailed phisyco-chemical characterization of the multilayered thin films based on titanium oxynitride and copper doped titanium nitride obtained by different PVD techniques,” Vacuum, vol. 195, 2022, doi: 10.1016/j.vacuum.2021.110708.

[37] G. Asensio, B. Vázquez-Lasa, and L. Rojo, “Achievements in the topographic design of commercial titanium dental implants: Towards anti-peri-implantitis surfaces,” Journal of Clinical Medicine, vol. 8, no. 11. 2019, doi: 10.3390/jcm8111982.

[38] O. Depablos-Rivera, C. Sánchez-Aké, R. Álvarez-Mendoza, T. García-Fernández, S. Muhl, and M. Villagrán-Muniz, “Hybrid magnetron sputtering and pulsed laser ablation for the deposition of composite ZnO-Au films,” Thin Solid Films, vol. 685, 2019, doi: 10.1016/j.tsf.2019.06.006.

[39] J. Hardes et al., “The influence of elementary silver versus titanium on osteoblasts behaviour in vitro using human osteosarcoma cell lines,” Sarcoma, vol. 2007, 2007, doi: 10.1155/2007/26539.

[40] J. Njuguna, F. Ansari, S. Sachse, V. M. Rodriguez, S. Siqqique, and H. Zhu, “Nanomaterials, nanofillers, and nanocomposites: types and properties,” in Health and Environmental Safety of Nanomaterials, 2021.

[41] L. Leon, E. J. Chung, and C. Rinaldi, “A brief history of nanotechnology and introduction to nanoparticles for biomedical applications,” in Nanoparticles for

Biomedical Applications: Fundamental Concepts, Biological Interactions and Clinical Applications, 2019.

[42] J. L. Paris and M. Vallet-Regí, “Nanostructures for imaging, medical diagnostics and therapy,” in Fundamentals of Nanoparticles: Classifications, Synthesis Methods, Properties and Characterization, 2018.

[43] The Chemistry of Copper, Silver and Gold. 1973.

[44] R. P. Allaker and K. Memarzadeh, “Nanoparticles and the control of oral infections,” International Journal of Antimicrobial Agents, vol. 43, no. 2. 2014, doi: 10.1016/j.ijantimicag.2013.11.002.

[45] R. K. Kunkalekar, “Role of Oxides (Fe3O4, MnO2) in the Antibacterial Action of Ag-Metal Oxide Hybrid Nanoparticles,” in Noble Metal-Metal Oxide Hybrid Nanoparticles: Fundamentals and Applications, 2018.

[46] S. Khorrami, A. Zarrabi, M. Khaleghi, M. Danaei, and M. R. Mozafari, “Selective cytotoxicity of green synthesized silver nanoparticles against the MCF-7 tumor cell line and their enhanced antioxidant and antimicrobial properties,” Int. J. Nanomedicine, vol. 13, 2018, doi: 10.2147/IJN.S189295.

[47] N. Durán, G. Nakazato, and A. B. Seabra, “Antimicrobial activity of biogenic silver nanoparticles, and silver chloride nanoparticles: an overview and comments,” Applied Microbiology and Biotechnology, vol. 100, no. 15. 2016, doi: 10.1007/s00253-016-7657-7.

[48] I. X. Yin, J. Zhang, I. S. Zhao, M. L. Mei, Q. Li, and C. H. Chu, “The antibacterial mechanism of silver nanoparticles and its application in dentistry,” International Journal of Nanomedicine, vol. 15. 2020, doi: 10.2147/IJN.S246764.

[49] M. M. Almoudi, A. S. Hussein, M. I. Abu Hassan, and N. Mohamad Zain, “A systematic review on antibacterial activity of zinc against Streptococcus mutans,” Saudi Dental Journal, vol. 30, no. 4. 2018, doi: 10.1016/j.sdentj.2018.06.003.

[50] T. N. Phan, T. Buckner, J. Sheng, J. D. Baldeck, and R. E. Marquis, “Physiologic actions of zinc related to inhibition of acid and alkali production by oral streptococci in suspensions and biofilms,” Oral Microbiol. Immunol., vol. 19, no. 1, 2004, doi: 10.1046/j.0902-0055.2003.00109.x.

[51] A. Sirelkhatim et al., “Review on zinc oxide nanoparticles: Antibacterial activity and toxicity mechanism,” Nano-Micro Letters, vol. 7, no. 3. 2015, doi: 10.1007/s40820-015-0040-x.

[52] S. Tavassoli Hojati et al., “Antibacterial, physical and mechanical properties of flowable resin composites containing zinc oxide nanoparticles,” Dent. Mater., vol. 29, no. 5, 2013, doi: 10.1016/j.dental.2013.03.011.

# Chapter 3 – Coatings deposition TiN-Ag and TiN-Zn:

## 1. Introduction:

As already discussed, dental implants are usually manufactured with Ti-based materials due to their biocompatibility and strong corrosion resistance. Currently, Ti-6Al-4V is the most commonly used alloy for this application due to its higher corrosion resistance. However, the low bioactivity, and the ease of microorganisms colonizing the surface are major limitations of this material [1]. Thus, the current challenge in this field is to develop a multifunctional coating that could improve osseointegration capacity and enhance the antibacterial activity.

This chapter presents a description of the chosen deposition method of TiN-Ag and TiN-Zn films and the respective deposition parameters.

## 2. Physical Vapor Deposition (PVD) Technology:

Plasma-based physical vapor deposition (PVD) methods have achieved a wide range of industrial applications. Vapor deposition comprises three steps: (I) the creation of the gaseous species; (II) the transport of the species to the substrate; (III) and his condensation on the substrate surface to form a coating [2].

In the present work, and considering the requirements for dental implants, it is important to achieve coatings with high adhesion and excellent chemical and biological properties. In this sense, the deposition of TiN-Ag and TiN-Zn films was performed using the reactive magnetron sputtering technique, which consists of the junction of two sputtering techniques: reactive sputtering and sputtering in magnetron [3].

## 3. Cathodic sputtering:

In plasma based PVD processes, the deposition species are vaporized by thermal evaporation or by sputtering from a source (the cathode target) through the bombardment of ions [4]. Sputter deposition has been known for decades as a flexible, reliable, and effective coating method as it enables films with high density, smooth surface, excellent adhesion, high hardness, good thickness uniformity, stoichiometry and reproducibility [5].

Reactive sputtering consists of sputtering an elemental target in the presence of a gas that will react with the target material to form a compound. In a sense, all sputtering is reactive because there are always residual gases in the deposition chamber that will react with the sprayed species. However reactive sputtering occurs when a gas is

purposely added to the spray chamber to react with the material [6]. In this deposition process, the metal is conducted in the form of atomic vapor to condense on the surface of the object to be coated. The non-metallic element is introduced in the process in the form of a gas that can react with the condensed metal and a chemical reaction between the two constituents defines the formation of the compound [7].

In this sense, sputtering starts with plasma formation by applying an electric field between the cathode (target) and anode (substrate) in a non-reactive atmosphere in a low vacuum environment. In this way, gaseous species present in the chamber are induced by the potential difference to form a glow discharge or plasma. The electric field promotes the acceleration of charged particles that ensure the collision and the transfer of momentum to the target, causing its pulverization and producing secondary electrons that ensure the ionization of the non-reactive species and the maintenance of the plasma [8].

However, it is important to bear in mind that there is a minimum voltage required to create the plasma, known as the breakdown voltage, otherwise, the reactive species do not acquire enough kinetic energy to ionize and create charged particles. Typically, the non-reactive gas used in ionization is argon, due to its availability in the market, low cost, and atomic weight, which allows high momentum transfer, increasing the sputtering yield [9]. Finally, the ions removed from the target condense on the substrate surface and then nucleation and coalescence phenomena lead to the formation of a thin film [10]. Although many materials have been successfully deposited, this process still has limitations such as low deposition rate, low ionization efficiency in the plasma, and high substrate heating effects [11].

Another factor to take into account is that due to the variety of reactive gases that can be added to produce coatings with different compositions, modifying the reactive atmosphere (i.e., in this work, the ratio between Ar and $N_2$), makes the control of the deposition parameters extremely important to optimize the final properties of the coatings, namely the chemical state, structure and morphology [12].

One of the main concerns, is the presence of instabilities that are typically associated with a wrong selection of the experimental parameters. Therefore, voltage hysteresis analysis is a very useful method to understand the influence of the gas flow rate on the plasma discharge by the evolution of the cathodic voltage with the increased partial pressure of the reactive gas. A typical hysteresis curve displays three different zones that correspond to two deposition modes: I) metallic mode and II) reactive mode [13].

In the metallic mode the deposition occurs with no or low reactive gas flow. The target surface maintains a metallic character and has an associated low discharge voltage. The pulverized metal atoms of the target react with the reactive gas on the surface of the substrate forming typically sub-stoichiometric compounds [14].

On the other hand, when a higher reactive gas flow rate is used, the depositions pass to the reactive mode. This means that the reactivity of the plasma with the metal target is higher and induces the formation of a TiN (when the reactive gas is the nitrogen and de target is de titanium) film on the target surface through chemisorption and/or nitrogen implantation. This process is known as "target poisoning" and leads to higher discharge voltages. The increased reactivity of the target surface is generally associated with a decrease in the effective yield of secondary electron emission, which for a constant current density result in a significant direct dependence of the target voltage on the reactive gas flow. At this stage, the sputtering of the existing TiN film on the substrate surface competes with the sputtering of pure metal atoms, reducing the total sputtering yield. In addition, the appearance of a new layer on the target surface contributes to lowering the deposition rate [15]. Between these two modes of deposition, a transition zone with an intermediate behavior appears. In this transition zone, the reactive species can partially react with the sprayed atoms on the substrate surface, in the plasma atmosphere, and finally on the target surface, associated with a progressive increase of the voltage and discharge. This zone is highly unstable, which reinforces the appearance of a mixture of phases during the deposition of coating [16].

### 3.1. Magnetron System:

The sputtering system using a magnetron source was the solution to improve the low deposition rates, due to the low efficiency of the plasma ionization and the high substrate temperature. By creating a magnetic field perpendicular to the electric field and parallel to the target surface, the magnetrons force the secondary electrons to stay in their vicinity and travel along the field lines in a helical path, thus substantially increasing the probability of ionization and electron-atom collision. The increased ionization yield near the magnetrons creates denser plasma in the target region, leading to an increase of the ion bombardment of the target and, in turn, higher deposition rates [17]. Furthermore, the bombardment of the sample holder with secondary electrons leads to an increase in its temperature, as well as causes re-spraying from the growing film, creating defects. By applying a negative bias voltage to the sample holder (BIAS), it is possible to minimize

this effect and increase the deposition efficiency. However, magnetron sputtering has the disadvantage that the use of the target material is reduced, causing deformation (“trakes”). This denomination is caused by the interaction of both the magnetic and electric fields, causing the region where the plasma is concentrated to be only a small portion of the total surface area of the target. This concentration leads to the formation of erosion "tracks", causing much higher wear in this area. So typically, in the conventional magnetron, only 25-30% of the total target material is expected to be pulverized [17], figure 18.

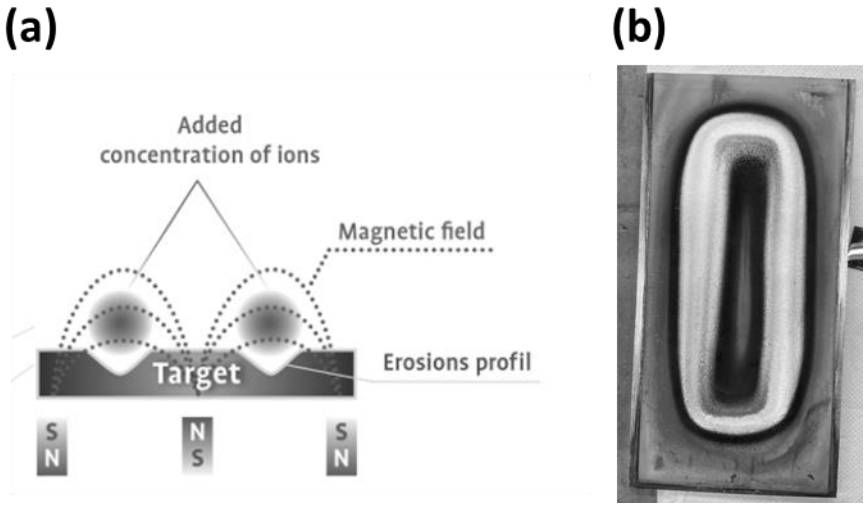


*Figure 7 - More material is locally eliminated as more ions are produced in the permanent magnets' magnetic field.. (a) Cross-section diagram of the target [18]; (b) Silver target at the end of the depositions.*

In magnetron sputtering, there are different ways of adjusting the magnetrons to maximize the deposition yield.

### 3.2. Unbalanced magnetron sputtering:

The main difference between conventional and unbalanced magnetrons is in the degree to which the plasma is confined. In a conventional magnetron, the plasma is tightly confined to the target region, with a region of dense plasma extending about 60 nm in front of the target. During film growth, substrates positioned within this region are subjected to ion bombardment, which can strongly modify the structure and properties of the resulting film. Substrates positioned outside this high plasma density region experience insufficient ion bombardment to modify the microstructure of the growing film and, therefore, it is difficult to produce fully dense, high-quality coatings on large, complex components using conventional magnetron [11].

In the unbalanced configuration, not all field lines are closed between the central and outer poles of the magnetron some are directed toward the substrate, and part of the secondary electrons can follow those field lines. Consequently, the plasma is not strongly confined to the target region, flowing also towards the substrate. Thus, high ionic currents are drawn from the plasma without the need to external polarization of the substrate [19]. Windowns e Savvides et al. [20] evaluated the importance when systematically varying the magnetic configuration of the conventional magnetron [20]. They have demonstrated that ionic current densities on the substrate exceeding 5mA/cm$^2$ can be generated using an unbalanced, i.e., asymmetric magnetron. Furthermore, in the conventional process, the plasma is tightly confined to the target region becoming extremely dense (about 60mm in front of the target). Substrates placed outside this region are in an insufficient ion bombardment zone, making it difficult to densify the coating [21].

The unbalanced magnetron design discussed above was called "type 2" by Window and Savvides et al. [20]. However, they also considered the opposite case ("type 1"), where the central pole was strengthened relative to the outer pole. In this configuration, the field lines do not close and are directed towards the chamber walls and the plasma density in the substrate region is low [17]. A comparison between the plasma confinement obtained in the different plasma configurations is shown schematically in figure 19.

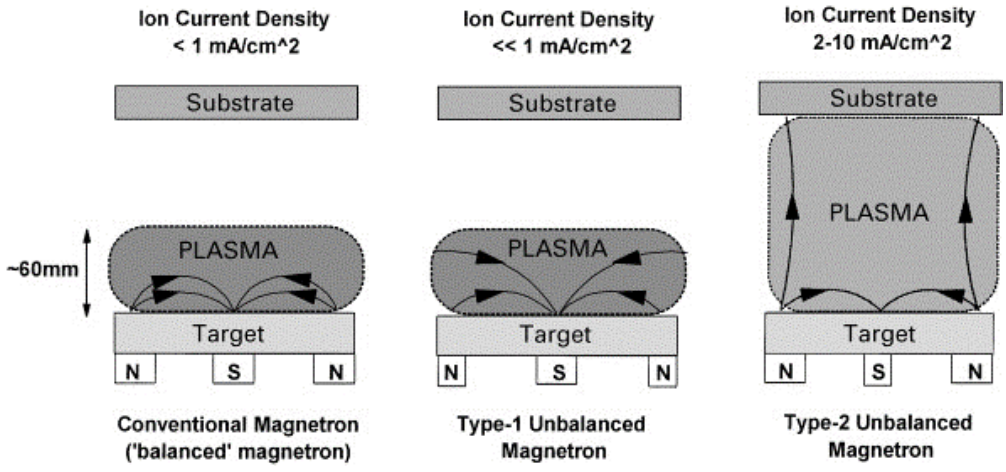


*Figure 8 - Schematic representation of the plasma confinement observed in conventional and unbalanced magnetrons [17].*

### 3.3. Closed-field unbalanced magnetron sputtering:

Deposition of uniform coatings of complex components using a single spray target with an unbalanced magnetron source can be difficult, hence the choice of a multiple-target system. By installing two unbalanced magnetrons opposite each other, the magnet arrays can be configured with either identical or opposite polarities. In the first case, the configuration is described as "mirrored" and in the second case, "closed-field", as it can be seen in figure 20 [17].

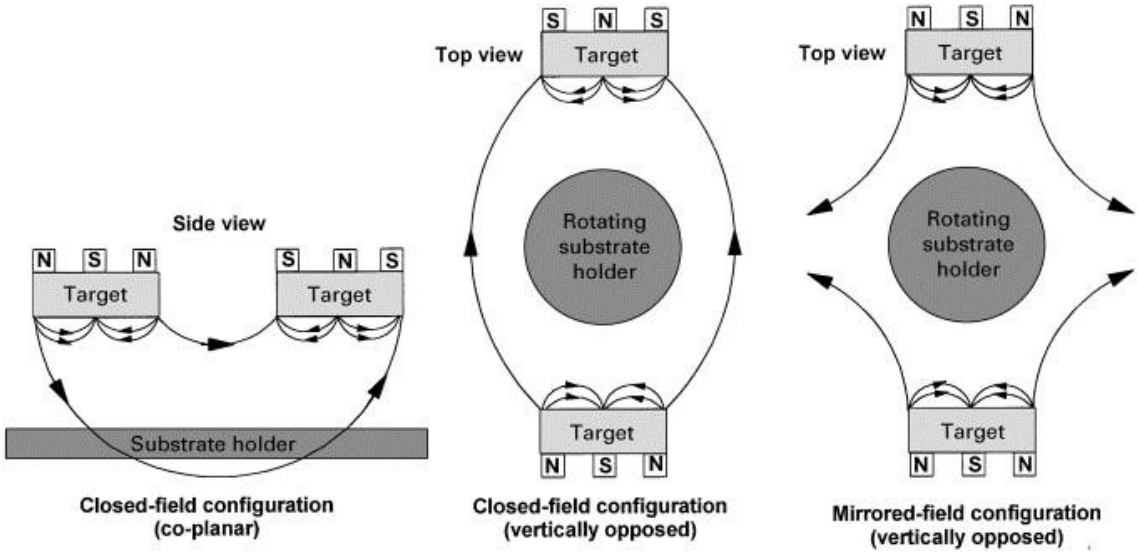


*Figure 9 - Dual unbalanced magnetron configurations [17]*

In the mirrored configuration, the field lines are directed towards the chamber walls. Consequently, the secondary electrons following these field lines are lost, leading to a low plasma density in the substrate region. On the other hand, in the "closed-field" configuration, the field lines are connected between the magnetrons. This configuration keeps the plasma density in the substrate region since few electrons are lost in the chamber walls. Thus, during the deposition process, it is possible to reach high levels of bombardment, with a rate of ions per atom 2-3 times higher than those obtained in the previous configurations referred [22].

## 4. Coatings deposition: TiN-Ag and TiN-Zn:

## 4.1. Equipment used in the production of the coatings:

The deposition chamber used in the production of the different coatings is in the Functional Coatings Laboratory II, of the Physics Department of the University of Minho, Azurém campus, figure 21.

*Figure 10 - Reactive magnetron sputter equipment from the University of Minho.*

In this deposition chamber, there are two opposite rectangular targets measuring 200 mm x 100 mm. For the realization of this work, one of them corresponds to pure titanium (99.99%) and the other to the element to incorporate in the film (Ag (99.99%), Zn (99.99%)). Next to the inner wall of the chamber and along its entire perimeter, there is a distributor tube that injects the gases used during the depositions (Ar and $N_2$). The chamber is heated by an electric resistance and an attempt has been made to maintain a temperature of 200 ºC.

For each series of depositions, were used, Ti-6Al-4V, Si and glass substrates, was fixed to the sample holder (hexagonal prism) using assemblies with conductive polyimide tape (Kapton tape) and copper wires to improve conductivity. The distance between the targets and the sample holder was constate at 70 mm, and the holder was always rotating at a clockwise speed of 7 rpm during the depositions.

## 4.2. Preparation of the substrates:

The depositions were performed on Ti-6Al-4V, silicon, and glass substrates. The previous preparation conditions of the substrates are described below.

### 4.2.1. Ti-6Al-4V substrates:

Before being mounted on the sample holder the Ti-6Al-4V substrates were ultrasonically cleaned in water and detergent, distilled water, acetone, and isopropyl alcohol, during 10 minutes for each solvent. Finally, they were grouped in groups of 15/16 substrates. Finally, 5 groups were glued on the sample holder, one group per face, with Kapton tape together with a copper wire connecting all of them to improve the conductivity of the substrates, figure 22.


*Figure 11 - Preparation of the substrates.*

### 4.2.2. Silicon substrates:

A silicon wafer was cut into squares with a diamond tip. Subsequently, these were ultrasonically cleaned with isopropyl alcohol in a for 10 minutes. Finally, these were also grouped, in groups of 4 and glued to one face of the sample holder with Kapton tape and a copper wire.

### 4.2.3. Glass substrates:

The glass was cleaned with isopropyl alcohol and taped to the display case with Kapton tape.

## 4.3. Deposition Parameters of TiN, TiN-Ag, and TiN-Zn coatings:

The deposition of TiN, TiN-Ag, and TiN-Zn films followed four steps: first, etching was performed to clean the substrates and the targets inside the deposition chamber; then, two interlayers, one of Ti and other of TiN, were produced to improve the adhesion of the films to the substrates; and finally, the films were deposited. The parameters used in each step are detailed below.

### 4.3.1. Etching:

In this step, the argon flow rate was maintained at 80 sccm and a DC pulsed source was used to apply a current of 300 mA to the sample holder, in pulses with a duration of 1536 ns at a frequency of 200 kHz for 15 minutes; A DC source was connected to the titanium target with a current density of 0.08 A and, for doped coatings, a current density of 0.01 A (DC) was also applied to the Ag or Zn target.

### 4.3.2. Interlayers:

To improve the adhesion of the coatings, interlayers were deposited, for the TiN coating only one Ti interlayer was deposited. In TiN-Ag and TiN-Zn coatings, two interlayers were deposited, one of Ti and one of TiN, figure 23.

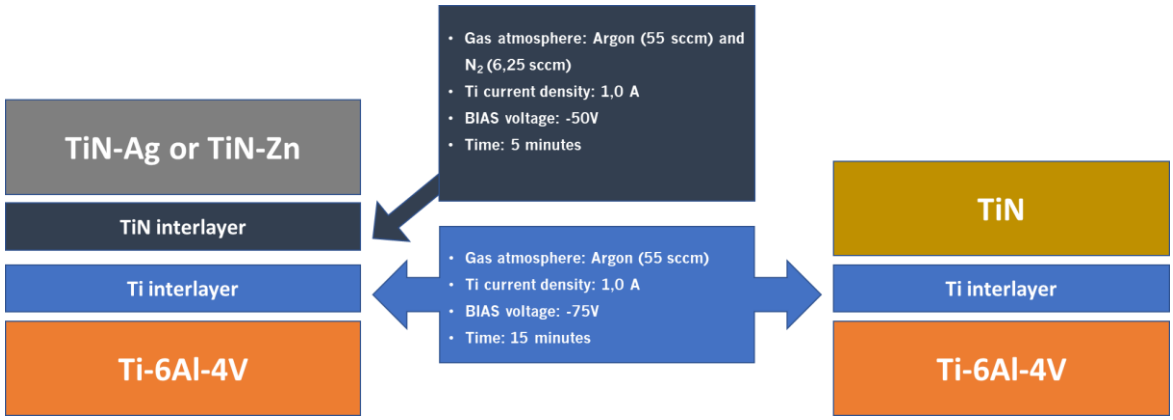


*Figure 12 - Schematic representation and parameters of deposited interlayers.*

The Ti interlayer was deposited by applying a DC current density of 1.0 A was applied to the Ti target and a BIAS voltage of -75V to the substrate holder for 15 minutes. The argon flow rate was maintained at 55 sccm.

The TiN interlayer was deposited by applying a DC current density of 1.0 A on the Ti target and a BIAS voltage of -50V on the substrate holder for 5 minutes, with the flow rates of argon and $N_2$ maintained at 55 sccm and 6.25 sccm, respectively.

### 4.3.3. Deposition:

The deposition parameters of TiN, TiN-Ag, and TiN-Zn films are summarized in table 4. They can also be found in annex 1, where they are presented in more detail. Due to the deposition rates of silver and zinc, it was decided to use a pulsed dc power supply to apply current to these targets to obtain better control over the content of the dopant

material to be incorporated. In addition, the BIAS potential was adjusted from -75 V for pure TiN deposition, to -50 V for coatings incorporated with nanoparticles, since in previous TiN-Ag deposition studies, it was found that a BIAS of -75 V leads to too high TiN-Ag contents in the TiN-Ag film. The system was programmed to maintain a constant current on the targets for all depositions.

*Table 3 - Summarized deposition parameters of TiN, TiN-Ag, and TiN-Zn coatings.*

| **Coating** | **Top layer** | **Interlayer** | | **Gas flow (sccm)** | | **Deposition time (h)** | **Temperature (ºC)** | **Current density ($mA/cm^2$)** | | |
|---|---|---|---|---|---|---|---|---|---|---|
| | | **Ti** | **TiN** | **Ar** | **$N_2$** | | | **Ti** | **Ag** | **Zn** |
| **TiN** | TiN | ✓ | X | 55 | 6.25 | 2 | ≈ 200 | 10 | X | X |
| **TiN-Ag 0.15** | TiN-Ag | ✓ | ✓ | 55 | 6.25 | 1.5 | ≈ 200 | 10 | 0.75 | X |
| **TiN-Ag 0.18** | TiN-Ag | ✓ | ✓ | 55 | 6.25 | 1.5 | ≈ 200 | 10 | 0.90 | X |
| **TiN-Ag 0.21** | TiN-Ag | ✓ | ✓ | 55 | 6.25 | 1.5 | ≈ 200 | 10 | 1.05 | X |
| **TiN-Zn 0.18** | TiN-Zn | ✓ | ✓ | 55 | 6.25 | 1.5 | ≈ 200 | 10 | X | 0.90 |
| **TiN-Zn 0.25** | TiN-Zn | ✓ | ✓ | 55 | 6.25 | 1.5 | ≈ 200 | 10 | X | 1.25 |
| **TiN-Zn 0.32** | TiN-Zn | ✓ | ✓ | 55 | 6.25 | 1.5 | ≈ 200 | 10 | X | 1.60 |

## 5. References:


[1] M. P. Mughal et al., “Surface modification for osseointegration of Ti6Al4V ELI using powder mixed sinking EDM,” J. Mech. Behav. Biomed. Mater., vol. 113, 2021, doi: 10.1016/j.jmbbm.2020.104145.

[2] S. M. Rossnagel, “Thin film deposition with physical vapor deposition and related technologies,” J. Vac. Sci. Technol. A Vacuum, Surfaces, Film., vol. 21, no. 5, 2003, doi: 10.1116/1.1600450.

[3] X. Q. Tan, J. Y. Liu, J. R. Niu, J. Y. Liu, and J. Y. Tian, “Recent progress in magnetron sputtering technology used on fabrics,” Materials, vol. 11, no. 10. 2018, doi: 10.3390/ma11101953.

[4] D. Lundin, J. T. Gudmundsson, and T. Minea, High power impulse magnetron sputtering : Fundamentals, technologies, challenges and applications. 2019.

[5] Y. Deng, W. Chen, B. Li, C. Wang, T. Kuang, and Y. Li, “Physical vapor deposition technology for coated cutting tools: A review,” Ceramics International, vol. 46, no. 11. 2020, doi: 10.1016/j.ceramint.2020.04.168.

[6] W. D. Sproul, D. J. Christie, and D. C. Carter, “Control of reactive sputtering processes,” Thin Solid Films, vol. 491, no. 1–2. 2005, doi: 10.1016/j.tsf.2005.05.022.

[7] R. P. Howson, “The reactive sputtering of oxides and nitrides,” Pure Appl. Chem., vol. 66, no. 6, 1994, doi: 10.1351/pac199466061311.

[8] V. Jokanović et al., “Detailed phisyco-chemical characterization of the multilayered thin films based on titanium oxynitride and copper doped titanium nitride obtained by different PVD techniques,” Vacuum, vol. 195, 2022, doi: 10.1016/j.vacuum.2021.110708.

[9] I. Safi, “Recent aspects concerning DC reactive magnetron sputtering of thin films: A review,” Surf. Coatings Technol., vol. 127, no. 2–3, 2000, doi: 10.1016/s0257-8972(00)00566-1.

[10] Q. M. Mehran, M. A. Fazal, A. R. Bushroa, and S. Rubaiee, “A Critical Review on Physical Vapor Deposition Coatings Applied on Different Engine Components,” Critical Reviews in Solid State and Materials Sciences, vol. 43, no. 2. 2018, doi: 10.1080/10408436.2017.1320648.

[11] R. D. Arnell and P. J. Kelly, “Recent advances in magnetron sputtering,” Surf. Coatings Technol., vol. 112, no. 1–3, 1999, doi: 10.1016/S0257-8972(98)00749-X.

[12] M. Audronis and V. Bellido-Gonzalez, “Hysteresis behaviour of reactive high power impulse magnetron sputtering,” Thin Solid Films, vol. 518, no. 8. 2010, doi: 10.1016/j.tsf.2009.12.011.

[13] K. Strijckmans, R. Schelfhout, and D. Depla, “Tutorial: Hysteresis during the reactive magnetron sputtering process,” J. Appl. Phys., vol. 124, no. 24, 2018, doi: 10.1063/1.5042084.

[14] J. Musil, P. Baroch, J. Vlček, K. H. Nam, and J. G. Han, “Reactive magnetron sputtering of thin films: Present status and trends,” in Thin Solid Films, 2005, vol. 475, no. 1-2 SPEC. ISS., doi: 10.1016/j.tsf.2004.07.041.

[15] L. C. Fontana and J. L. R. Muzart, “Triode magnetron sputtering TiN film deposition,” Surf. Coatings Technol., vol. 114, no. 1, 1999, doi: 10.1016/S0257-8972(99)00032-8.

[16] S. Kadlec, J. Musil, and H. Vyskocil, “Hysteresis effect in reactive sputtering: A problem of system stability,” J. Phys. D. Appl. Phys., vol. 19, no. 9, 1986, doi: 10.1088/0022-3727/19/9/004.

[17] P. J. Kelly and R. D. Arnell, “Magnetron sputtering: A review of recent developments and applications,” Vacuum, vol. 56, no. 3. 2000, doi: 10.1016/S0042-207X(99)00189-X.

[18] “Magnetron sputtering & magnetron sputtering deposition | FHR Thin film technology.” https://www.fhr.biz/en/thin-film-technology/sputtering-technology/magnetron-sputtering/ (accessed Aug. 19, 2022).

[19] S. Lobe et al., “Radio frequency magnetron sputtering of Li7La3Zr2O12 thin films for solid-state batteries,” J. Power Sources, vol. 307, 2016, doi: 10.1016/j.jpowsour.2015.12.054.

[20] B. Window and N. Savvides, “Unbalanced dc magnetrons as sources of high ion fluxes,” J. Vac. Sci. Technol. A Vacuum, Surfaces, Film., vol. 4, no. 3, 1986, doi: 10.1116/1.573904.

[21] R. P. Howson, H. A. J’Afer, and A. G. Spencer, “Substrate effects from an unbalanced magnetron,” Thin Solid Films, vol. 193–194, no. PART 1, 1990, doi: 10.1016/S0040-6090(05)80020-3.

[22] P. J. Kelly and R. D. Arnell, “The influence of magnetron configuration on ion current density and deposition rate in a dual unbalanced magnetron sputtering system,” Surf. Coatings Technol., vol. 108–109, 1998, doi: 10.1016/S0257-8972(98)00566-0.

# Chapter 4 - Characterization techniques

# 1. Introduction:

The developed surfaces were carefully investigated and analysed using various characterisation techniques. Importantly, the coatings were deposited on different substrate materials such as Ti-6Al-4V, Si and glass, thus ensuring that the properties of the coating would not be affected by the nature of the substrates themselves.

The characterisation of the surfaces produced was carried out at the School of Science of the University of Minho, using various techniques such as Energy Dispersive Spectrometry (EDS), Scanning Electron Microscopy (SEM), X-ray Diffraction (XRD), water contact angle (WCA) and Atomic Force Microscopy (AFM). At the same time, the evaluation of the functional response of the deposited coatings was performed at the Biological Engineering department of the University of Minho, in Braga and at the NOVA School of Science and Technology, in Lisbon. The objectives of these tests are the determination of the possible response of the organism to the implant with the coatings produced; and the determination of the antibacterial activity, essential for the objective proposed in the development of the multifunctionality of the implants. For that, Inductively Coupled Plasma Optical Emission spectroscopy (ICP-OES), antibacterial, cell viability, adhesion, proliferation, and alkaline phosphatase (ALP) assays were performed. In this chapter, is given a brief description of the different methods and techniques used for the characterisation of the coatings.

# 2. Physical and chemical characterization techniques:

Physical and chemical characterization techniques were used in order to evaluate the morphology, topography, chemical composition, crystal structure, contact angle and surface energy of the produced coatings.

## 2.1. Scanning electron microscopy and energy dispersive spectroscopy (SEM-EDS):

SEM provides information about the microstructure of a surface, homogeneity and morphology of the particles presented in the coating [1]. SEM micrographs formation depends on the acquisition of signals produced from the incidence of a focused electron beam on the sample surface, which can cause numerous types of interactions, such as inelastic interactions with the atomic electrons and elastic interactions with the atomic nucleus [2], as it can be seen in figure 7.

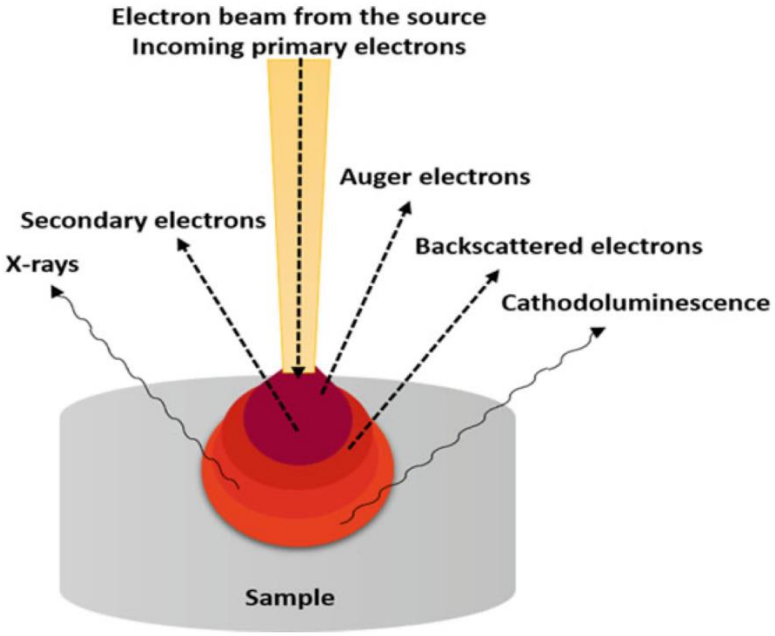


*Figure - The interaction of electron beam with specimen and the signal emitted from the sample [7].*

This technique is one of the most widely used to study surface morphology that can withstand vacuum exposure, allowing the identification of small areas that cannot be observed by optical microscopy, such as clusters. One of the requirements of SEM analysis is that the surface must be conductive. Therefore, if the surface is not conductive, it is firstly sprayed with a thin layer of a metal, making it conductive [3]. When this requirement is met, an electron beam is generated and focused on the sample by a series of electromagnetic lenses. The electron beam striking the sample surface emits X-ray and three types of electrons: backscattered electrons, secondary electrons and Auger electrons [4]. Due to their low energy, secondary electrons can only escape a few nanometres from the material surface thus providing information on the topography of the sample with good resolution. Furthermore, the elastic collisions between the electron beam and the atomic nucleus contribute to an energy conservation that leads to the emission of backscattered electrons, whose emission is strongly influenced by the atomic number of the sample [5]. Thus, in this technique, only the backscattered electrons (BSE) and the secondary electrons (SE) are collected by an appropriate detector and used to generate an image of the sample allowing to assess texture, grain defects, morphology and deformations. [6].

EDS is a standard characterisation technique to identify and quantify elemental compositions of a sample. The emission of X-rays characteristic of the atomic structure

of the elements presents in the sample due to the incidence of a focused electron beam allows the quantification of the X-ray energy by the energy dispersive detector. While the excitation of an atom occurs, an electron from its inner layer can be ejected and subsequently an electron hole is created. Subsequently, an electron from the valence layer occupies the hole, and the energy disparity between the valence and inner layer electrons is released in the form of X-rays, as shown in figure 8 [8].

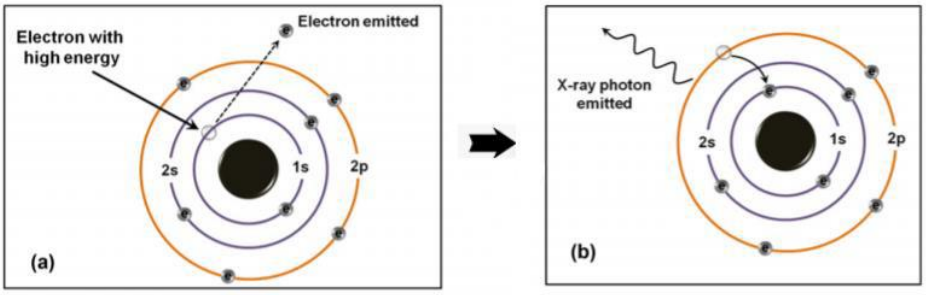


*Figure 13 - Schematic diagram illustrating the primary electron emission process. (a) High-Energy induces target atom with an inner-shell emission. (b) An electron drops from a higher energy level to the vacant hole by emitting X-rays [8].*

This emitted X-ray has an energy characteristic of the atomic structure of the element from which it was emitted. Therefore, by measuring the amount of X-ray energy emitted from the sample, it is possible to determine its composition [8]. However, X-rays with different energies may arise for the same element, depending on the atomic orbital from which they are emitted. From the difference between the background and the peak intensity emerges the energy dispersive spectrum of X-ray, as represented in figure 9. Although it is possible to identify the chemical element, EDS equipment is recommended as a qualitative method because of the possible overlap of the X-ray energy of some elements, for example Ti and N.

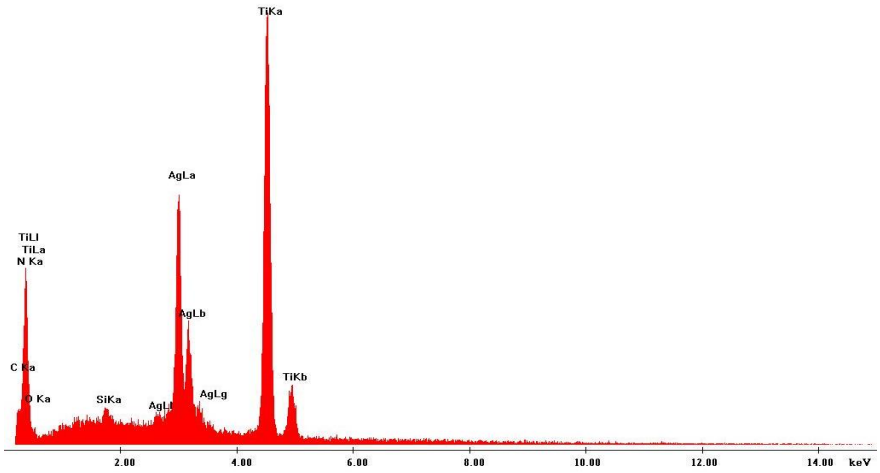


*Figure 14 - Example of an EDS spectrum for a TiN-Ag 0.21A sample.*

For this work, was used the equipment located at SEMAT laboratory in University of Minho. Chemical composition estimation was performed with an EDAX-Pegasus X4M-Energy dispersive spectrometer (EDS) apparatus coupled with a SEM. The surface morphology and thickness was examined by SEM through a NanoSEM–FEI Nova 200, FEI Company, Hillsboro, OR 97124-5793 USA (FEG/SEM) equipped with a field emission gun (FEG), operated in high vacuum mode with a chamber pressure of 0.003 Pa. The micrographs were obtained with secondary (SE) electron detectors in "through-the-lens" (TLD) mode at an acceleration voltage of 10 kV and working distance of roughly 5 mm.

## 2.2 Atomic force microscopy (AFM):

Atomic force microscopy (AFM) is a characterization technique used to assess the surface topography of a material. It uses a microfabricated piezoelectric cantilever to measure the interatomic forces between the surface atoms and the tip of the cantilever. Depending on the magnitude of the tunneling current or the deflection of the cantiliver, a magnitude that depends on the distance between the surface and the tip, it is possible to measure the height of the surface with atomic resolution in all three directions, and then map the topography of the surface. This technique, despite being relatively recent, has become an essential mechanism for analysing a surface at the nanoscale as it is able to produce detailed three-dimensional maps instead of two-dimensional images [8].

In AFM images, the sample is scanned line-by-line using a fine probe tip mounted on a micro-cantilever, thus generating a topographic image of the surface. The interaction between the tip and the surface causes the cantilever to be deflected. This deflection is monitored by a laser that is focused on the top of the cantilever and from there is reflected

onto a split photodiode. When the laser spot moves over the photodiode, it triggers a change in the electrical signal which is used in a feedback loop in order to keep the force exerted constant. During the feedback loop, voltage is applied to a piezoelectric scanner which moves the tip or show up and down. This vertical movement of the piezoelectric enables an image of the surface topography to be generated [9]. figure 10 illustrates the principal mechanism of an AFM equipment.

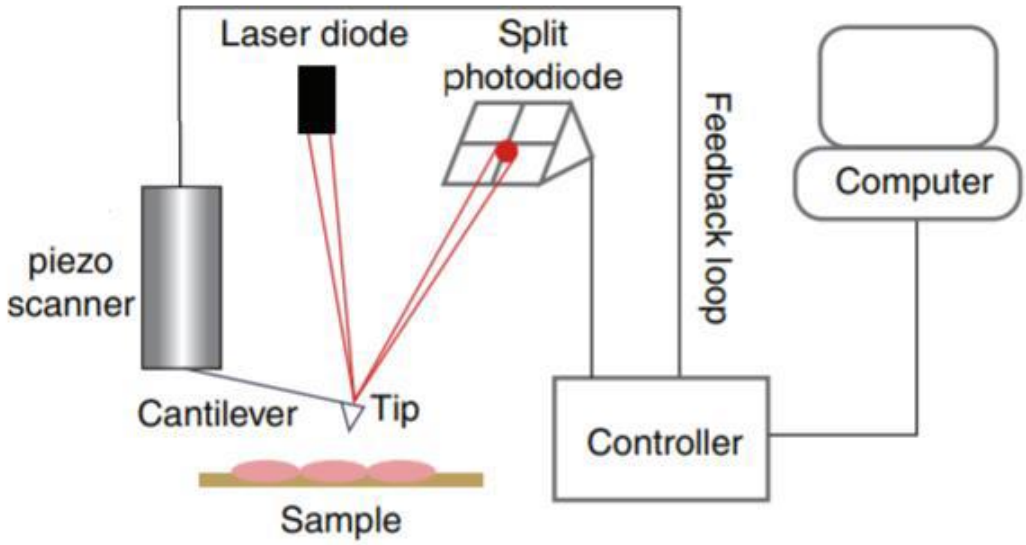


*Figure 15 - Sketch illustrating the principal of Atomic Force Microscopy [9].*

There are three AFM operation modes: contact mode, non-contact mode, and trapping mode [8]. In trapping mode, a vibrating micro-cantilever is held at a tip distance to the sample. During the vibrational motion, the lowest point of the cantilever touches the surface. While the cantilever is vibrating, the sample is dragged under the tip, which leads to changes in the vibrational parameters of the cantilever. These changes are monitored, and correctional feedback parameters are used to keep the vibration constant and then processed to produce a topographic image [10].

The AFM analysis were performed at 3B's Research Group (Biomaterials, Biodegradables and Biomimetics), in trapping mode using the Dimension icon the bruker, with an RTESPA-150 tip. All samples passed through the first order flat process. The average roughness was obtained in an area of 5x5 $\mu m^2$.

## 2.2. X-Ray Diffraction (XRD):

The structural characterization of the different coatings was performed by X-ray diffraction microscopy. XRD is a technique widely used in industry to quickly assess the crystalline structure of materials since samples require minimal preparation and the interpretation of the resulting data is usually straightforward. This technique allows the precise study of the crystalline phase structure. It is based on the constructive interference of monochromatic X-rays that occurs in a crystalline sample where the radiation is suffering a constructive interference. On the other hand, when the atoms are randomly arranged, the intensity of the radiation is annulled, suffering a destructive interference. Thus, crystalline substances containing a network of atoms can diffract the incident X-ray and generate an interference pattern. From this pattern, information about the atomic or molecular structure of the material can be obtained and, the identity of the phase [11].

The geometrical interpretation of the XRD phenomenon was described by W.L Bragg. Figure 11 shows a schematic of the interaction of X-ray with the material and gives the details about the geometrical condition of diffraction and the determination of Bragg's law, equation 1:

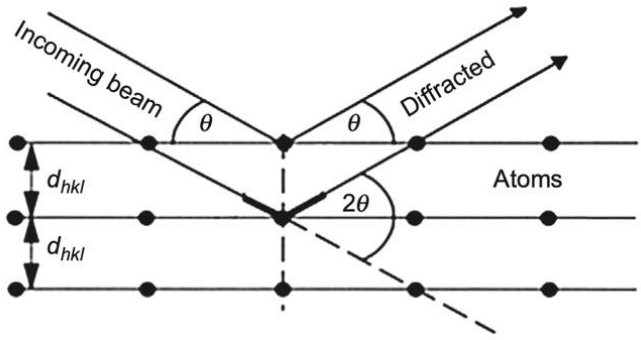


*Figure 16 - Geometrical condition for diffraction from lattice planes [12].*

Using Bragg's law:

$$n\lambda = 2d_{hkl}\, sin\, \theta \qquad \text{(Equation 1)}$$

It is possible to find a relationship between the wavelengths of the characteristic spectra and the interatomic spacing, where: $n$ is the order of diffraction, λ the wavelength of the incident beam, $d_{hkl}$ the interplanar distance, and θ the diffraction angle [12]. By measuring the angles of the X-ray when they reflect on the sample and the interplanar

spaces and comparing these data with the standard line patterns in the power diffraction file database, each crystallographic phase can be determined. It is important to mention that this file is updated annually by the International Centre for Diffraction Data (ICDD) [13]-

In this work, the XRD analyses of the films were performed at SEMAT laboratory located at University of Minho. The structure of the samples was studied by X-ray diffraction using a Bruker D8 Discover, operating at 40 Kv and 40 mA with a Cu (λk_α1= 0,1540600 nm e λk_α2 = 0,1544339 nm) equipped with a collimator. The X-ray diffraction was performed in the shallow mode at 2º with a step size of 1 second and angle 2 ranging from 200 to 800.

### 2.3. Wettability and Surface energy:

Contact angle measurements allow a better understanding of the adsorption behaviour of biomolecules. The surface wettability of a biomaterial in combination with other surface characteristics, such as nanotopography, surface energy, among others, that determines the biological cascade of events at the biomaterial/host interface ranging from protein adsorption to bacterial film formation [14].

Using the geometric mean method, Owens, Wendt & Kälble extended Fowkes concept of surface tension components (γ) by discerning polar and apolar forces. Polar interactions comprise the interactions between two permanent dipoles (Keesom interaction) and the interactions between a permanent and an induced dipole (Debye interactions). The interactions between two induced dipoles (London interactions) are considered apolar [15]. From the additivity of polar and apolar contributions postulated by Fowkes, equation 2 (a) and (b):

$$(a)\ \gamma_{lv} = \gamma_{lv}^{d} + \gamma_{lv}^{p} \qquad (b)\ \gamma_{sv} = \gamma_{sv}^{d} + \gamma_{sv}^{p} \qquad \text{(Equation 2)}$$

The interfacial tension γsl can be calculated by the equation 3:

$$\gamma_{sl} = \gamma_{v} + \gamma_{lv} - 2\left(\sqrt{\gamma_{sv}^{d} \cdot \gamma_{lv}^{d}} + \sqrt{\gamma_{sv}^{p} \cdot \gamma_{lv}^{p}}\right) \qquad \text{(Equation 3)}$$

The exponents *p* and *d* denote the polar and dispersive components while *s*, *l* and *v* represent the solid, liquid and vapour phases, respectively. Applying equation 3 to Young's equation gives the linear expression, equation 4:

$$\frac{1+\cos(\Theta)}{2}\frac{\gamma_{lv}}{\sqrt{\gamma_{lv}^{d}}} = \sqrt{\gamma_{sv}^{p}}\sqrt{\frac{\gamma_{lv}^{p}}{\gamma_{lv}^{d}}} + \sqrt{\gamma_{sv}^{d}} \qquad \text{(Equation 4):}$$

Where Θ is the contact angle of the liquid on the solid surface and $\gamma_{lv}^{p}$, $\gamma_{lv}^{d}$, $\gamma_{lv}$ are the surface tension parameters of the liquid. Consequently, the components $\gamma_{sv}^{p}$, $\gamma_{sv}^{d}$, can be determined from the slope and intercept of the linear fit to the data.

The wettability of the different samples was determined using a contact angle meter apparatus (OCA 15 Plus, DataPhysics Instruments GmbH Filderstadt, Germany). All measurements were performed at room temperature and two microliters drops of pure water (polar liquid); glycerol (polar liquid, Sigma, Merck KGaA, Darmstadt, Germany) and 1-bromonaphthalene (apolar liquid, Sigma, Merck KGaA, Darmstadt, Germany), were used as reference liquids. Using the Owens, Wendt, Rabel, and Kälble (OWRK) method [15], the surface free energy was calculated.

### 2.4. Inductively Coupled Plasma Optical Emission Spectrometry (ICP-OES):

The silver and zinc nanoparticles present in the coatings are responsible for the antibacterial activity of the coatings through ion release. One way to confirm this property is by studying their ion release kinetics. An inductively coupled plasma optical emission spectrometer (ICPOES-ICP PerkinElmer Optima 8000 spectrometer) was used to measure the release of silver and zinc ions when the coatings are in a liquid medium, in this case, in artificial saliva (since they are coatings for dental implants).

This technique begins by introducing a liquid sample into a nebuliser, which transforms it into droplets. These droplets are then sprayed into a plasma torch, where the plasma excites the electrons in the samples. As with other techniques, when the electrons return to the fundamental state, they emit electrons with wavelengths specific to the characteristic element. The intensity of this emission is proportional to the amount of the element present in the sample. Figure 12 shows a typical scheme of the ICP-OES system.

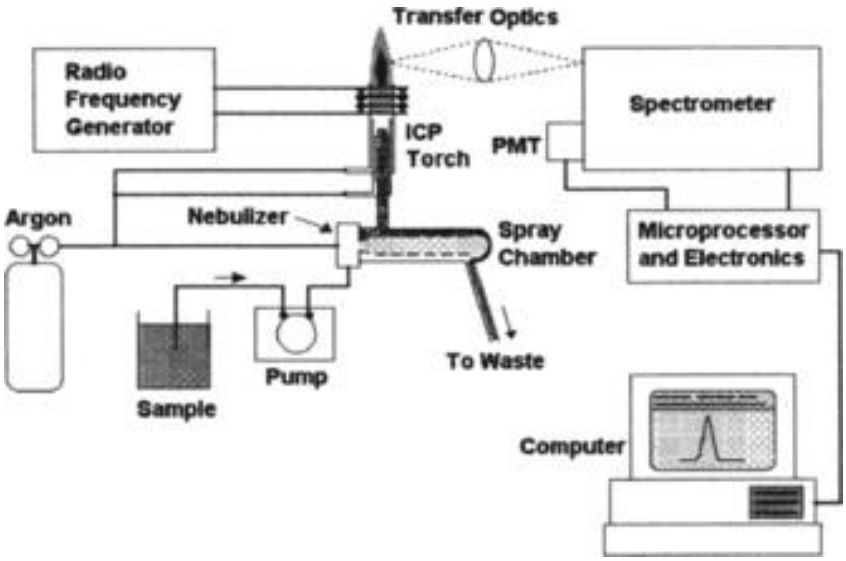


*Figure 17 - Schematic of a typical inductively coupled plasma-optical emission spectrometry (ICP-OES) system [16].*

In this work, the uncoated substrates were used as control while, the Ti-6Al-4V coated samples were used to analyse the release of $Ag^+$ and $Zn^+$ ions and compared with the control samples.

Different coatings of each condition were placed in a falcon with 50ml of artificial saliva solution. Subsequently, 2ml of this solution was removed to a new falcon at different time-setting points of immersion time in the artificial saliva solution: 2h, 6h, 12h, 48h, 120h and 168h. Before analysis, the 2ml of the solution were diluted in 4ml of nitric acid ($HNO_3$). Finally, ICP-OES was performed, and the concentration of ions released over time was calculated. The artificial saliva solution used in the test was prepared in the laboratory according to table 3.

*Table 4 - Chemical composts used to make 400 ml of artificial saliva.*

| **Artificial saliva solution** | |
|---|---|
| **Chemical compounds** | **Quantity measure** |
| NaCl | 0,1458 g |
| $CaCl_2$ | 0,1080 g |
| KCl | 0,08 g |
| $H_2O$ ultrapure | 400 ml |

To quantify the release of silver and zinc ions in an aqueous medium, a calibration curve was calculated using a silver standard solution and a zinc standard solution (specpure, 1000 ug/ml). These calibration curves are shown in figure 13.

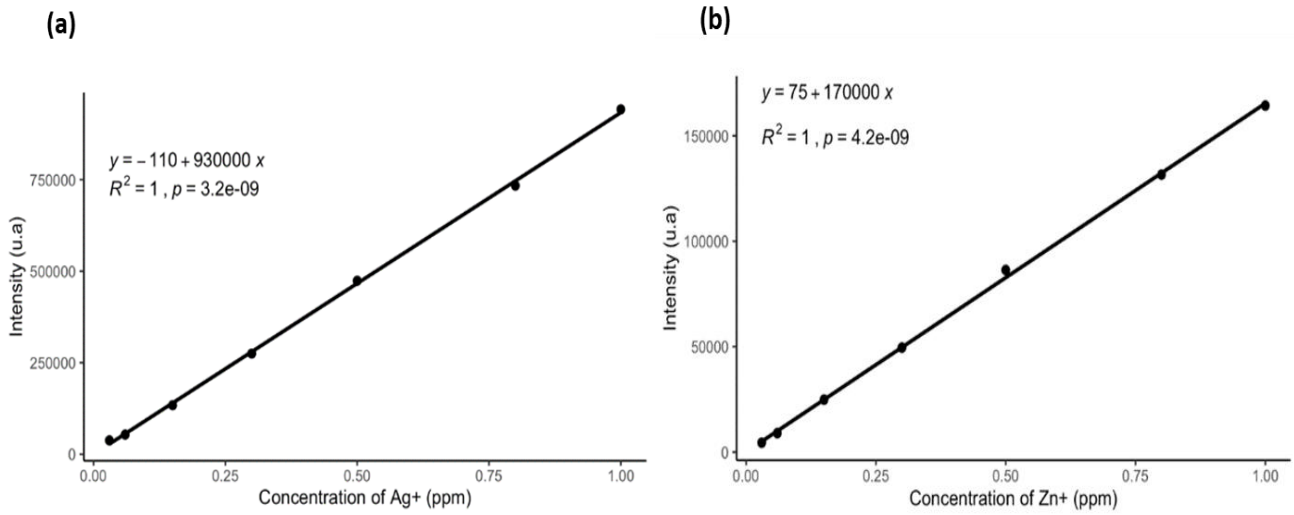


*Figure 18 - ICP-OES Silver calibration: (a) silver calibration curve with nitric acid; (b) zinc calibration curve with nitric acid.*

## 3. Biological analyses:

The biological response of the coatings produced were assessed by tests of cell viability, antibacterial activity, cells adhesion, cells proliferation, and ALP activity.

### 3.1. Cell viability:

Cell viability was assessed using the resazurin assay, which is based on the ability of metabolically active cells to reduce resazurin to resorufin, figure 14. Resazurin is a cell-permeable redox indicator that can be used to monitor the number of viable cells. This non-fluorescent blue dye is converted to pink-fluorescent resorufin in the presence of metabolically active cells. NADPH dehydrogenase is probably responsible for the electron transfer from NADPH to resazurin, which is reduced to resorufin. This conversion can be detected by visual observation of its pink colour or absorbance readings of the resorufin/resazurin ratio at 570/600. [16].

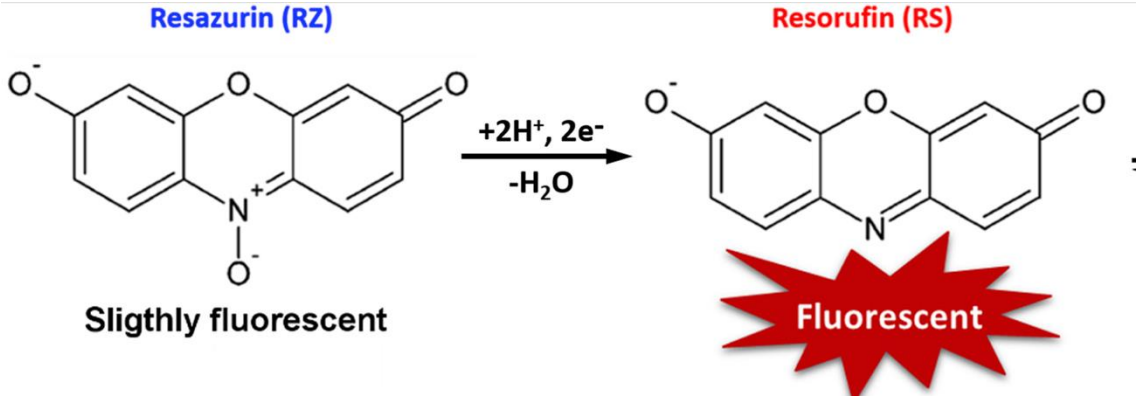


*Figure 19 - Structures and reaction mechanism of resazurin (RZ), resorufin (RS) [18].*

The methodology consisted in exposing human osteosarcoma cells (SaOS-2) to McCoy culture medium that were previously in contact with the different coatings. For this, the coatings were first sterilized in the autoclave at 180ºC, during 1h. Then, were immersed for 48h at 37ºC in a McCoy culture medium with a concentration of 100 mg/ml. At the same time, SaOS-2 cells were "seeded" in a Mccoy culture medium, in a 96-well-plate at a concentration of 30000 cells/cm$^2$, figure 15.

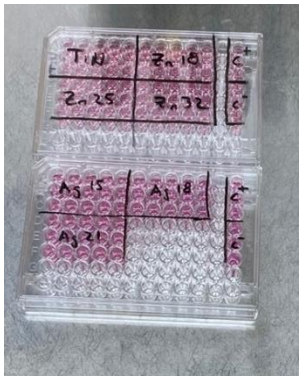

*Figure 20 - 96-well plate, "seeded" with SaOS-2 cells at a concentration of 30000 cells/cm$^2$.*

After 24h from "seeding", the extracts (McCoy medium where samples were submerged), were added to SaOS-2 cells culture for 24h. Three replicates were made with five dilutions of the extracts ($10^0$, $10^{-2}$, $10^{-4}$, $10^{-6}$, $10^{-8}$) for each sample, three negative controls using DMSO, and three positive controls using SaOS-2 cells. Finally, the resazurin was added, and after waiting for 3h, the absorbance at 570 and 600 nm was read using a Biotek ELX 800 UV reader.

The percentage of viability was calculated using equation 5:

$$\left[\frac{\left(\left(Abs_{570_{cell\ medium}} - Abs_{600\ cell\ medium}\right)\right) - \left(\left(Abs_{570_{resazurin\ control}} - Abs_{600\ resazurin\ control}\right)\right)}{\left(Abs_{570_{control}} - Abs_{600\ control}\right) - \left(\left(Abs_{570_{resazurin\ control}} - Abs_{600\ resazurin\ control}\right)\right)}\right] \times 100 \quad \text{(Equation 5)}$$

Where: $Abs_{570_{cell\ medium}}$ and $Abs_{600_{cell\ medium}}$ means the measured absorbance at 570 and 600 nm, respectively, of the sample (cells growth in the presence of the coatings; $Abs_{570_{control}}$ and $Abs_{600_{control}}$ means the measured absorbance at 570 and 600nm, respectively, of the control (cells growth without coatings); and $Abs_{570_{resazurin\ control}}$ and $Abs_{600\ resazurin\ control}$ means the measured absorbance at 570 and 600nm, respectively, of the resazurin control (only resazurin).

An important point of this methodology is that it is an indirect method for cytotoxicity evaluation, so it is only possible to evaluate if the leaching that may occur on the surface of the material is harmful to the cells.

### 3.2. Antibacterial Activity Assay:

To evaluate the antibacterial activity of the coatings produced, three microorganisms typically involved in the formation of bacterial biofilms in the oral cavity were used: two gram-positive bacteria's, *Streptococcus mutans* (DSM 20523) and

*Staphylococcus aureus* (ATCC 6538), involved in the first stage of biofilm formation; and a gram-negative bacteria, *Escherichia coli* (K12 DSM 498).

The experimental procedure for the antibacterial activity of the produced coatings was based on the ISO22196 standard [18]. Firstly, the substrates were sterilized in the autoclave at 180ºC during 1h. Each organism was pre-inoculated and incubated at 37°C for about 16h. *Streptococcus mutans* was incubated in a controlled atmosphere with 5% $CO_2$. Two independent trials were conducted for each condition, for each trial, three coatings from each condition were used. Each coating was placed in a well of 20-well plates and adeed 40 µL of the pre-inoculum of *Streptococcus mutans* with a concentration of 5 x $10^5$ cells/ml (see figure 16). On the top of each coating, a sterilised plastic film (PVC thin film with 13x13 $mm^2$) , was placed on top of the surface coating in order to spread the drop. In addition, 2 ml of water ultra-pure was placed in one well to keep the humidity atmosphere saturated. Finally, the plates were left to incubate for 24h at 37ºC. The plates with *E. coli* and *S. aureus* were sealed inside a bag with moist paper,in order to maintain a humid atmosphere. The plates with *S. mutans* were simply placed in a controlled atmosphere incubator with 5% $CO_2$ during 24h.

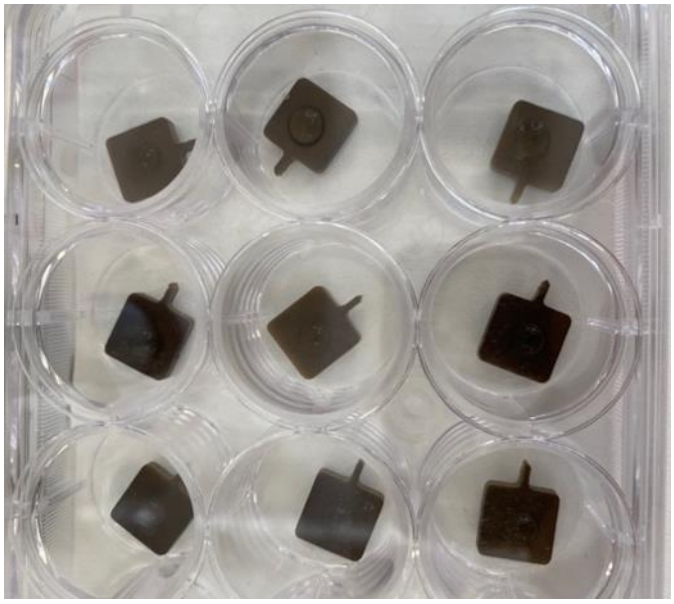

*Figure 21 - 20-well plate, with the coatings produced. Each coating contains a drop of 40 µL of the pre-inoculum at a concentration of 5 x 105 cells/ml.*

After removing the well-plates from the incubator, 1ml of SP1X salts was placed in each well and the well-plates were placed in agitation for 10 min at 220 rpm to wash the samples. Finally, a 10 µL drop of serial dilutions was placed in a Petri dish with

trypticase soy agar (TSA),. then were incubates for 24h at 37ºC. *S. mutans* was incubated with 5% $CO_2$.After, the Petri dishes were removed from the incubator and the number of Colony forming units (CFU), for each dilution was counted, figure 17.

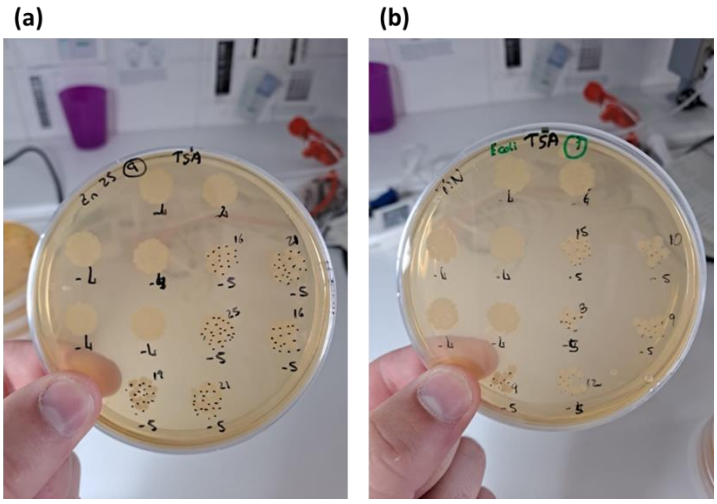


*Figure 22 - Petri dishes were removed from the incubator and the number of colony forming units (CFU), for each dilution: (a) TiN-Zn 0.25 coating; (b) TiN coating.*

### 3.3. Cell's Adhesion test:

To analyse the initial adhesion of cells to the implant, the coating samples were first sterilised in the autoclave at 180°C during 1h. Then "seeding" was performed with SaOS-2 in a 12-well plate, placing 80µL of the cell's suspension on each sample and using a density of 40000 cells/$cm^2$. Then, with the 12 well-plates the seeded samples were incubates in a controlled atmosphere of 37°C and with 4% $CO_2$ for 90 min. After, McCoy culture medium was added to each well in order to assure a volume of 2 ml. After 24h of incubation, samples were changed to a new well-plates and 2 ml of McCoy culture medium with resazurin (ratio 1:1) was placed in each well and incubated for 3h at 37°C and a 5% $CO_2$ atmosphere. After incubation time, 200uL of the McCoy medium with resazurin in contact with each coating,was removed for a new 96-well plate, obtaining two replicates per coating condition. Finally, the absorbance was measured at 570 and 600 nm.

The medium that remained in the plates with the samples was refreshed with 2 ml of McCoy culture medium and incubated during 24h at 37ºC and an atmosphere with 5% $CO_2$, in order to be used in the remaining biological assays.

### 3.4. Cell's Proliferation assay:

To evaluate the proliferation of SaOS-2 cells adhered to the different coatings, the medium of the samples was first replaced by McCoy medium with resazurin (ratio 1:1) and the well-plates were incubated at 37ºC, in an atmosphere of 5% $CO_2$ for 3h. Then 200 µL of the medium was removed from each well and putted in each well of a 96-wells-plate, in order to obtaining two replicates per each different coating. Then, the absorbance was measured at 570 and 600 nm. The medium remaining on the plates with the samples was replaced by 2 ml of McCoy's culture medium every 24h and the plates were placed in the incubator at 37ºC and in an atmosphere with 5% $CO_2$ in order to be used in the remaining biological assays.

This procedure was repeated for 4, 7, 11 and 14 days after the start of culture.

### 3.5. Cell's Differentiation assay:

Alkaline phosphatase (ALP), a glycoprotein belonging to a family of proteins anchored to the plasma membrane e through glycosylphosphatidylinositol binding, catalyses the hydrolysis of phosphate esters at alkaline pH. ALP is a common biochemical marker used to assess osteoblast differentiation and is thought to be involved in skeletal mineralisation. ALP is abundant in vesicles matrix that play a role in extracellular matrix processing and calcification of bone. ALP levels are increased immediately before mineralisation begins. Furthermore, the precise role of ALP in mineralisation remains unclear. It may be related to its calcium-binding action, generation of free phosphate, or degradation of mineralization inhibitors [19].

In this research work, to measure the ALP activity of SaOS-2 cells. First 100 µL of McCoy medium was added to each well of a a 96-well plate, in order to obtaining two replicates per each analysed condition coating. Then, the absorbance of the McCoy medium, present in the 96-well plates, was measured at 405 nm. After the measurement, 100 µL of a solution of nitrophenyl phosphate (p-NPP) in TRIS-HCL (1mg/ml), a widely used substrate for detecting alkaline phosphatase activity, was added to each well of the 96-well plate and the plates were incubated at 37ºC with an atmosphere of 5% $CO_2$, during 20 and 30 min. After that time, a new measurement of the absorbances at 405 nm was made. This procedure was repeated 5, 8, 12 and 15 days after culture initiation.

## 3.6. Statistical analysis:

The data collected during this work were analysed using R software and GraphPad Prism.

Results are presented as mean ± standard deviation (SD). Cell viability, antibacterial activity and cell adhesion were analysed using student t test. Proliferation and alkaline phosphatase activity, on the other hand, was analysed by a two-way ANOVA using Dunnett's multiple comparisons test. All experiments were performed at least in triplicate.

## 4. References:


[1] M. Faraldos and A. Bahamonde, "Multifunctional photocatalytic coatings for construction materials," in Nanotechnology in Eco-efficient Construction: Materials, Processes and Applications, 2018. doi: 10.1016/B978-0-08-102641-0.00023-2.

[2] W. Zhou, R. Apkarian, Z. L. Wang, and D. Joy, "Fundamentals of scanning electron microscopy (SEM)," in Scanning Microscopy for Nanotechnology: Techniques and Applications, 2007. doi: 10.1007/978-0-387-39620-0_1.

[3] S. Ebnesajjad, Surface treatment of materials for adhesive bonding. 2013. doi: 10.1016/C2013-0-12914-5.

[4] H. Zhang, "Surface Characterization Techniques for Polyurethane Biomaterials," in Advances in Polyurethane Biomaterials, 2016. doi: 10.1016/B978-0-08-100614-6.00002-0.

[5] M. Ohring, The Materials Science of Thin Films. 2013. doi: 10.1016/C2009-0-22199-4.

[6] G. Cao, NANOSTRUCTURES AND NANOMATERIALS - Synthesis, Properties and Applications. 2010. doi: 10.1142/9781860945960.

[7] K. Akhtar, S. A. Khan, S. B. Khan, and A. M. Asiri, "Scanning electron microscopy: Principle and applications in nanomaterials characterization," in Handbook of Materials Characterization, 2018. doi: 10.1007/978-3-319-92955-2_4.

[8] H. Wang and P. K. Chu, "Surface Characterization of Biomaterials," in Characterization of Biomaterials, 2013. doi: 10.1016/B978-0-12-415800-9.00004-8.

[9] F. J. Giessibl, "Advances in atomic force microscopy," Reviews of Modern Physics, vol. 75, no. 3. 2003. doi: 10.1103/RevModPhys.75.949.

[10] B. Voigtländer, "Scanning Probe Microscopy: Atomic Force Microscopy and Scanning Tunneling Microscopy," NanoScience and Technology, 2015.

[11] D. Alderton, "X-Ray Diffraction (XRD)," in Encyclopedia of Geology, 2021. doi: 10.1016/b978-0-08-102908-4.00178-8.

[12] J. Epp, "X-Ray Diffraction (XRD) Techniques for Materials Characterization," in Materials Characterization Using Nondestructive Evaluation (NDE) Methods, 2016. doi: 10.1016/B978-0-08-100040-3.00004-3.

[13] F. Rupp et al., “A review on the wettability of dental implant surfaces I: Theoretical and experimental aspects,” Acta Biomaterialia, vol. 10, no. 7. 2014. doi: 10.1016/j.actbio.2014.02.040.

[14] M. Rankl, S. Laib, and S. Seeger, “Surface tension properties of surface-coatings for application in biodiagnostics determined by contact angle measurements,” Colloids Surf B Biointerfaces, vol. 30, no. 3, 2003, doi: 10.1016/S0927-7765(03)00085-7.

[15] J. Sneddon and M. D. Vincent, “ICP-OES and ICP-MS for the determination of metals: Application to oysters,” Analytical Letters, vol. 41, no. 8. 2008. doi: 10.1080/00032710802013991.

[16] A. Mehring, N. Erdmann, J. Walther, J. Stiefelmaier, D. Strieth, and R. Ulber, “A simple and low-cost resazurin assay for vitality assessment across species,” J Biotechnol, vol. 333, 2021, doi: 10.1016/j.jbiotec.2021.04.010.

[17] D. Ibáñez, D. Izquierdo-Bote, A. Pérez-Junquera, M. B. González-García, D. Hernández-Santos, and P. Fanjul-Bolado, “Raman and fluorescence spectroelectrochemical monitoring of resazurin-resorufin fluorogenic system,” Dyes and Pigments, vol. 172, 2020, doi: 10.1016/j.dyepig.2019.107848.

[18] “ISO 22196 - Antimicrobial Plastic Test - Situ Biosciences.” https://www.situbiosciences.com/product/iso-22196-antimicrobial-plastic-test/ (accessed Oct. 13, 2022).

[19] V. Pivodovaa, J. Frankovaa, and J. Ulrichovaa, “Osteoblast and gingival fibroblast markers in dental implant studies,” Biomedical Papers, vol. 155, no. 2, 2011, doi: 10.5507/bp.2011.021.

# Chapter 5 – Results and Discussion:

## 1. Introduction:

In this chapter, the results obtained from the physical, chemical and functional characterization of the produced coatings will be presented and discussed.

Since all the coatings were deposited with a constant power density applied to the titanium target ($J_{Ti}$=10 mA/cm$^2$), varying only the power density applied to the silver target ($J_{Ag}$ of 0.75, 0.90 and 1.05 mA/cm$^2$, respectively) in the TiN-Ag coatings, and the power density applied to the zinc target ($J_{Zn}$ of 0, 90, 1.25 and 1.60 mA/cm$^2$, respectively) in TiN-Zn coatings, keeping constant the $N_2$ flow rate, of 6.25 sccm, the chemical, physical and biological properties of the films, directly result from a higher or lower incorporation of Ag and Zn particles in TiN-Ag and TiN-Zn coatings.

## 2. Physical and chemical characterization:

The deposition conditions, together with the chemical composition, thickness, deposition rate and roughness are summarized in table 5.

*Table 5 - Results obtained for chemical composition, thickness, deposition rate and roughness, as well as some experimental details.*

| Coating | Current density | | Thickness (nm) | Deposition rate (nm/h) | Chemical composition (at. %) | | | | Ti/N ratio | (Ag or Zn)/Ti | Roughness (nm) |
|---|---|---|---|---|---|---|---|---|---|---|---|
| | $J_{Ti}$ (dc) (mA/cm$^2$) | $J_{(Ag\ or\ Zn)}$ (puls) (mA/cm$^2$) | | | N | Ti | Ag | Zn | | | |
| TiN | 10 | 0 | 1190 | 595 | 48 | 52 | - | | 1.09 | - | 8.2 |
| TiN-Ag 0,15A | 10 | 0.75 | 1500 | 1000 | 46 | 51 | 3 | - | 1.11 | 0.05 | 22 |
| TiN-Ag 0,18A | 10 | 0.90 | 1090 | 727 | 43 | 49 | 8 | - | 1.16 | 0.16 | 32 |
| TiN-Ag 0,21A | 10 | 1.05 | 1250 | 833 | 42 | 45 | 13 | - | 1.09 | 0.28 | 47.2 |
| TiN-Zn 0,18A | 10 | 0.90 | 1650 | 1100 | 49 | 46 | - | 5 | 0.94 | 0.15 | 17.8 |
| TiN-Zn 0,25A | 10 | 1.25 | 1150 | 767 | 50 | 44 | - | 6 | 0.88 | 0.20 | 25.1 |
| TiN-Zn 0,32A | 10 | 1.60 | 2400 | 1600 | 31 | 44 | - | 25 | 1.42 | 0.71 | 186.5 |

Through the deposition time and the thickness of the coating estimated by SEM cross-section images, performed on a silicon substrate, it was possible to determine the deposition rate. Again, considering that all the coatings were deposited with a constant

power density applied to the Ti target and constant $N_2$ flow rate of 6.25 sccm, varying only the power density applied to the Ag and Zn target in TiN-Ag and TiN-Zn coatings, respectively, in order to achieve different silver and zinc contents. The samples also present a residual amount of oxygen and carbon of less than 5 at. %, and less than 8 at. %, respectively. as a result of contamination.

All coatings show a Ti/N ratio greater than 1, indicating a slight excess of Ti over $N_2$, however, it does not deviate much from the stoichiometric ratio (1:1), as verified in previous studies [1] [2]. The Ag and Zn content is influenced by the deposition conditions: the atomic percentage of Ag, Zn in the doped coatings increase with increasing current density applied to the target of the respective element, figure 24.

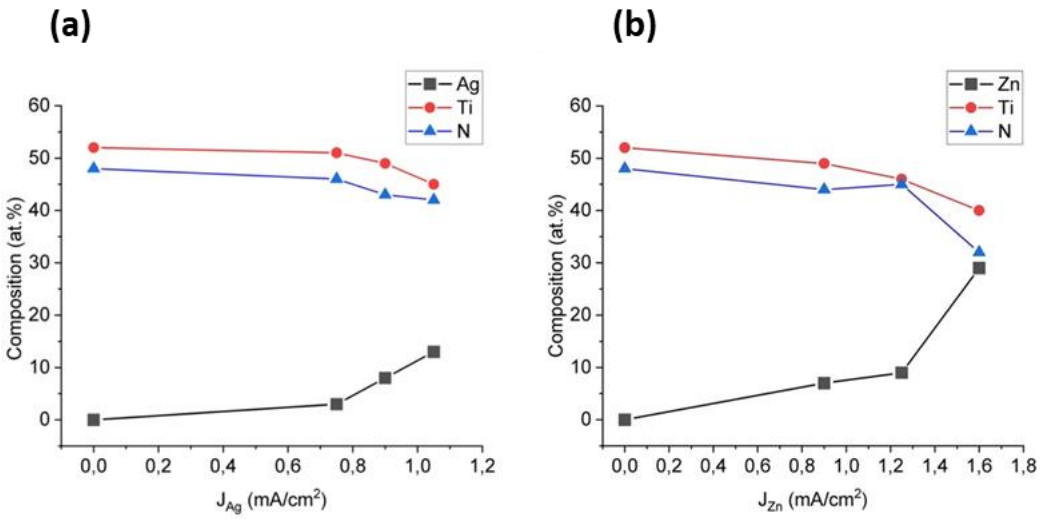


*Figure 23 - Chemical compositions of the various coatings: (a) TiN-Ag; (b) TiN-Zn.*

It was expected that the deposition rates would increase with increasing power density applied to the silver and zinc targets, since Ag and Zn present a higher sputtering yield than Ti (380 Å/sec for Ag, 80 Å/sec for Ti and 340 Å/sec for Zn when bombarded with Ar at 600 eV)[3]. However, a direct relationship between the current applied to the target and the deposition rate was not found, since in the deposition of the silver coatings, a power density was applied to the silver target in the order of 0.75, 0.90 and 1.05 mA/cm$^2$, and a deposition rate of 1000, 727 and 833 nm/h was obtained, respectively. In the case of the deposition of zinc coatings, the same phenomenon was observed, applying a power density on the zinc target in the range of 0.90, 1.25 and 1.60 mA/cm$^2$ and obtaining a deposition rate of 1100, 767 and 1600 nm/h. There are several explanations for this phenomenon: one was reported by Pah Jisheng at. al [4], where he demonstrated

that the surface topography of the targets can influence the sputtering yield; another may be errors during the execution of the SEM analysis because considering the steps followed in the deposition of the films, it was expected that the cross-section images would show several layers (figura 25). However, in the micrographs obtained from the TiN-Ag and TiN-Zn samples only the Ti interlayer is visible.

## 2.1. Morphology:

SEM top-view and cross-section, AFM and WCA analyses were performed to evaluate the surface characteristics and the presence of Ag and Zn nanoparticles on the surface of the TiN-Ag and TiN-Zn coatings, respectively, which would be available for an immediate antibacterial activity. Figure 25 shows the SEM micrographs of the TiN, TiN-Ag and TiN- Zn coatings deposited on silicon substrates.

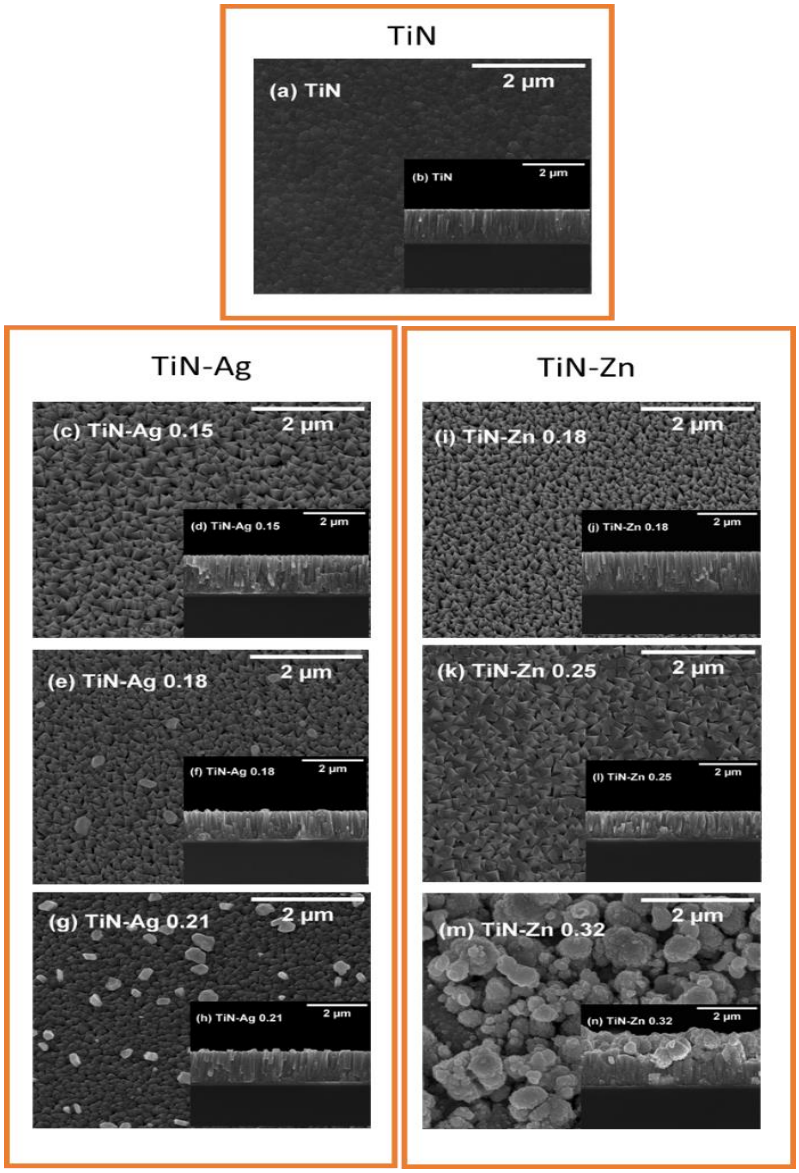


*Figure 24 - SEM micrographs in SE mode of the different films, deposited in PVD. The inserts are cross-section micrographs.*

The analysis SEM micrographs shows that the incorporation of silver and zinc in TiN coatings causes a drastic change in the morphology of the film. The TiN sample is homogeneous with a very smooth surface, while the silver doped coatings are composed of nanoparticles embedded in a TiN matrix. On the other hand, the zinc doped coatings saw their morphology changed, however no nanoparticles are visible. The TiN columns in the film matrix change from a "scale-like" surface morphology in the case of TiN, to a pyramidal structure when silver is added. These structures, as the silver content is increased, become progressively more rounded. It can also be observed that the homogeneity of the coating is affected. While the TiN sample is homogeneous, presenting a very smooth surface, increasing the silver content proves changes in this characteristic. Increasing the zinc content in the film induces also causes significant changes in the surface structure of the coating. The TiN columns in the film matrix evolved pyramidal structures. These structures assume a more rounded shape in the case of TiN-Zn 0.25, becoming fully amorphous and heterogeneous in the case of TiN-Zn 0.32.

Several authors [1] [6], reported that TiN-Ag coatings are composed of Ag clusters inserted into the column boundaries of the TiN matrix. In this sense, TiN-Ag 0.18 and TiN-Ag 0.21 samples are composed of a heterogeneous surface being possible to observe Ag clusters. The appearance of Ag cluster on the surface can be explained by its significant diffusion throughout the film thickness and by coalescence processes, properties already known of silver-based nanocomposites [7]. The existence of these clusters on the surface is a promising aspect for the objective of the work because in this way the silver is more quickly available for the desired antibacterial activity. To elucidate these conclusions the morphology of the coatings was analysed using micrographs of cross sections, showing a columnar structure common in this type of films with a relatively low deposition temperature, according to the Thornton diagram [8], and an accumulation of silver nanoparticles (white/shiny dots) in the TiN matrix. It is noticeable that as the silver content increases, the silver is no longer as visible in the TiN matrix since, it migrates to the surface, resulting in a non-uniform distribution of Ag over the thickness of the coating.

Using ImageJ software, it was possible to calculate the area of the clusters that appeared on the surface of the silver doped samples, table 6. As expected, a higher silver content led to the emergence of clusters with larger areas.

*Table 6 - Area of the nanoparticles present in each sample.*

| Particle size | |
|---|---|
| **Coating** | **Area (μm²)** |
| TiN-Ag 0.18 | 0.054 ± 0.02 |
| TiN-Ag 0.21 | 0.080 ± 0.026 |

In both cases, the film roughness increases along with the Ag and Zn content, figure 26.

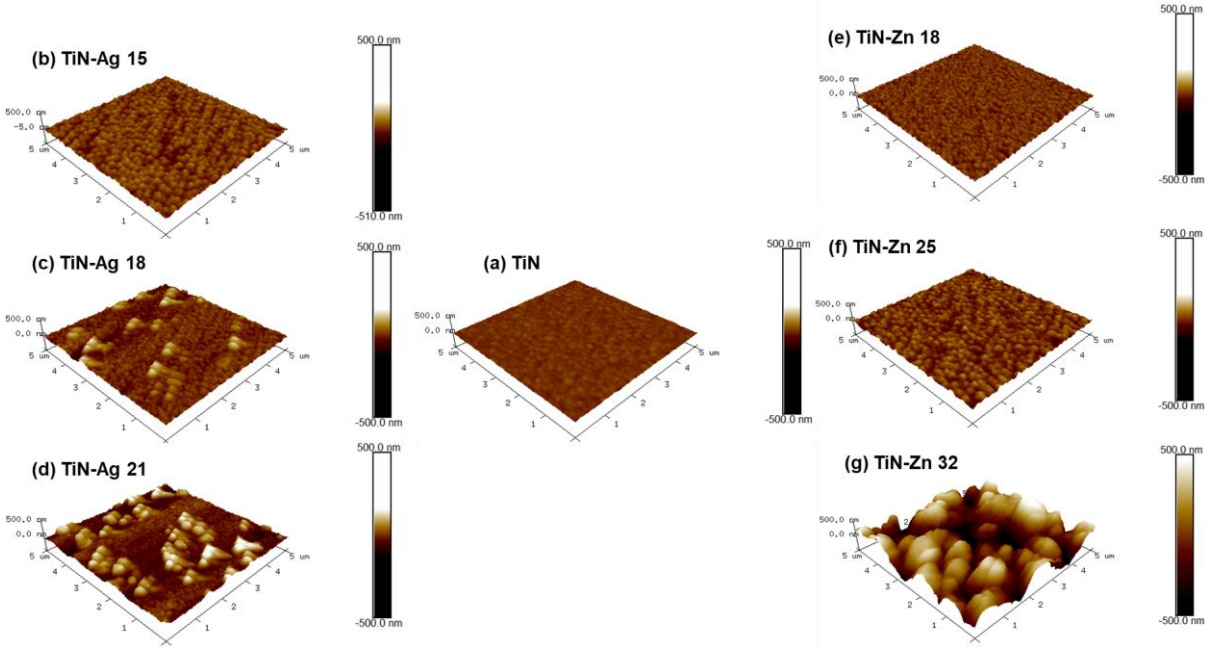


*Figure 25 - AFM images of the TiN, TiN-Ag and TiN- Zn coatings deposited on silicon substrates.*

From a mechanical point of view, the primary stability of the implant will be improved by a rough surface as it provides friction between the implant surface and the bone tissue, resulting in a greater initial retention, and consequently a greater stability, achieved soon after surgery [5]. Similarly, cell adhesion also depends on the anchorage sites on the implant surface. Thus, the roughness should be carefully controlled, since if it is much smaller than the size of the cells, there will not be adequate anchorage sites. On the other hand, roughness of large dimensions compared to the size of the cells will also not provide ideal sites for biofixation.

The surface hydrophobicity of the different samples was also evaluated by contact angle measurements, shown in Figure 27. The surface energy of the various coatings was calculated according to the Owens, Wendt, Rabel (OWRK) approach [9], which is a

standard procedure to calculate the surface energy of hydrophobic solid surfaces from the contact angle using at least two liquids, table 7.

*Table 7 - Water, glycerol and 1-bromonaphthalene contact angles and surface energy components of the different coatings.*

| Coating | Contact angle ± SDa (deg) | | | Surface energy components (mN/m) | | |
|---|---|---|---|---|---|---|
| | Water | Glycerol | 1-Bromonaphthalene | γ Polar | γ Dispersive | γ Total |
| **Ti-6Al-4V** | 73 ± 5 | 80 ± 7 | 55 ± 2 | 9.48 | 22.33 | 31.81 |
| **TiN** | 76 ± 2 | 79 ± 3 | 63 ± 3 | 9.75 | 19.91 | 29.66 |
| **TiN-Ag 0.15** | 85 ± 7 | 81 ± 6 | 41 ± 11 | 3.15 | 30.37 | 33.52 |
| **TiN-Ag 0.18** | 93 ± 14 | 77 ± 7 | 40 ± 4 | 1.27 | 33.81 | 35.09 |
| **TiN-Ag 0.21** | 106 ± 4 | 70 ± 4 | 31 ± 14 | 0.29 | 40.65 | 40.94 |
| **TiN-Zn 0.18** | 94 ± 6 | 54 ± 8 | 49 ± 6 | 1.92 | 37.00 | 39.92 |
| **TiN-Zn 0.25** | 114 ± 2 | 117 ± 2 | 43 ± 5 | 0.53 | 26.62 | 27.15 |
| **TiN-Zn 0.32** | 114 ± 1 | 107 ± 3 | 55 ± 3 | 0.13 | 24.54 | 24.66 |

The surfaces can be classified as superhydrophilic when in the case of liquid water Ø=0º, hydrophilic when Ø<90º and hydrophobic when Ø>90 [8]. Thus, the water contact angles obtained for the different coatings (figure 27 and table 7) indicate that TiN and TiN-Ag 0.15 are coatings with a hydrophilic character. On the other hand, the remaining coatings produced present a contact angle greater than 90° indicating that they are hydrophobic [10] [11]. It is notable that the doping of TiN with silver or zinc nanoparticles causes the increase of the hydrophobicity of the coating, i.e., as the silver or zinc content is increased, the water contact angle also increases. On the other hand, looking at the surface energies of the different coatings (table 7), and dividing it into its polar and dispersive components, the dispersive component presents higher values compared to the polar component. These results are in line with the hydrophobic character observed in the different coatings. Fangyuan Yan at al [41] analysed silver coated films by static contact angle and concluded that they are hydrophobic due to the chemical properties of silver, and the emergence of agglomerates increases hydrophobicity.

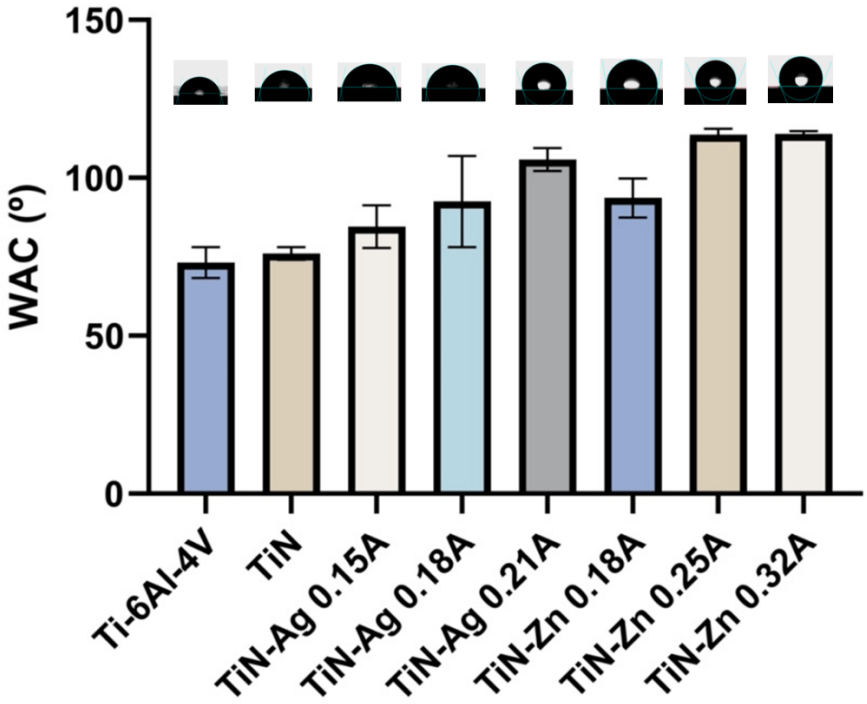


*Figure 26 - The water contact angle of the several samples. Data was represented as mean± standard deviation.*

Water molecules establish the first contact with the implant surface during implant placement. Therefore, from an osseointegration point of view, a hydrophilic surface is considered desirable to promote the initial stages of bone healing. Thus, surface wettability plays an important role in early bone healing [12]. Protein adsorption occurs on the implant surface; initially by high wettability proteins present in higher concentration in plasma, which are then replaced by other proteins with greater affinity for the implant surface (Vroman effect) [13]. This process is delayed on a hydrophobic surface, thus highlighting the importance of a hydrophilic surface in preserving the tertiary structures and activities of the proteins adsorbed on the surface. On the other hand, from the point of view of antibacterial activity, it has been shown in previous studies that there is a direct correlation between the wettability of a surface and the rate of bacterial attachment: higher surface wettability results in higher bacterial attachment and a higher rate of subsequent spreading [14].

## 2.2 Structural analysis:

The XRD results for the crystalline structures present in the samples are presented in the form of diffractogram in figure 28. Comparing the spectra of the samples with the Power Diffraction Files from ICDD it is possible to verify the presence of the crystal

structures of stoichiometric FCC-TiN (ICDD 00-038-1420), FCC-Ag (ICDD 00-004-0783) and hexagonal Zn (ICDD 00-004-083).

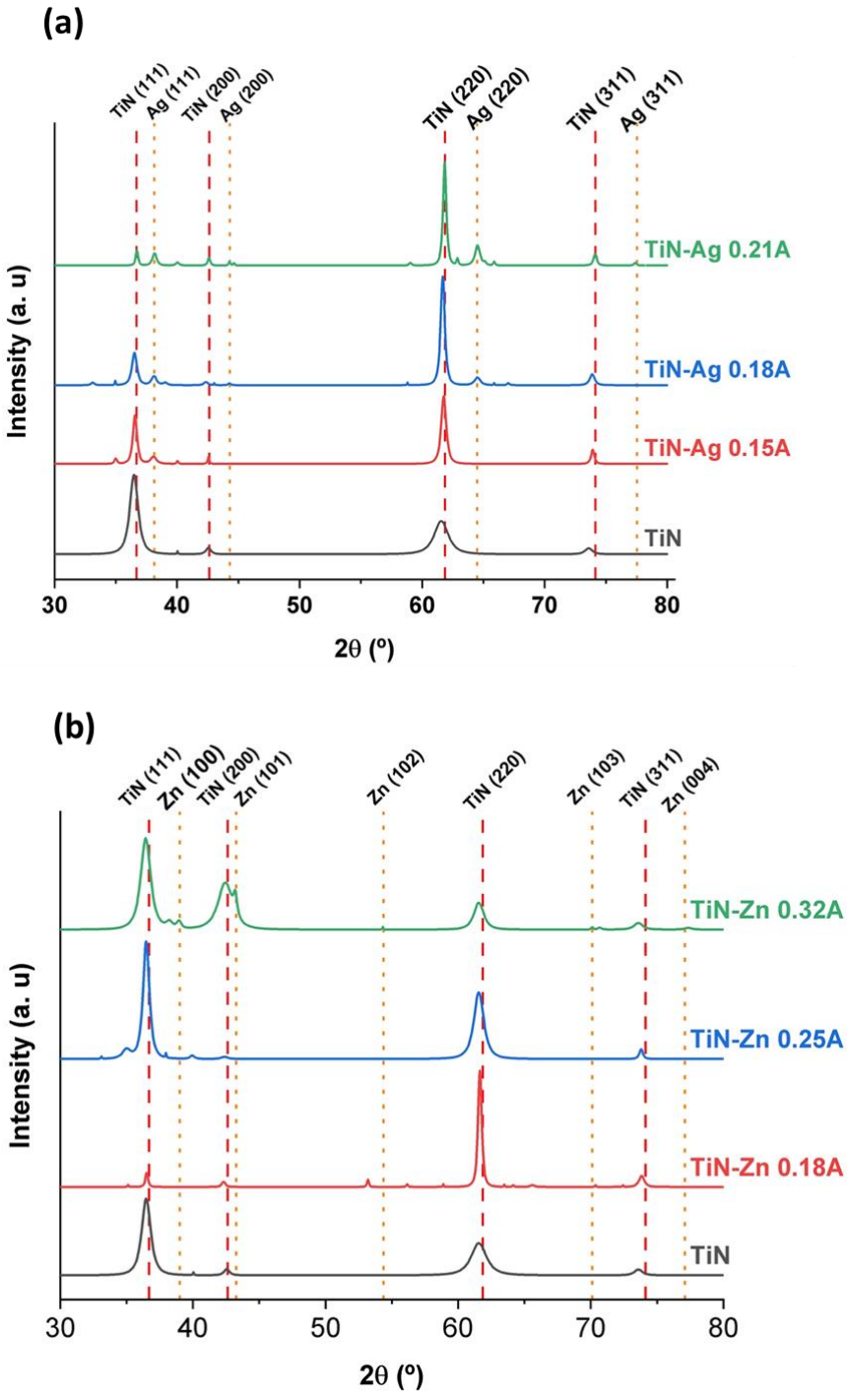


*Figure 27 - XRD diffractogram of several coatings: (a) TiN-Ag; (b) TiN-Zn*

The differences in chemical composition correlate well with the observed differences in the developed structure. The XRD pattern of the TiN coating indicates that

the most intense peaks are located at 36.8° and 62.1º, which are very close to the TiN (111) and TiN (220) peaks. Previous studies with TiN coatings deposited by magnetron sputtering have reported this behaviour [15] [16].

Regarding TiN-Ag coatings, one can clearly identify the presence of two crystalline phases, namely one of the stoichiometric TiN and one phase of Ag. The intensity of the TiN (111) peak decreases with increasing Ag content. On the other hand, the TiN (220) peak increases significantly as the silver content increases. Moreover, the FWHM of the TiN (220) peak becomes narrower and narrower indicating that the grain size increases [17]. The diffractogram analysis of TiN-Zn coatings, on the other hand, confirms the presence of stoichiometric titanium nitride in all the series. As the Zn content increases, the preferential phase of TiN changes from TiN (220) to (111). Also, only in TiN-Zn 0.32A series was it possible to verify the existence of Zn crystalline phase. Previous studies justify this observation with the possibility of Zn being in an amorphous form, or being present in a low concentration, or the nanoparticles are of a small size, which are not identified by XRD [18].

Using the Scherrer equation, equation 6, a grain size was calculated for the most intense peaks of TiN, Ag and Zn. The results are presented in the tables 8-9.

$$D_{hkl} = \frac{k\lambda}{\beta \cos \Theta`} \qquad \text{(Equation 6)}$$

*Table 8 - Grain size was calculated on TiN-Ag coatings for the most intense TiN and Ag peaks.*

| **Peak** | **$D_{hkl}$ (nm)** | | | |
|---|---|---|---|---|
| | **TiN** | **TiN-Ag 0.15** | **TiN-Ag 0.18** | **TiN-Ag 0.21** |
| **TiN (111)** | 10.5 | 20.9 | 17.4 | 34.7 |
| **TiN (220)** | 6.8 | 19.3 | 23.1 | 29.0 |
| **Ag (111)** | - | 14.3 | 16.8 | 21.0 |
| **Ag (220)** | - | - | 16.8 | 19.4 |

These results are in agreement with those obtained by S. Calderon Velasco at al [22] where he reported that the main crystalline phase for silver in TiN-Ag coatings is FCC and the grain size of Ag 6-78 nm and of TiN 12-80 nm.

In the case of TiN-Zn coatings, it can be observed that the growth of a new phase (zinc), compromises the growth of the TiN phase, table 9. Thus, the TiN grain size decreases as the zinc content increases.

*Table 9 - Grain size was calculated on TiN-Zn coatings for the most intense TiN and Zn peaks.*

| **Peak** | **$D_{hkl}$ (nm)** | | | |
|---|---|---|---|---|
| | **TiN** | **TiN-Zn 0.18** | **TiN-Zn 0.25** | **TiN-Zn 0.32** |
| **TiN (111)** | 10.5 | 34.9 | 14.9 | 9.5 |
| **TiN (220)** | 6.8 | 28.9 | 10.5 | 10.5 |
| **Zn (101)** | - | - | - | 18.3 |
| **Zn (100)** | - | - | - | 15.1 |

Finally, knowing previously through the ICDD sheets that TiN and Ag have an FCC structure and Zn a hexagonal structure, the XRD network parameters were calculated using the following equations below. The results are presented in tables 10-11.

- FCC Structure (TiN, Ag):

$$a = b = c$$

$$\frac{1}{d^2{}_{hkl}} = \frac{h^2+k^2+l^2}{a^2} \qquad \text{(Equation 7)}$$

- Hexagonal structure (Zn):

$$a = b \neq c$$

$$\frac{1}{d^2{}_{hkl}} = \frac{4}{3}\left(\frac{h^2+k+k^2}{a^2}\right) + \frac{l^2}{c^2} \qquad \text{(Equation 8)}$$

*Table 10 - XRD network parameters was calculated on TiN-Ag coatings for the most intense TiN and Ag peaks.*

| Peak | a (Å) | | | |
|---|---|---|---|---|
| | TiN | TiN-Ag 0.15 | TiN-Ag 0.18 | TiN-Ag 0.21 |
| TiN (111) | 4.27 | 4.26 | 4.25 | 4.24 |
| TiN (220) | 4.27 | 4.26 | 4.25 | 4.24 |
| Ag (111) | - | 4.09 | 4.09 | 4.08 |
| Ag (220) | - | - | 4.09 | 4.09 |

*Table 11 - XRD network parameters was calculated on TiN-Zn coatings for the most intense TiN and Zn peaks.*

| Peak | a (Å) | | | | |
|---|---|---|---|---|---|
| | TiN | TiN-Zn 0.18 | TiN-Zn 0.25 | TiN-Zn 0.32 | |
| TiN (111) | 4.27 | 4.26 | 4.26 | 4.26 | |
| TiN (220) | 4.27 | 4.26 | 4.26 | 4.26 | |
| | | | | a | b |
| Zn (101) | - | - | - | 2.67 | 4.96 |
| Zn (100) | - | - | - | 2.67 | 4.96 |

According to the ICDD sheets, TiN and Ag have an FCC structure, with a network parameter a=4.24 Å and a=4 Å, respectively. On the other hand, according to the ICDD sheets in zinc doped TiN coatings, Zn has a hexagonal structure with a network parameter a=2.66 Å and b=4.94 Å. In this work, larger values were obtained due to the compressive stresses [42].

## 2.3 Silver and zinc ion release:

The ICP-OES results for silver and zinc ion release from samples immersed in an artificial saliva solution at room temperature for 7 days are shown in figure 29-30.

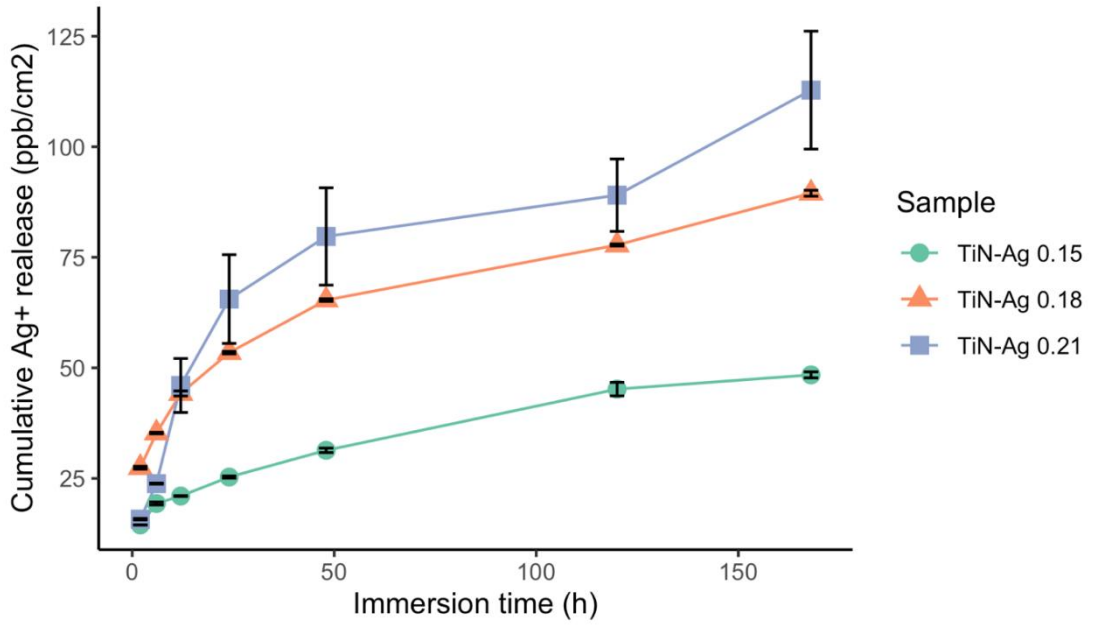


*Figure 28 - Ag+ release along time (2h, 6h, 12h, 24h, 48h, 120h and 168h) determined by ICP-OES analysis. Data was represented as mean± standard deviation.*

The silver ionization by the sample with lower silver content (TiN-Ag 0.15) over time was always lower compared to the samples with higher content, reaching a maximum of about 48 ppb/cm$^2$ after 7 days.

The samples with higher silver content (TiN-Ag 0.18 and TiN-Ag 0.21) show a different behaviour, since the sample with an intermediate silver content shows a higher silver ionisation than TiN-Ag 0.21 in the first 6h (35 and 23 ppb/cm$^2$, respectively).

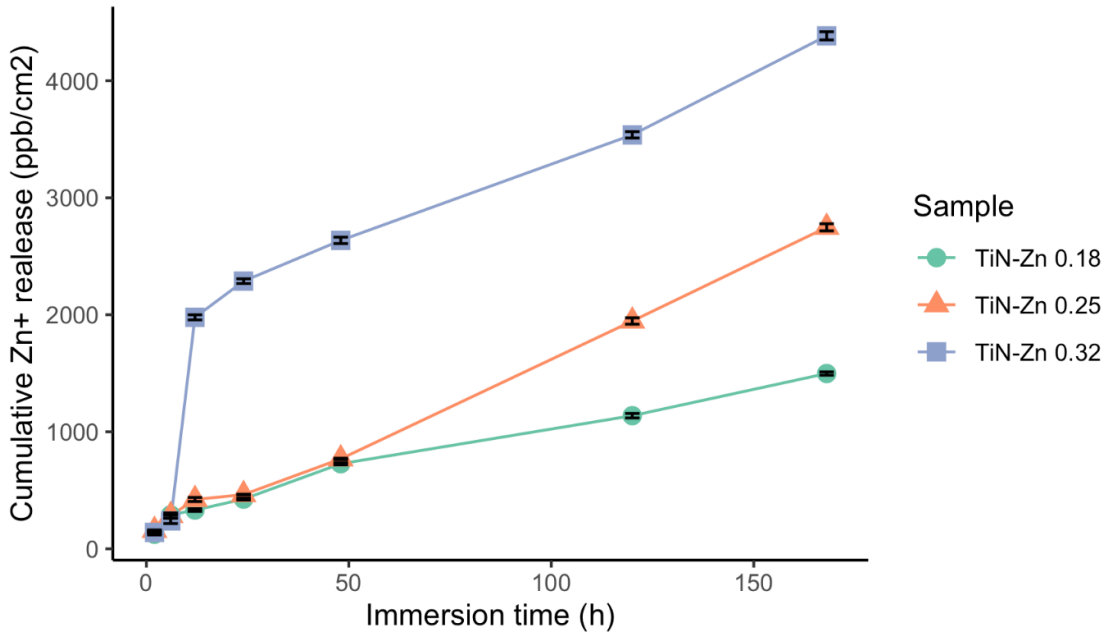


*Figure 29 - Zn+ release along time (2h, 6h, 12h, 24h, 48h, 120h and 168h) determined by ICP-OES analysis. Data was represented as mean± standard deviation.*

Regarding the release of zinc ions, it can be conclude that the ionisation of zinc by the sample with lower zinc content (TiN-Zn 0.18) over time was always lower compared to the samples with a higher content. However, it can be said that the difference in zinc ionisation only becomes significant on the second day of immersion compared to TiN-Zn 0.25. On the other hand, the TiN-Zn 0.32 sample stands out from the others since it reaches 2000 ppb/cm$^2$ in only 12h and goes up to 4300 ppb/cm$^2$ after 7 days.

This result corroborates the morphology of the samples, as mentioned previously (Section 2.1. Morphology), the TiN-Ag 0.18 and TiN-Ag 0.21 coatings present silver agglomerates on their surface (Figure 25), unlike the TiN-Ag 0.15 sample, where the silver is incorporated into the bulk coating, delaying Ag ionisation during the first days of immersion. They also meet with the EDS results (Section 2. Physical and chemical characterization:), where the silver content present in the coatings was proved to increase.

Finally, this analysis also allowed us to conclude that the samples have not yet stabilized and would continue to release ions, since no stationary phase was reached in the graphs of the different samples.

# 3. Biological analysis:

## 3.1. Cell viability:

By measuring the absorbance, it was possible to quantify (using equation 5) the amount of resazurin and resorufin since these molecules present absorbance peaks at 601nm and 571nm, respectively. Since the conversion rate is directly proportional to the number of viable cells in each well, it was possible to calculate cell viability for each sample, figure 31.

The analysis was carried out considering the percentage of viability obtained: viability above 90%, the material is not cytotoxic; cell viability between 80% and 89% is considered slightly cytotoxic; between 50% and 79% is moderately cytotoxic; if it is less than 50% it is severely cytotoxic.

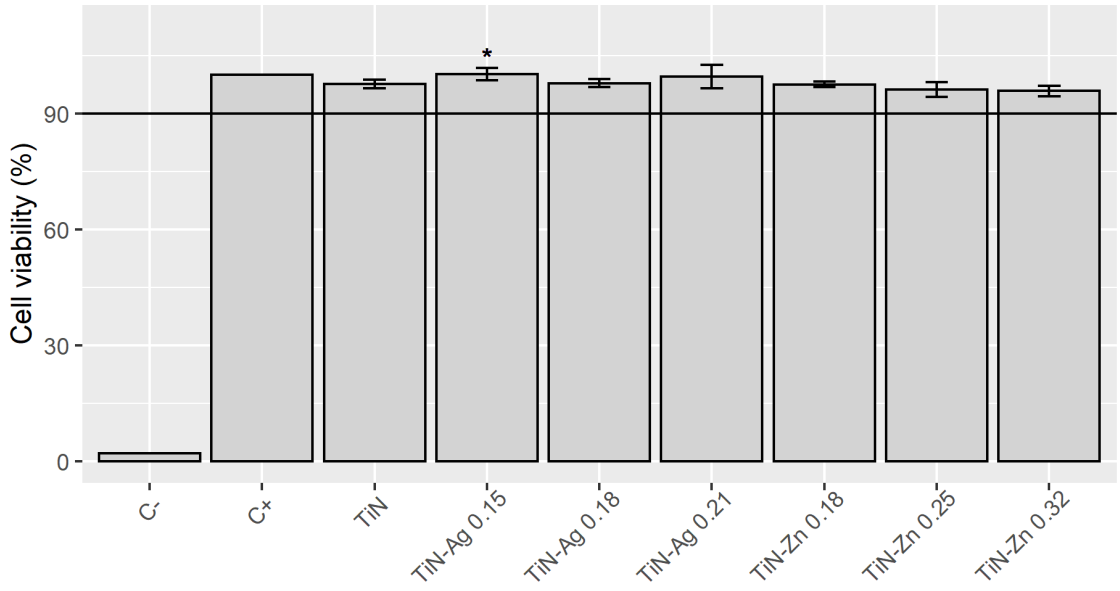


*Figure 30 - Cell viability assessed using the resazurin assay. C- was the negative control. C+ was the positive control. Data was represented as mean± standard deviation. Significant values as *p > 0.05.*

Thus, it is conclude that all samples present cell viability above 90%. These results allow supporting the theory that there is no leaching of cytotoxic substances from the coated substrates, making them cytotoxic-free in a systemic context.

### 3.2. Antibacterial activity:

When the surface roughness enters or approaches the micrometer level, bacterial adhesion increases in parallel with the roughness. This can be explained by the attachment point theory. The theory states that for organisms smaller than the microstructure of the surface, increasing roughness results in more attachment points and microscale shelters of refuge, which will protect adherent organisms from hydrodynamic shear forces [19]. Taking into account the bacteria used in the antibacterial tests, which are discussed ahead, this protection phenomenon conferred by roughness will not have interference in the results since: the *Escherichia coli* which is cylindrical gram-negative bacteria, presenting a length of 1-2 µm and 0. 5 µm radius [20]; *Streptococcus mutans* which is a spherical gram-positive bacterium with a diameter varying between 0.5-0.7 µm; and *Staphylococcus aureus* which is a gram-positive bacterium with a diameter varying between 0.5-1.5 µm [21].

The antibacterial activities were quantitatively evaluated by the number of viable cells (CFU). The data collected were normalized considering that the number of CFU/ml counted in the TiN samples on each day corresponds to 100% survival. In this way, it is possible to compare the survival rates obtained in the various experiments. Since the results of this assay are subject to several execution errors and the conversion of dilutions may result in differences in the order of $10^6$ CFU/ml, boxplots were used to remove outliers that could appear, figure 32.

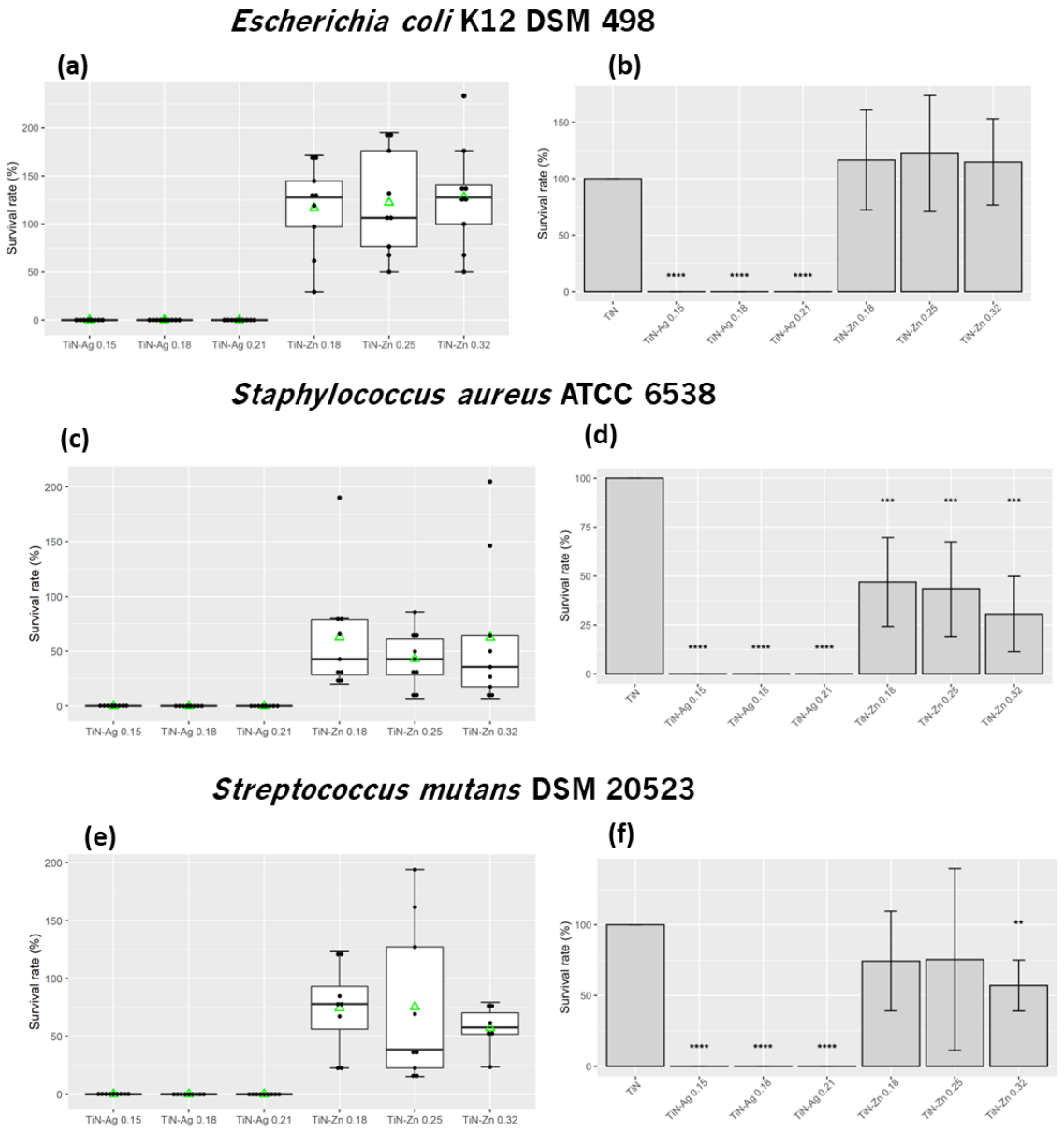


*Figure 31 - Survival rate (%) of: E. coli: (a) boxplot, (b) bar graph; S. aureus: (c) boxplot, (d) bar graph; S. mutans: (e) boxplot, (f) bar graph. Data was represented as mean± standard deviation. Significant values as ****p < 0.0001***p <0.001, **p < 0.01. The green triangle symbolises the mean, the black line the median and the dots the values obtained in each repetition.*

The above results indicate that the presence of silver in the coatings significantly improves the antibacterial activity, completely inhibiting the survival of the three bacteria tested. This reduction is statistically significant *(p-value* ≤ 0.0001) regardless of the silver content present in the coating, resulting in a 0% survival rate. As can be seen, TiN-Ag 0.21 has a higher silver content (13 at.%) than TiN-Ag 0.15 and TiN-Ag 0.18 (3 at. % and 8 at.%, respectively), and survival rates do not differ.

TiN-Ag 0.18 and TiN-Ag 0.21 coatings exhibit silver agglomerates on the surface. Although it cannot be conclude in this work, that the presence and agglomerates of silver on the surface improves the antibacterial behaviour, Velasco et al [22], reported that the direct interaction of silver with the bacterial cell is relevant in the antibacterial activity.

The antibacterial activity of silver-doped coatings lies in the fact that the released silver ions interact with membrane proteins of the respiratory chain, disrupting the reduction of $O_2$ and causing the production of ROS [23]. The thioredoxin (TrX) system, which is composed of nicotinamide adenine dinucleotide phosphate, thioredoxin reductase (TrxR) and TrX, is one of the main disulfide reductase systems used by bacteria against oxidative stress. In recent studies, it has been shown that Ag ions bind to the active site of Trx and TrxR of Staphylococcus aureus leading to oligomeration and functional disruption of these enzymes [24].

Conversely, zinc doped coatings, show no antibacterial effect on *E. coli* since all coatings show a survival rate of around 100%. In a previous study, it was reported that zinc does not show antibacterial activity against *E. coli*, being necessary to be present in a concentration of the order of 50 mg/L to have any effect [25]. On the other hand, when the coating is expose to gram-positive bacteria, such as *S. aureus* and *S. mutans*, the surfaces show antibacterial activity, this effect being more noticeable in the coating with higher zinc content. In the case of *S. aureus*, a statistically significant reduction (*p-value* $\leq 0.001$) is achieved for the various Zn contents. TiN-Zn 0.32 (25 at. %), which shows a 30% survival rate while TiN-Zn 0.18 (5 at.%) and TiN-Zn 0.25 (6 at.%) show a 46% and 43% survival rate, respectively. In the case of *S. mutans*, a statistically significant reduction (*p-value* $\leq 0.01$) was achieved only for TiN-Zn 0.32, with a 57% survival rate, while TiN-Zn 0.18 and TiN-Zn 0.25 had a 75% survival rate. The antibacterial effect of Zn nanoparticles is similar to that of silver, working through the destruction of cell membranes and the production of ROS, however in this case there is a dose-dependent antibacterial effect [26] [27].

## 4.1. Cell's Adhesion, cell's proliferation, and Cell's differentiation assay:

The initial interaction with the coating is extremely important as it determines the subsequent cell proliferation [28]. Thus, figure 33 shows the results of the adhesion test performed with SaOS-2 cells on the different coatings.

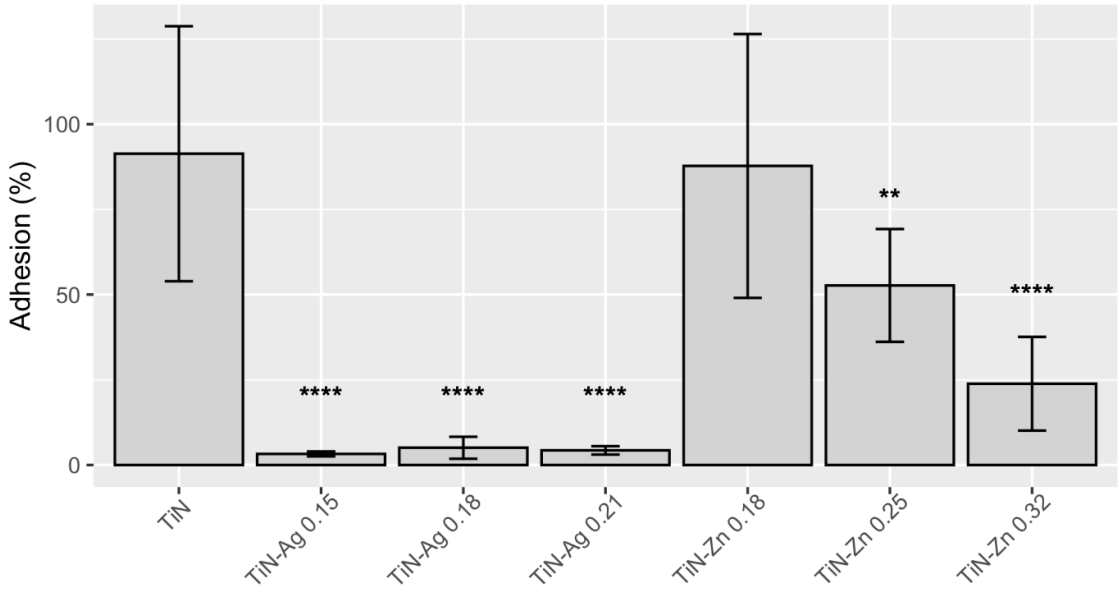


*Figure 32 - Adhesion of SaOS-2 cells on different coatings. Data was represented as mean± standard deviation. Significant values as ****p < 0.0001, **p < 0.01.*

Silver doped coatings show an adhesion in the order of 4%, (*p-value* ≤ 0.0001), regardless of the silver content of the samples. These results are in agreement with those described by Gokcekaya et al [29] where he concluded that the adhesion of osteoblasts on silver-doped surfaces decreases with increasing silver content present. In contrast, Jin et al [30] concluded that Zn can stimulate osteoblast adhesion, which agrees with the results obtained for zinc doped coatings show an adhesion rate of 87% for TiN-Zn 0.18, 52% for TiN-Zn 0.25 (*p-value* ≤ 0.01) and 23% for TiN-Zn 0.32 (*p-value* ≤ 0.0001). Thus, it can be conclude that cell adhesion in zinc doped coatings decreases as the zinc content present in the coating increases.

To evaluate SaOS-2 cell's proliferation, a TiN-coated Ti-6Al-4V substrate was compared with the coatings produced. As our aim would be to analyse the effect of doping the coatings with Ag and Zn, a Two-way ANOVA statistical test, using Dunnett's multiple comparisons test, was performed, comparing TiN with the other produced coatings, table 12.

*Table 12 – Proliferation two-way ANOVA statistical test results comparing TiN coating with doped coatings.*

| | p value summary | | | | |
|---|---|---|---|---|---|
| | **Day 1** | **Day 4** | **Day 7** | **Day 11** | **Day 14** |
| **TIN vs Control** | **** | **** | **** | **** | **** |
| **TiN vs TiN-Ag 0.15A** | **** | **** | **** | **** | **** |
| **TiN vs TiN-Ag 0.18A** | **** | **** | **** | **** | **** |
| **TiN vs TiN-Ag 0.21A** | **** | **** | **** | **** | **** |
| **TiN vs TiN-Zn 0.18A** | ns | ns | ns | ns | ns |
| **TiN vs TiN-Zn 0.25A** | ** | *** | *** | *** | ** |
| **TiN vs TiN-Zn 0.32A** | **** | **** | **** | **** | **** |

The SaOS-2 cell's proliferation results show that the proliferation of SaOS-2 cells in silver doped coatings is very low, being almost null. On the other hand, in zinc doped coatings, it seems that proliferation decreases with increasing zinc content in the coating. These results are linked with those obtained in adhesion, since zinc can significantly stimulate adhesion and proliferation of osteoblastic cells [31]. However, increasing hydrophobicity has also been shown to decrease cell adhesion and proliferation, figure 34 [32] [33]. Another important factor is that although the silver ions released from the coatings contribute to their antibacterial activity, it has also been reported that these ions interfere with cell division, causing structural changes in the cell membrane, generating ROS, inducing stress in microorganisms, causing DNA data and chromosomal mutations that end up being the main factor causing cell cycle arrest [34]. That said, more systematic studies are needed to understand the effects of silver ions released from the surface on cytotoxicity. Regarding Zn-doped coatings, Santos et al [35] concluded the presence of Zn in low concentrations, may induce in osteoblasts a higher proliferation [36] and a higher production of alkaline phosphatase, since zinc is also known as a growth inhibitor.

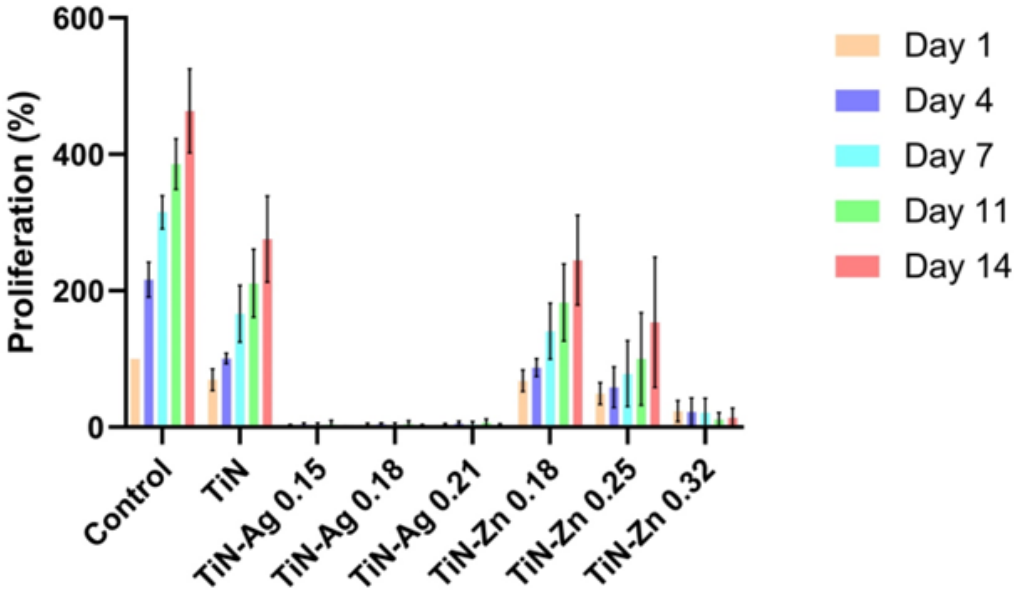


*Figure 33 - Cell proliferation of SaOS-2 cells "seeded" on the coatings produced. The control is SaOS-2 cells grown on the plates.*

SaOS-2 cell differentiation was assessed by histological staining for alkaline phosphatase. A two-way ANOVA analysis, using Dunnett's multiple comparisons test, was performed to statistically evaluate the results allowed some critical conclusions to be drawn. In this analysis, the results obtained in TiN coatings were compared with the doped coatings, in order to be possible to evaluate the effect of TiN doping, table 13.

*Table 13 - ALP activity two-way ANOVA statistical test results comparing TiN coating with doped coatings*

| | **p-value summary** | | | |
|---|---|---|---|---|
| | **Day 5** | **Day 8** | **Day 12** | **Day 15** |
| **TiN vs TiN-Ag 0.15A** | **** | **** | **** | **** |
| **TiN vs TiN-Ag 0.18A** | **** | **** | **** | **** |
| **TiN vs TiN-Ag 0.21A** | **** | **** | **** | **** |
| **TiN vs TiN-Zn 0.18A** | ns | ** | ns | ns |
| **TiN vs TiN-Zn 0.25A** | ns | ns | **** | ns |
| **TiN vs TiN-Zn 0.32A** | * | ns | **** | ** |

The results show that the silver doped coatings practically do not present ALP activity. On the other hand, TiN-Zn 0.18 coating show ALP activity similar to TiN coatings, which decreases with increasing zinc content in the coating, figure 35.

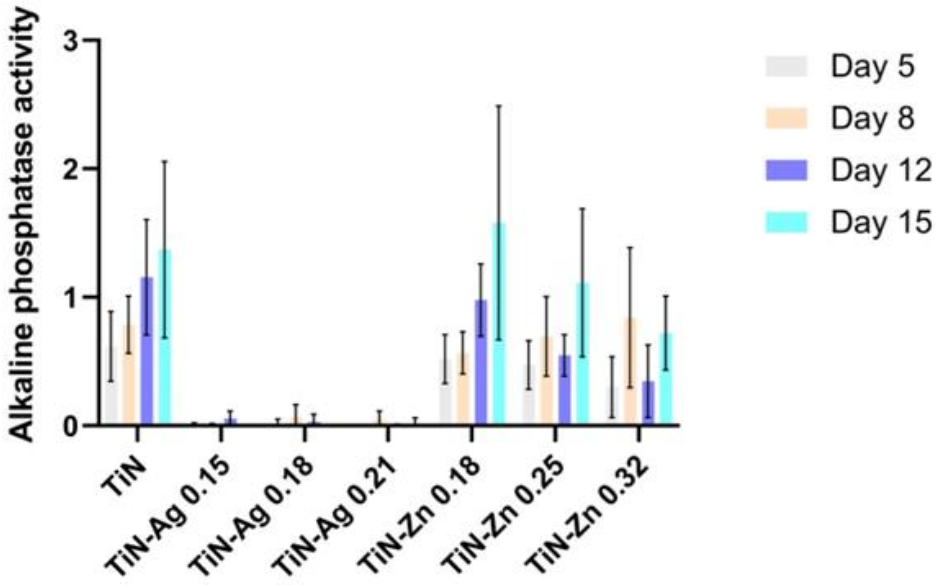


*Figure 34 - ALP activity of SaOS-2 cells "seeded" on the coatings produced.*

Thus, it is concluded that silver-doped coatings decrease the differentiation of osteoblasts, despite several papers reporting that silver nanoparticles can increase mineralisation and alkaline phosphatase expression [37]. These results are also influenced by the poor adhesion demonstrated by the samples. On the other hand, zinc doped coatings show more encouraging data since TiN-Zn 0.18A and TiN-Zn 0.25A samples show similar values to that obtained in TiN. These results are in line with existing works in the literature, where it is described that in general, materials containing Zn promote osteogenic differentiation [38] [39]. Another factor that also for the increase of ALP activity is the increase of roughness [40].

## 4. References:


[1] S. M. Marques, N. K. Manninen, S. Lanceros-Mendez, and S. Carvalho, “Ag-TiNx electrodes deposited on piezoelectric poly(vinylidene fluoride) for biomedical sensor applications,” Sens Actuators A Phys, vol. 234, 2015, doi: 10.1016/j.sna.2015.08.016.

[2] J. D. Castro et al., “Surface functionalization of 3D printed structures: Aesthetic and antibiofouling properties,” Surf Coat Technol, vol. 386, 2020, doi: 10.1016/j.surfcoat.2020.125464.

[3] “Sputtering Yield Rates.” https://www.semicore.com/reference/sputtering-yields-reference (accessed Oct. 06, 2022).

[4] P. Jisheng, W. Zhenxia, T. Zhenlan, and Z. Jiping, “Influence of surface topography on the sputtering yields of silver,” Nuclear Inst. and Methods in Physics Research, B, vol. 67, no. 1–4, 1992, doi: 10.1016/0168-583X(92)95863-M.

[5] M. Lievore de Brandão, T. Batista Degli Esposti, E. Décio Bisognin, N. David Harari, G. Maciel Vidigal Jr, and M. Baltazar Conz, “Superfície dos implantes osseointegrados X resposta biológica Dental implants surface X biological response: a literature review,” Caderno Científico REVISTA IMPLANTNEWS, vol. 7, no. 1, 2010.

[6] C. Lopes et al., “TiAg x thin films for lower limb prosthesis pressure sensors: Effect of composition and structural changes on the electrical and thermal response of the films,” Appl Surf Sci, vol. 285, no. PARTA, 2013, doi: 10.1016/j.apsusc.2013.07.021.

[7] D. Machado, P. Pedrosa, C. Fonseca, N. Martin, and F. Vaz, “Structural and morphological changes in Ag:TiN nanocomposite films promoted by in-vacuum annealing,” Journal of Nano Research, vol. 25, 2013, doi: 10.4028/www.scientific.net/JNanoR.25.67.

[8] J. A. Thornton, “Structure-Zone Models Of Thin Films,” in Modeling of Optical Thin Films, 1988, vol. 0821. doi: 10.1117/12.941846.

[9] D. K. Owens and R. C. Wendt, “Estimation of the surface free energy of polymers,” J Appl Polym Sci, vol. 13, no. 8, 1969, doi: 10.1002/app.1969.070130815.

[10] J. Avossa et al., “Forming nanostructured surfaces through Janus colloidal silica particles with nanowrinkles: A new strategy to superhydrophobicity,” Appl Surf Sci, vol. 465, 2019, doi: 10.1016/j.apsusc.2018.09.131.

[11] I. P. Okokpujie, C. A. Bolu, O. S. Ohunakin, and E. T. Akinlabi, “Experimental Study of the Effect of TiN–Zn Coated High-Speed Steel Cutting Tool on Surface Morphology of AL1060 Alloy During Machining Operation,” in Lecture Notes in Mechanical Engineering, 2021. doi: 10.1007/978-981-15-4745-4_57.

[12] F. Rupp, L. Liang, J. Geis-Gerstorfer, L. Scheideler, and F. Hüttig, “Surface characteristics of dental implants: A review,” Dental Materials, vol. 34, no. 1. 2018. doi: 10.1016/j.dental.2017.09.007.

[13] H. Terheyden, N. P. Lang, S. Bierbaum, and B. Stadlinger, “Osseointegration - communication of cells,” Clin Oral Implants Res, vol. 23, no. 10, 2012, doi: 10.1111/j.1600-0501.2011.02327.x.

[14] E. P. Ivanova et al., “Impact of nanoscale roughness of titanium thin film surfaces on bacterial Retention,” Langmuir, vol. 26, no. 3, 2010, doi: 10.1021/la902623c.

[15] S. Plaipichit et al., “Preparation of TiN nanorods for SERS substrate by controlling pulse frequency of high power impulse magnetron sputtering,” Optik (Stuttg), p. 170081, Oct. 2022, doi: 10.1016/J.IJLEO.2022.170081.

[16] C. Yang, R. Wang, B. Jiang, J. Hao, and D. Dong, “Effect of Target Power Ratio on Microstructure and Deposition Rate of Tin Film Deposited by Dual Pulse Power Magnetron Sputtering,” SSRN Electronic Journal, 2022, doi: 10.2139/ssrn.4067201.

[17] J. G. Yu et al., “Influence of Ag concentration on microstructure, mechanical properties and cytocompatibility of nanoscale Ti-Ag-N/Ag multilayers,” Surf Coat Technol, vol. 312, 2017, doi: 10.1016/j.surfcoat.2017.01.104.

[18] Y. Wang et al., “Preparation and in vitro antibacterial properties of anodic coatings co-doped with Cu, Zn, and P on a Ti–6Al–4V alloy,” Mater Chem Phys, vol. 241, 2020, doi: 10.1016/j.matchemphys.2019.122360.

[19] S. Wu, S. Altenried, A. Zogg, F. Zuber, K. Maniura-Weber, and Q. Ren, “Role of the Surface Nanoscale Roughness of Stainless Steel on Bacterial Adhesion and Microcolony Formation,” ACS Omega, vol. 3, no. 6, 2018, doi: 10.1021/acsomega.8b00769.

[20] M. Riley, “Correlates of smallest sizes for microorganisms,” in Size Limits of Very Small microorganisms: Proceedings of a Workshop, 1999.

[21] J. Y. Park and K. S. Seo, “Staphylococcus aureus,” in Food Microbiology: Fundamentals and Frontiers, 2019. doi: 10.1128/9781555819972.ch21.

[22] S. Calderon Velasco, A. Cavaleiro, and S. Carvalho, “Functional properties of ceramic-Ag nanocomposite coatings produced by magnetron sputtering,” Progress in Materials Science, vol. 84. 2016. doi: 10.1016/j.pmatsci.2016.09.005.

[23] Y. M. Long et al., “Surface ligand controls silver ion release of nanosilver and its antibacterial activity against Escherichia coli,” Int J Nanomedicine, vol. 12, 2017, doi: 10.2147/IJN.S132327.

[24] S. Gon, M. J. Faulkner, and J. Beckwith, “In vivo requirement for glutaredoxins and thioredoxins in the reduction of the ribonucleotide reductases of Escherichia coli,” Antioxid Redox Signal, vol. 8, no. 5–6, 2006, doi: 10.1089/ars.2006.8.735.

[25] R. C. T. Porto, P. Z. Uchôa, L. T. Peschel, B. Justi, L. A. D. Koslowski, and A. L. Nogueira, “Nanopartículas de óxido de zinco sintetizadas pelo método poliol: Caracterização e avaliação da atividade antibacteriana,” Revista Materia, vol. 22, 2017, doi: 10.1590/S1517-707620170005.0248.

[26] M. M. Almoudi, A. S. Hussein, M. I. Abu Hassan, and N. Mohamad Zain, “A systematic review on antibacterial activity of zinc against Streptococcus mutans,” Saudi Dental Journal, vol. 30, no. 4. 2018. doi: 10.1016/j.sdentj.2018.06.003.

[27] K. H. Tam et al., “Antibacterial activity of ZnO nanorods prepared by a hydrothermal method,” Thin Solid Films, vol. 516, no. 18, 2008, doi: 10.1016/j.tsf.2007.11.081.

[28] L. Fialho, L. Grenho, M. H. Fernandes, and S. Carvalho, “Porous tantalum oxide with osteoconductive elements and antibacterial core-shell nanoparticles: A new generation of materials for dental implants,” Materials Science and Engineering C, vol. 120, 2021, doi: 10.1016/j.msec.2020.111761.

[29] O. Gokcekaya et al., “Effect of precursor deficiency induced ca/p ratio on antibacterial and osteoblast adhesion properties of ag-incorporated hydroxyapatite: Reducing ag toxicity,” Materials, vol. 14, no. 12, 2021, doi: 10.3390/ma14123158.

[30] G. I. Bell, M. Dembo, and P. Bongrand, “Cell adhesion. Competition between nonspecific repulsion and specific bonding,” Biophys J, vol. 45, no. 6, 1984, doi: 10.1016/S0006-3495(84)84252-6.

[31] G. Jin, H. Cao, Y. Qiao, F. Meng, H. Zhu, and X. Liu, “Osteogenic activity and antibacterial effect of zinc ion implanted titanium,” Colloids Surf B Biointerfaces, vol. 117, 2014, doi: 10.1016/j.colsurfb.2014.02.025.

[32] L. Li, Q. Li, M. Zhao, L. Dong, J. Wu, and D. Li, “Effects of Zn and Ag Ratio on Cell Adhesion and Antibacterial Properties of Zn/Ag Coimplanted TiN,” ACS Biomater Sci Eng, vol. 5, no. 7, 2019, doi: 10.1021/acsbiomaterials.9b00248.

[33] H. D. Mejía, A. M. Echavarría, and G. Bejarano G., “Influence of Ag-Cu nanoparticles on the microstructural and bactericidal properties of TiAlN(Ag,Cu) coatings for medical applications deposited by Direct Current (DC) magnetron sputtering,” Thin Solid Films, vol. 687, 2019, doi: 10.1016/j.tsf.2019.137460.

[34] S. H. Choi, Y. S. Jang, J. H. Jang, T. S. Bae, S. J. Lee, and M. H. Lee, “Enhanced antibacterial activity of titanium by surface modification with polydopamine and silver for dental implant application,” J Appl Biomater Funct Mater, vol. 17, no. 3, 2019, doi: 10.1177/2280800019847067.

[35] M. H. Santos, A. P. M. Shaimberg, P. Valerio, A. M. Goes, M. de F. Leite, and H. S. Mansur, “Cytocompatibility evaluation of hydroxyapatite/collagen composites doped with Zn+2,” Matéria (Rio de Janeiro), vol. 12, no. 2, 2007, doi: 10.1590/s1517-70762007000200009.

[36] A. Grandjean-Laquerriere et al., “Influence of the zinc concentration of sol-gel derived zinc substituted hydroxyapatite on cytokine production by human monocytes in vitro,” Biomaterials, vol. 27, no. 17, 2006, doi: 10.1016/j.biomaterials.2006.01.024.

[37] H. Xie, P. Wang, and J. Wu, “Effect of exposure of osteoblast-like cells to low-dose silver nanoparticles: uptake, retention and osteogenic activity,” Artif Cells Nanomed Biotechnol, vol. 47, no. 1, 2019, doi: 10.1080/21691401.2018.1552594.

[38] S. Wang et al., “The impact of Zn-doped synthetic polymer materials on bone regeneration: a systematic review,” Stem Cell Research and Therapy, vol. 12, no. 1. 2021. doi: 10.1186/s13287-021-02195-y.

[39] F. Westhauser et al., “Impact of zinc-or copper-doped mesoporous bioactive glass nanoparticles on the osteogenic differentiation and matrix formation of mesenchymal stromal cells,” Materials, vol. 14, no. 8, 2021, doi: 10.3390/ma14081864.

[40] B. G. X. Zhang, D. E. Myers, G. G. Wallace, M. Brandt, and P. F. M. Choong, “Bioactive coatings for orthopaedic implants-recent trends in development of

implant coatings," International Journal of Molecular Sciences, vol. 15, no. 7. 2014. doi: 10.3390/ijms150711878.

[41] F. Yan et al., "Thermal stabilization of nanocrystalline promoting conductive corrosion resistance of TiN–Ag films for metal bipolar plates," Vacuum, vol. 195, 2022, doi: 10.1016/j.vacuum.2021.110631.

[42] Y. Y. Tse, D. Babonneau, A. Michel, and G. Abadias, "Nanometer-scale multilayer coatings combining a soft metallic phase and a hard nitride phase: Study of the interface structure and morphology," Surf Coat Technol, vol. 180–181, 2004, doi: 10.1016/j.surfcoat.2003.10.139.

# Chapter 6 – Final remarks and future research:

# 1. Final remarks:

The main objective of this work was the development of multifunctional coatings to be applied to dental implants, in order to improve the osseointegration, the mechanical and antibacterial properties of these devices, based on two systems, TiN-Ag and TiN-Zn.

To meet this objective, the following specific tasks had to be developed:

- Magnetron sputtering deposition on Ti-6Al-4V substrates of two different systems, TiN-Ag with different Ti/Ag atomic ratios and TiN-Zn coatings with different Ti/Zn atomic ratios, where the current density applied to the Ag and Zn targets was varied.
- To characterize physically and chemically the deposited coatings
- To analyse the biocompatibility
- To evaluate the antibacterial activity
- To study cell adhesion, proliferation, and differentiation.

The results show that the different processing conditions allowed to obtain different systems, where it was possible to change the physical and chemical properties of both TiN-Ag and TiN-Zn series. By varying the current density applied to the dopant element target (Ag and Zn), it was possible to obtain coatings with different rat and zinc contents. This content increases with the increase of the applied current density.

According to the morphology analysis, for TiN-Ag series, only TiN-Ag 0.15 coating is homogeneous. In TiN-Ag 0.18 and TiN-Ag 0.21, agglomerates appear on the surface, which increase with increasing silver content. On the other hand, the samples of TiN-Zn series present a heterogeneous structure. The AFM analysis suggested that both series of coatings increase their roughness with increasing dopant element content. This effect is extremely noticeable in the TiN-Zn series.

The water contact angles obtained for the different coatings indicate that TiN and TiN-Ag 0.15 are coatings with a hydrophilic character. On the other hand, the remaining coatings produced present a contact angle greater than 90° indicating that they are hydrophobic

The XRD analysis reveals that for TiN-Ag series, the crystalline phase FCC- TiN and a crystalline phase FCC-Ag are present; for TiN-Zn series there is also the crystalline phase FCC-TiN and hexagonal phase of Zn on TiN-Zn 0.32.

All the coatings produced are biocompatible, do not demonstrate cytotoxicity, since cell viability levels are above 90%. The antibacterial activity of the samples of both series was evaluated. TiN-Ag coatings totally inhibit bacterial activity, whereas TiN-Zn coatings show antibacterial activity, dose-dependent, only on gram-positive bacteria.

Cell's adhesion, proliferation and differentiation were also evaluated with SaOS-2 cells. The results indicate that in general, fewer cells attach to silver coatings compared to TiN. in the case of TiN-Zn series, there is a dose dependent effect, where the increase in Zn concentration decreases cell adhesion. The same behaviour was verified in the proliferation and differentiation tests.

Globally, considering the objective of the work, TiN-Ag 0.15 and TiN-Zn 0.32 are the coatings that present the best properties to be applied in dental implants. The TiN-Ag 0.15 because no dose dependent property was found in this series and therefore, TiN-Ag 0.15 is the most economical coating. The TiN-Zn 0.32, because it was proved that the coatings doped with zinc improve its antibacterial properties with the increase of the zinc content.

## 2. Future work:

Future work involves the deposition of TiN, TiN-Ag 0.15 and TiN-Zn 0.32 coatings on dental implants in order to create a prototype. For this it is necessary to optimise the deposition conditions, since making depositions on flat substrates is not the same as depositing on a screw. It would also be interesting to repeat some tests, namely: the ICP-OES, performing it for a longer period of time to be able to see what the maximum concentration of Zn ions is reached; and the biological ones, conditioning the coatings with saline solution, since the adhesion of proteins on the surface could improve the adhesion and proliferation of osteoblasts. Then it would also be interesting to perform antimicrobial tests, for example with fungi and viruses, since the oral microbiota is composed of a wide variety of microorganisms, and instead of being done separately, i.e. one microorganism at a time, it would be interesting to perform the tests in consortium. Finally, it would be interesting to make a new series of TiN-Ag coatings with a lower silver content, since in antibacterial tests all the contents obtained excellent antibacterial activity, and it is not possible to find a middle ground, so that similar results could be obtained with a lower silver content, making the implant more economically reliable.

# Annex 1:

The parameters of the depositions of TiN, TiN-Ag, and TiN-Zn films are detailed in the following tables 1-7.

Table 1 - PVD deposition parameters of TiN.

| **TiN** | | |
|---|---|---|
| **Time (h)** | | 2 |
| **Temperature (ºC)** | | 185-190 |
| **BIAS voltage (V)** | | -75 |
| | | |
| **Pressure (Pa)** | | |
| **Base** | **$N_2$** | **Ar** |
| 0,31 | 75 | 492 |
| | | |
| **Target** | | |
| | **Ti** | |
| **Current density (DC) ($mA/cm^2$)** | 10 | |
| **Current density (PULS) ($mA/cm^2$)** | - | |
| **Potential (V)** | 365 | |
| **Power Density ($W/cm^2$)** | 3,7 | |

Table 2 -PVD deposition parameters of TiN-Ag 0,15.

| **TiN-Ag 0,15** | | |
|---|---|---|
| **Time (h)** | | 1,5 |
| **Temperature (ºC)** | | 180-185 |
| **BIAS voltage (V)** | | -50 |
| | | |
| **Pressure (Pa)** | | |
| **Base** | **$N_2$** | **Ar** |
| 0,39 | 75 | 490 |
| | | |
| **Target** | | |
| | **Ti** | **Ag** |
| **Current density (DC) ($mA/cm^2$)** | 10 | - |
| **Current density (PULS) ($mA/cm^2$)** | - | 0,75 |
| **Potential (V)** | 357 | 135 |
| **Power Density ($W/cm^2$)** | 3,6 | 0,11 |

Table 3 - PVD deposition parameters of TiN-Ag 0,18.

| **TiN-Ag 0,18** |
|---|

| | | |
|---|---|---|
| **Time (h)** | | 1,5 |
| **Temperature (ºC)** | | 190-200 |
| **BIAS voltage (V)** | | -50 |
| | | |
| **Pressure (Pa)** | | |
| **Base** | **$N_2$** | **Ar** |
| 0,25 | 86 | 490 |
| | | |
| **Target** | | |
| | **Ti** | **Ag** |
| **Current density (DC) ($mA/cm^2$)** | 10 | - |
| **Current density (PULS) ($mA/cm^2$)** | - | 0,90 |
| **Potential (V)** | 356 | 149 |
| **Power Density ($W/cm^2$)** | 3,6 | 0,14 |

Table 4 - PVD deposition parameters of TiN-Ag 0,21.

| **TiN-Ag 0,21** | | |
|---|---|---|
| **Time (h)** | | 1,5 |
| **Temperature (ºC)** | | 195-200 |
| **BIAS voltage (V)** | | -50 |
| | | |
| **Pressure (Pa)** | | |
| **Base** | **$N_2$** | **Ar** |
| 0,25 | 86 | 493 |
| | | |
| **Target** | | |
| | **Ti** | **Ag** |
| **Current density (DC) ($mA/cm^2$)** | 10 | - |
| **Current density (PULS) ($mA/cm^2$)** | - | 1,05 |
| **Potential (V)** | 353 | 162 |
| **Power Density ($W/cm^2$)** | 3,5 | 0,17 |

Table 5 - PVD deposition parameters of TiN-Zn 0,18.

| **TiN-Zn 0,18** | | |
|---|---|---|
| **Time (h)** | | 1,5 |
| **Temperature (ºC)** | | 195-200 |
| **BIAS voltage (V)** | | -50 |
| | | |
| **Pressure (Pa)** | | |
| **Base** | **$N_2$** | **Ar** |
| 0,67 | 86 | 484 |
| | | |
| **Target** | | |
| | **Ti** | **Zn** |
| **Current density (DC) ($mA/cm^2$)** | 10 | - |
| **Current density (PULS) ($mA/cm^2$)** | - | 0.90 |
| **Potential (V)** | 336 | 177 |
| **Power Density ($W/cm^2$)** | 3,4 | 0,16 |

Table 6 - PVD deposition parameters of TiN-Zn 0,25.

| **TiN-Zn 0,25** | | |
|---|---|---|
| **Time (h)** | | 1,5 |
| **Temperature (ºC)** | | 195-200 |
| **BIAS voltage (V)** | | -50 |
| | | |
| **Pressure (Pa)** | | |
| **Base** | **$N_2$** | **Ar** |
| 0,52 | 87 | 482 |
| | | |
| **Target** | | |
| | **Ti** | **Zn** |
| **Current density (DC) ($mA/cm^2$)** | 10 | - |
| **Current density (PULS) ($mA/cm^2$)** | - | 1,25 |
| **Potential (V)** | 330 | 220 |
| **Power Density ($W/cm^2$)** | 3,3 | 0,28 |

Table 7 - PVD deposition parameters of TiN-Zn 0,32.

| **TiN-Zn 0,32** | | |
|---|---|---|
| **Time (h)** | | 1,5 |
| **Temperature (ºC)** | | 195-200 |
| **BIAS voltage (V)** | | -50 |
| | | |
| **Pressure (Pa)** | | |
| **Base** | **$N_2$** | **Ar** |
| 0,99 | 86 | 480 |
| | | |
| **Target** | | |
| | **Ti** | **Zn** |
| **Current density (DC) ($mA/cm^2$)** | 10 | - |
| **Current density (PULS) ($mA/cm^2$)** | - | 1,60 |
| **Potential (V)** | 332 | 251 |
| **Power Density ($W/cm^2$)** | 3,3 | 0,40 |